Title
Stochastic Characterization of Aftershock Building Seismic Performance

Author
Shokrabadi, Mehrdad

Publication Date
2018

Peer reviewed|Thesis/dissertation

UNIVERSITY OF CALIFORNIA

Los Angeles

Stochastic Characterization of Aftershock Building Seismic Performance

A dissertation submitted in partial satisfaction

of the requirements for the degree

Doctor of Philosophy in Civil Engineering

by

Mehrdad Shokrabadi

2018

ABSTRACT OF THE DISSERTATION

Stochastic Characterization of Aftershock Building Seismic Risk

by

Mehrdad Shokrabadi

Doctor of Philosophy in Civil Engineering

University of California, Los Angeles, 2018

Professor Henry V. Burton, Chair

The increase in seismic activity after a large-magnitude earthquake coupled with the reduction in the lateral load-carrying capacity of the affected structures presents a significant human and financial risk to communities. The focus of this study is placed on formulating a framework for quantifying the impact of both the elevated post-mainshock seismic hazard as well as the mainshock-induced structural damage on building seismic performance. The viability of the proposed framework is examined through its application to mainshock-aftershock seismic performance evaluation of a set of reinforced concrete frames. Additionally, discrepancies between the frequency content of mainshock and aftershock ground motions and their impact on the seismic performance of RC moment frames is investigated. Two metrics are used in evaluating the seismic performance; seismic risk and seismic-induced financial losses. Both metrics are evaluated in both pre- and post-mainshock environments. The time-dependent nature of seismic hazard in the post-mainshock environment is accounted for through the adoption of a Markov risk assessment framework. In the post-mainshock environment, the seismic risk is examined as a function of the time elapsed since the mainshock's occurrence while in the pre-mainshock environment, the risk is investigated during an assumed lifespan of 50 years for the studied structures. For the buildings and the high-seismicity site used in this study, both the increased post-mainshock seismic hazard as well as the reduction in the structural capacity are found to have a great influence on the seismic risk. The application of the proposed frameworks for seismic performance under mainshock-aftershock ground motions to the reinforced concrete frame buildings in Los Angeles County is also demonstrated. The outcomes of the regional seismic performance analysis show that omitting aftershocks from the seismic performance steps would lead to underestimating annual expected seismic risk and loss by up to 50% and 15%.

The dissertation of Mehrdad Shokrabadi is approved.

Jonathan Paul Stewart

John Wright Wallace

Jian Zhang

Abbie B. Liel

Henry V. Burton, Committee Chair

University of California, Los Angeles, 2018

2018

To my parents …

For their endless love, support and encouragement

Table of Contents

List of Tables

List of Figures

ACKNOWLEDGEMENTS

The research presented in this paper is supported by the National Science Foundation CMMI Research Grant No. 1554714 and the United States Geological Survey (USGS) EHP Award Number G16AP00006. Any opinions, findings, and conclusions or recommendations expressed in this paper are those of the authors and do not necessarily reflect the views of the sponsor.

The authors would like to thank Professor Meera Raghunandan of Indian Institute of Technology Bombay and Professor Abbie B. Liel of University of Colorado Boulder for generously sharing their concrete moment frame numerical models. Their contribution is greatly appreciated.

VITA

2006-2010	B.Sc. in Civil Engineering, Amirkabir University of Technology, Tehran, Iran
2010-2012	M.Sc. in Structural Engineering, Amirkabir University of Technology, Tehran, Iran
2013-2014	M.Sc. in Earthquake Engineering, University of California Los Angeles
2017-2018	M.Sc. in Statistics, University of California Los Angeles
2014-2018	PhD Candidate in Structural and Earthquake Engineering, University of California Los Angeles

CHAPTER 1: Introduction

1.1 Motivation and Background

In recent years the seismic performance of buildings under sequential ground motions has drawn the attention of the structural engineering community. Recent advancements in probabilistic seismic performance assessment of structures have provided the structural and earthquake engineers with the tools necessary to examine the seismic performance of buildings under consecutive seismic events with a great degree of accuracy. The human and financial impacts of powerful aftershocks on communities in the aftermath of major seismic events have further highlighted the significance of the hazard imposed by aftershocks. Aftershocks can exacerbate earthquake-induced financial losses by causing further damage to structural and nonstructural components in buildings that have already been affected by a mainshock event. One of the most recent examples of the earthquake sequences is the two **M** 6.2 and **M** 6.0 aftershocks that followed the 2010 **M** 7.1 Darfield earthquake. In addition to the 185 deaths, the combined direct and indirect losses from over 150 thousand impacted buildings added up to over 30 billion dollars [1]. The 1999 Chi-Chi earthquake and the following powerful aftershocks with four greater than 6.5 magnitude [2], the additional casualties from the 2008 Wenchuan earthquake and the 89 aftershocks of the 2011 Tohoku earthquake with magnitudes larger than 6 [3] are just a handful of other real-life examples of the importance of the human and financial implications of powerful aftershocks.

Modern seismic design requirements are designed with the intention of ensuring public safety during a major mainshock earthquake. However, the direct and indirect seismic hazard due to the ensuing aftershocks can still pose a significant threat on communities. Whereas seismic loss assessment under isolated events has been addressed thoroughly in previous studies, comparatively less has been accomplished in the area of loss assessment under sequences of mainshock-aftershock ground motions. As such, a comprehensive framework that is capable of addressing the problem of seismic risk and loss assessment under sequential seismic events in a rigorous fashion is vital for mitigating the adverse of major seismic events on communities.

1.2 Objectives

The first objective of the current study is to examine mainshock and aftershock ground motions recorded from past events and determine if there are any meaningful systematic

discrepancies in their frequency contents. The impact of any differences in the frequency content on the seismic risk in a set of reinforced concrete frames is examined. The second main objective of this study is to develop a probabilistic framework that can be used as a tool for evaluating the seismic performance of any type of civil structures under sequential ground motions. The proposed framework is capable of estimating the seismic risk that building is subjected to during its lifetime due to the likely mainshock events and the aftershocks that would follow each mainshock for a certain period. Moreover, the financial losses due to the direct damage to the structural and non-structural contents of a building as well as the losses due to the disruption in its normal functionality can be quantified using the proposed loss evaluation framework. More specifically, the main objectives of the current study outlined below.

1. *If mainshocks and aftershocks ground motions are selected to have comparable source and distance properties, then can the mainshock ground motions substitute the aftershock records?* This issue is important due to the relatively small number of aftershock records available from past events. Aftershock ground motions are necessary in forming record-pairs that are used for performing response history analysis and simulating seismic response under sequential ground motions. If aftershock ground motions can indeed be replaced with mainshock records, then it is not necessary to be limited to the relatively small database of aftershock ground motions for forming the record-pairs. This issue is investigated by first selecting two sets of record-pairs where in one set both the first and second ground motions in each pair are mainshocks whereas in the second set the record-pairs are from actual mainshock-aftershock events. Both record-pair set are applied to a group of reinforced concrete frames and the impact of different record-pair selection approaches on seismic risk is examined.
2. *Is the correlation of ground motions between parent mainshocks and children aftershocks significant with respect to seismic response demands in structures?* This issue is investigated by developing story drift ratio prediction equations under mainshock-mainshock and mainshock-aftershock record-pairs and investigate the correlation between the residuals obtained in the development process of the prediction equations.
3. Develop a framework for the evaluation of seismic risk under sequential ground motions. This framework needs to be able to account for the uncertainty in the state of structures as they are to aftershock ground motions within a short period after the

causative mainshock without being restored to their pre-mainshock state. Moreover, the time-dependent nature of seismic hazard in the post-mainshock environment needs to be incorporated in the framework.

4. Propose a framework for seismic loss assessment under mainshock-aftershock ground motions. This framework builds on the seismic risk assessment approach of the previous step by expanding it to be able to estimate seismic-induced losses as well.
5. Demonstrate the viability of the proposed risk and loss assessment frameworks by showing their application to a set of case study reinforced concrete buildings.
6. Show the importance of incorporating aftershocks into the seismic risk and loss evaluation steps by conducting a regional seismic performance assessment for the reinforced concrete frames in Los Angeles County. The estimates of seismic risk and loss in the Los Angeles County obtained using the frameworks proposed in this study are compared and contrasted with the estimates obtained using a framework which only accounts for mainshocks.

1.3 Organization and Outline

The main body of the current study consists of five chapters. Most chapters are adopted from a research paper which is cited at the beginning of the chapter.

Chapter 2 is mostly focused on comparing the frequency contents of mainshock and aftershock ground motions and providing guidelines for record-pairs used in simulating seismic response under sequential ground motions. Earthquake engineers lack well-founded consensus guidelines for selecting ground motion time series for sequential mainshock-aftershock events for use in seismic performance assessment. Past practice has seen sequences formed by coupling as-recorded mainshock and aftershock records and by using repeated mainshock records for both event types. Using mainshock-mainshock versus mainshock-aftershock record pairs, we assess the structural performance of five ductile reinforced concrete frames with varying heights using sequential nonlinear response history analyses. The correlation between event terms of mainshock and aftershock ground motions recorded from the same sequence and its impact on maximum story drift ratio is also investigated. We provide recommendations for aftershock record selection that draw upon these results.

Chapter 3 outlines a framework for seismic risk evaluation under mainshock-aftershock ground motions. The increase in seismic activity after a large-magnitude earthquake coupled with the reduction in the lateral load-carrying capacity of the affected structures presents a

significant human and financial risk to communities. The focus of this chapter is placed on quantifying the impact of both the elevated post-mainshock seismic hazard as well as the mainshock-induced structural damage on the seismic risk of three reinforced concrete moment frame structures. The seismic hazard due to sequential earthquakes is examined in both pre- and post-mainshock environments. The time-dependent nature of seismic hazard in the post-mainshock environment is accounted for through the adoption of a Markov risk assessment framework. In the post-mainshock environment, the seismic risk is examined as a function of the time elapsed since the mainshock's occurrence while in the pre-mainshock environment, the risk is investigated during an assumed lifespan of 50 years for the studied structures.

Chapter 4 expands the framework discussed in Chapter 3 to seismic loss evaluation under sequential seismic events. Aftershocks have been shown to exacerbate earthquake-induced financial losses by causing further damage to structural and nonstructural components in buildings that have already been affected by a mainshock event and increasing the duration of disrupted functionality. Whereas seismic loss assessment under isolated events has been addressed thoroughly in previous studies, comparatively less has been accomplished in the area of loss assessment under sequences of mainshock-aftershock ground motions. The main objective of the current chapter is to formulate a comprehensive framework for quantifying financial losses under sequential seismic events. The proposed framework is capable of accounting for the uncertainties in the state of structure due to accumulation of earthquake-induced damage, the time-dependent nature of seismic hazard in the post-mainshock environment and the uncertainties in the occurrence of mainshock and aftershock events. Application of the proposed framework to a 4-story reinforced concrete moment frame is also demonstrated in this chapter.

Chapter 5 discusses the application of the frameworks discussed in Chapter 3 and Chapter 4 to a regional seismic performance assessment done for the reinforced concrete frames located in Los Angeles County. A framework for building-portfolio risk and loss assessment under mainshock-aftershock earthquake sequences is presented. Again, both the temporary increase in seismic hazard after a large-magnitude mainshock coupled with the reduction in the structural capacity under sequential ground motions are considered in the framework.

Chapter 6 summarizes the findings of the previous chapters and discusses the limitations of the current study and opportunities to improve the methodologies and frameworks presented in the previous chapters.

CHAPTER 2: Impact of Sequential Ground Motion Pairing on Mainshock-Aftershock Structural Response and Collapse Performance Assessment

---

This chapter is adopted from the following study:

Shokrabadi, M., Burton, H. V., and Stewart, J. (2018). "Impact of sequential ground motion pairing on mainshock-aftershock structural response and collapse performance assessment," *ASCE Journal of Structural Engineering (accepted for publication)*

2.1 Introduction

The notion of seismic resilience has gained significant attention in earthquake engineering research, education and practice in recent years. Central to achieving seismic resilience is understanding the role that buildings play in ensuring that communities can minimize the effects of, adapt to, and recover from earthquakes [4]. Quantifying the risk of further damage to the built environment from aftershocks is essential to post-mainshock decision-making, functionality and recovery. The compounding effect of the damage and disruption caused by the earthquake sequences in Chi-Chi (1999), Wenchuan (2008), Christchurch (2010-2011), Tohoku (2011) and Central Italy (2016) are just a few examples of the human and financial implications of mainshock-aftershock event sequences [3, 5, 6].

Advances in nonlinear structural response simulation [7], classifying mainshock-aftershock event sequences (e.g., Wooddell and Abrahamson [8]) and seismic hazard analysis for sequential events (e.g., Iervolino et al. [9], Boyd [10], Yeo and Cornell [11]) provide the essential ingredients to characterize structural performance to earthquake sequences. However, prior work on this topic has employed inconsistent protocols for selecting ground motions for event sequences and has not provided the needed insights required to arrive at consensus procedures. We seek to fill this gap in the present chapter. To help frame the discussion, it is useful at this stage to identify four approaches, most of which have been considered in various forms in the literature:

1. MS-MS (mainshock-mainshock): Select ground motions for both events in the sequence from earthquakes classified as mainshocks [12-20]. The second ground motion in an MS-MS sequence can be a scaled or an unscaled version of the first or a different motion selected from a database of mainshock recordings. As used here, the

second recording in an MS-MS sequence is not selected to represent the different source and path attributes of aftershocks.

2. TG-MS-MS (targeted mainshock-mainshock): The second ground motion in the pair, while recorded from a mainshock event, is selected to (as best as possible) match the characteristics of an aftershock motion, i.e. lower magnitude and larger rupture distance, than the first ground motion [12, 21].
3. SS-MS-AS (same-sequence mainshock-aftershock): First and second event records are taken from recordings of mainshock and aftershocks from the same sequence (e.g., Northridge earthquake mainshock and Northridge aftershocks). Most of the previous studies that utilized mainshock-aftershock ground motions were done with SS-MS-AS record-pairs [21-25].
4. DS-MS-AS (different-sequence mainshock-aftershock): Same as SS-MS-AS, but the first and second event records are now taken from two different sequences.

Several considerations affect the characteristics of aftershock ground motions, conditional upon the occurrence of a mainshock. First are implications for source and path − aftershocks are generally smaller in magnitude [26] and, for the same site, will typically have larger source-to-site distances (as a result of having smaller rupture area) than their parent mainshocks. Second, even when source and path differences are accounted for, evidence has been found of mild correlation between attributes of mainshock and aftershock records belonging to the same sequence [27]. SS-MS-AS record pairs can be considered "ideal" for sequential response history analysis because they would naturally capture these relationships between mainshock and aftershock ground motions. However, allowing for other constraints affecting ground motion selection for nonlinear response history analyses (e.g. matching target $\mathbf{M}$, R, V_{s30}, directivity conditions, and ε from hazard deaggregation), it may not be possible to adequately populate an SS-MS-AS record set. Using DS-MS-AS record-pairs would allow access to a broader pool of ground motions, which has obvious benefits, but at the cost of likely not preserving within-sequence ground motion correlations (as noted by Boore et al. [27]).

A few studies have investigated differences in the dynamic response of structures subjected to MS-MS and MS-AS sequences. Goda [21] compared the ductility demands imposed by MS-MS and SS-MS-AS sequences. The MS-MS sequences were selected such that the distribution of the magnitudes of the events producing the second motion in the pair would match the aftershock magnitude distribution predicted by Omori's law [28]. As such, the MS-MS sequence used by Goda [21] could be considered as TG-MS-MS, although the

effects of different rupture distances were not considered. A third foreshock-MS-MS sequence was also considered (originally proposed by Hatzigeorgiou and Beskos [12]) in which foreshock and aftershock records are scaled versions of mainshock records (factor of 0.85). The probability distribution of the peak ductility demands developed for a set of single-degree-of-freedom (SDOF) structures with different periods showed slight differences between responses obtained from the SS-MS-AS record-pairs and the MS-MS sequences generated based on Omori's law. The triad sequence produced significantly higher peak ductility demands. In a separate study, Goda [29] compared the collapse performance of a 2-story wood-frame building under both MS-MS and SS-MS-AS ground motion pairs. Unlike in Goda [21], in this case the MS-MS sequence used the same records in the second event as in the first. Not surprisingly, the MS-MS sequence produced higher collapse probabilities than SS-MS-AS. Ruiz-García [22] conducted a similar study using two low- and mid-height steel frames and reached the same conclusion.

From these prior studies, MS-MS sequences appear to be more damaging to structures than MS-AS sequences in which ground motions for the second event more accurately capture attributes of aftershock ground motions. However, there are several gaps in the state of knowledge pertaining to mainshock-aftershock record selection that we seek to address here, specifically:

1. *Is the correlation of ground motions from parent mainshocks to children aftershocks significant with respect to seismic response demands in structures?* We investigate this using carefully selected SS-MS-AS and DS-MS-AS record sequences.
2. *With suitable consideration of source and path differences between mainshocks and aftershocks, can records be selected from mainshock databases to represent the effects of aftershocks?* We investigate this by comparing responses obtained using TG-MS-MS sequences with those from SS-MS-AS.

Two other attributes of our study are distinct from prior work and are significant with respect to the aim of answering the above questions. First, whereas prior work has considered SDOF or multi-degree-of-freedom (MDOF) structures within a small period range, we use five realistic structural models of reinforced concrete frame structures ranging in height from 2- to 20-stories. The multi-mode responses inherent to such models, over a wide period range, is important to assess the impact of alternate record selection protocols.

A second important attribute, elaborated upon subsequently, is that we select ground motions for the alternate suites such that the characteristics that are likely to impact the

results of response history analyses (e.g., ε and V_{s30}) are similar. This control on record selection has not been exercised in prior studies [15-17]. This is an important feature of the selected record-pair sets that would ensure that the differences observed in the structural response under the four record-pair sets stem from the approach used to form the sequences and not the ground motion characteristics that can be controlled for when selecting the record-pairs.

Drawing upon the lessons from prior work, and the insights gained by resolving the above questions, we provide recommendations for selecting record-pairs for use in sequential response history analysis. We seek to accurately represent attributes of realistic ground motion sequences with due consideration of the constraints of record availability from the two event types. Lastly, we demonstrate the collapse safety of the five studied RC buildings using risk-based metrics, which also consider the effect of time-dependent aftershock hazard.

2.2 Ground Motion Selection for Building Aftershock Seismic Performance Assessment

2.2.1 Previous Studies on Differences in Frequency Contents of Mainshock and Aftershock Ground Motions

An important question that arises when selecting record-pairs for aftershock seismic performance assessment is whether it is appropriate to use mainshock-mainshock (MS-MS or TG-MS-MS) sequences for response history analyses. Previous studies have demonstrated that the response demand on a structure is significantly affected by the frequency content of the ground motion that is used in the analysis [30-32]. As such, any systematic differences in the frequency content of mainshock and aftershock records that are present after controlling for other characteristics (e.g. $\mathbf{M}$, R, V_{s30} and ε) would bias the results of aftershock performance assessments conducted using MS-MS or TG-MS-MS ground motions. On the other hand, if no significant differences are found, there is no need to be confined to the relatively limited library of the aftershock ground motions in selecting record-pairs. This section highlights previous studies related to this question.

Although based on a limited dataset, Boore and Atkinson [33] reported a difference in the magnitude scaling of spectral values of the mainshock and aftershock records from the 1985-1988 Nahanni and Miramichi earthquakes. In a different approach, Ruiz-García and Negrete-Manriquez [23] examined the predominant period (T_g) and bandwidth (Ω) of mainshock and aftershock ground motions recorded from seismic events in California. T_g is the period at

which the maximum pseudo spectral velocity of a 5%-damped SDOF occurs and Ω is a measure of how the spectral amplitudes of a ground motion are scattered around its central period. Ruiz-Garcia and Negrete-Manriquez reported a wider Ω for aftershock records and a weak correlation between the T_g of the mainshocks and aftershocks.

The difference in the frequency content of mainshock and aftershock ground motions has also been the subject of debate, specifically as it relates to the development of recent ground motion models (GMMs). Using a systematic approach to compare ground motions that allows for controlling the source and site characteristics (e.g. **M**, R), Boore et al. [27] examined the correlation of event terms from parent mainshocks and their children aftershock using the PEER NGA-West 2 database [34]. A mild correlation between the event terms was observed. No adjustment for aftershocks was included in the final functional form of their GMM as the difference between the event terms of mainshocks and average of event terms from aftershocks was practically zero and independent of magnitude.

For the original NGA project [35] functional forms used in some of the GMMs included a term to distinguish mainshocks from aftershocks. Abrahamson et al. [36] found that the median of spectral values of aftershocks at short periods are smaller than those from similar mainshocks, whereas at longer periods (> 0.75 sec) the aftershock spectral ordinates were larger. As shown in Fig. 2-1, Chiou and Youngs [37] reached a similar conclusion, but the transition from lower to higher spectral ordinates (of aftershocks relative to mainshocks) was about 2.0 sec. Such a relationship between S_a values of mainshocks and aftershocks needs to be viewed in the context of the different **M** and R expected for these two event types. Whereas aftershock demands will generally be smaller (due to lower **M** and larger R), their spectral shape is different from that of mainshocks as shown in Fig. 2-1. Chiou and Youngs also found that for aftershocks, the style of faulting had a smaller influence on the predicted spectral values, when compared to mainshocks. On the other hand, the depth to top of rupture (Z_{TOR}) had a stronger influence on the predictions made for aftershocks.

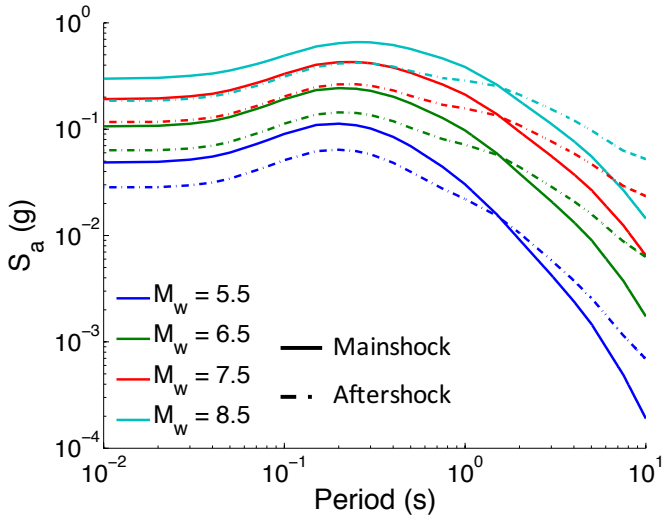

Fig. 2-1. Comparing the spectra of mainshock and aftershock records with similar magnitudes obtained from the GMM by Chiou and Youngs [37]

2.2.2 Ground Motions used for Mainshock-Aftershock Seismic Performance Assessment

Four sets of sequential ground motions are used for the seismic performance assessment. Each set contains 25 record-pairs selected from the PEER NGA-West2, K-NET and KiK-net databases. The first ground motion in each record-pair is from an event classified as a 'mainshock' in both databases whereas the second ground motion could be recorded from either a 'mainshock' or 'aftershock' event. Table 2-1 describes the selection of records for the two events in the sequence with respect to the attributes of the second event and attributes of the selected ground motion. The mainshock-aftershock classification for the ground motions selected from the PEER NGA-West2 database is based on the time and distance windowing algorithms developed by Wooddell and Abrahamson [8] while the classification for the K-NET and KiK-net databases is adopted from Goda [21], with a distance window based on Kagan [38] and a time window of 90 days.

For the MS-MS set, the second ground motion in the sequence is the same as the first. This set is included because it represents a common approach in the literature.

The second ground motion in DS-MS-AS sequences are from aftershock events that are not necessarily from the same event sequence as the mainshock. The effect of 'parent' and 'children' correlation on aftershock collapse risk is evaluated subsequently by comparing results from the DS-MS-AS and SS-MS-AS record-pair sets.

Each entry in the set of 25 TG-MS-MS record-pairs consists of two mainshock ground motions. The second ground motion is from mainshock events that are on average 1.0

magnitude unit smaller and at the same time, larger in distance than those of the first. Comparing the results from the SS-MS-AS and TG-MS-MS record-pair sets informs whether using mainshock ground motions as both records biases computed collapse capacities. If these two sets yield comparable results, the more comprehensive databases of mainshock ground motions can be used to assemble record-pairs, provided that an appropriate mainshock-aftershock magnitude and distance relationship is applied.

The SS-MS-AS set takes aftershock ground motions from the same event sequence as the mainshock. As such, this is the option in Table 2-1 that most reliably conforms to reality, and is the benchmark against which the two other schemes can be compared.

Table 2-1. Event and record sequence definitions adopted for simulations conducted in Chapter 2

Sequence notation	2nd (aftershock) event attribute	2nd event record attributes[1]
MS-MS: Mainshock-mainshock	Matches MS	Matches MS record
DS-MS-AS: MS and AS records from different event sequences	Distinct: -1.0[2] **M** unit (average), larger in R	Selected from AS record database, any event sequence
TG-MS-MS: Targeted MS-MS sequence	Distinct: -1.0[2] **M** unit (average), larger in R	Selected from MS record database
SS-MS-AS: MS and AS records from same event sequence	Distinct: **M** and R per natural sequence attributes	Selected from AS records following MS event in sequence

[1] In all cases, records from first event taken from mainshock records database

[2] This is the average differential between mainshock and aftershocks in the NGA-West2 database

All record-pairs were selected such that the probabilistic distributions of R, V_{s30} and ε values of the second-event ground motions are similar across the four sets. As discussed before, this ensures that observed differences in seismic response are not due to differences in these ground motion characteristics. The empirical cumulative distribution functions (CDF) of R, V_{s30} and ε for the second-event ground motion in the four record-pair-sets are compared using the two-sample Kolmogorov-Smirnov (KS) test [39]. A statistical hypothesis test is performed where the null hypothesis is that the R, V_{s30} and ε values in any two sets follow

the same empirical CDF. The output of the tests is expressed in the form of a $p-value$, which corresponds to the probability that the R, V_{s30} and ε values for two suites of ground motions are from identical probabilistic distributions. A $p-value$ of 5% is used as the acceptable margin [32]. If the $p-value$ obtained from the hypothesis test falls below 5%, then the difference between the R, V_{s30} and ε values of the records is deemed significant. A summary of the results from the KS-tests is shown in Table 2-2. As illustrated, almost all $p-values$ among the four sets of record-pairs are greater than 5%, confirming similarity in the distributions of R, V_{s30} and ε. It is worth noting that as the current databases of as-recorded ground motion sequences expand, further constraints on the other properties of ground motions that have been shown to be influence building ground motion properties (e.g., fault mechanism, duration), can also be imposed in the record selection process

Table 2-2. Summary of $\boldsymbol{p-values}$ from KS-Test on $\boldsymbol{R}$, $\boldsymbol{V_{s30}}$ and $\boldsymbol{\varepsilon}$

Record-pair set	$p-values$ from KS-test											
	SS-MS-AS			DS-MS-AS			TG-MS-MS			MS-MS		
	V_{s30}	R	ε	V_{s30}	R	ε	V_{s30}	R	ε	V_{s30}	R	ε
SS-MS-AS	1	1	1	0	0	0	0	0	0	0	0	0
	.00	.00	.00	.88	.99	.41	.41	.24	.41	.88	.06	.12
DS-MS-AS				1	1	1	0	0	0	0	0	0
				.00	.00	.00	.03	.12	.65	.12	.06	.24
TG-MS-MS							1	1	1	1	0	0
							.00	.00	.00	.00	.24	.88
MS-MS										1	1	1
										.00	.00	.00

Fig. 2-2a compares the magnitude versus distance distributions for the second-event ground motion in the four record-pair sets used for response history analysis. The upper and lower bounds on **M** are 5.6 and 7.6 respectively. The median spectra of the second-event ground motion in the record-pair-sets are compared in Fig. 2-2b. The spectral values of the second-event ground motion in the TG-MS-MS set are generally higher than the aftershock ground motion in the SS-MS-AS sets up to a period of about 2.0s, beyond which the spectral values of aftershock records approach or exceed those of the mainshocks. This observation is consistent with the trend predicted by the Chiou and Young GMM [37]. This is an interesting

observation given that **M** for the TG-MS-MS records are generally higher than those of the SS-MS-AS set.

As noted previously, one of the objectives of this work is to investigate the impact of mainshock-aftershock ground motion correlations on structural response engineering demand parameters (EDP). This is facilitated by the SS-MS-AS sequence, which implicitly contains these correlations, whereas others do not. To investigate the impact of SS-MS-AS correlation on EDPs, we develop subsequently a prediction equation for maximum SDR. By examining event-specific residuals relative to this prediction equation, we examine the impact of the correlation between parent and children events on SDR values for the five RC buildings.

To support development of the EDP prediction equation, we utilize SDR values obtained using a separate set of ground motions from those used in the sequence analyses (Table 2-1). For this application, we selected 620 ground motions from the NGA-West2 database, recorded from 17 parent mainshock events and their associated 27 children aftershocks as well as a set of 474 mainshock-mainshock ground motions. All of the records have **M** > 4.5 and R_{jb} < 100 km. The methodology used to interpret EDPs derived from these time series is presented subsequently.

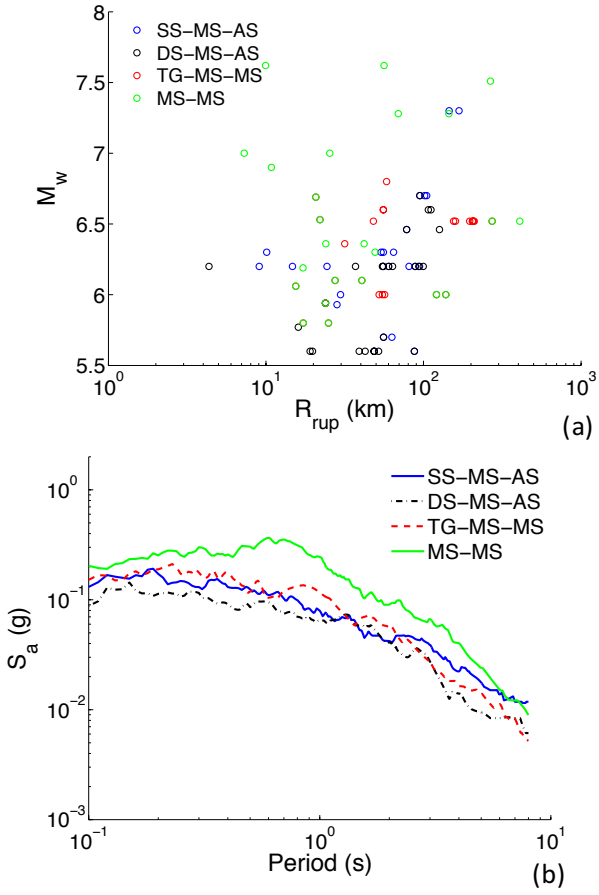

Fig. 2-2. Comparing a) the magnitude versus distance distributions and b) the median response spectra of the second-event ground motions in the four record-pair sets

2.2.3 Nonlinear Response Spectra for Ground Motions used for Mainshock-Aftershock Seismic Performance Assessment

A linear response spectrum provides insight into the frequency content of a ground motion. However, it is well known that the displacement demand in a nonlinear SDOF could be significantly larger than that of a linear SDOF when subjected to the same ground motions [40-43]. Past studies on the dynamic response of SDOFs have shown that the ratio of maximum displacements in nonlinear and linear SDOFs (C_u) can significantly exceed unity at short periods and for highly ductile systems [41-44]. Moreover, the response of nonlinear SDOFs is more representative of the behavior of nonlinear MDOF structures. In light of this, constant-ductility inelastic response spectra [45] of elastic-perfectly plastic (EPP) SDOFs, shown in Fig. 2-3, are used to compare the response demands from the second event ground motion in the four record-pairs. The ductility factor (μ) is defined as the ratio of the maximum displacement in the EPP SDOF to its yield displacement from response history analysis. The nonlinear pseudo acceleration (A_y) is defined as $A_y = \omega_n^2 u_y$ [45], where u_y is the yield displacement of the nonlinear SDOF.

The normalized A_y spectra in Fig. 2-3 suggest that as μ increases, the point at which the spectral values of the aftershock ground motions exceed those of the mainshocks shifts towards lower periods. If the equal displacement rule holds, a higher ductility factor means that yielding in the SDOF happens at lower intensities. Consequently, because of period elongation, such a system would be more sensitive to the low-frequency contents of the records where, conditioned on similar $\mathbf{M}, R$, V_{s30} and ε, the spectral demand in aftershock ground motions are expected to be higher than those of mainshock records (Fig. 2-2b). This implies that structural systems with higher levels of ductility (as it is the case with most modern code-conforming frame structures) and moderate to long periods may undergo higher seismic demands when subjected to aftershock ground motions compared to mainshock records. The constant-ductility median response spectra of the second records in the SS-MS-AS and MS-MS sets are also compared in Fig. 2-3. Even though the second-event ground motions in the SS-MS-AS set are on average 0.4 **M** smaller than those in the MS-MS set, the median A_y values from the former approach the latter at periods above approximately 2 seconds. Later, we will examine the implications of these observed differences in the

characteristics of mainshock and aftershock ground motions on the seismic performance of the five RC frame buildings.

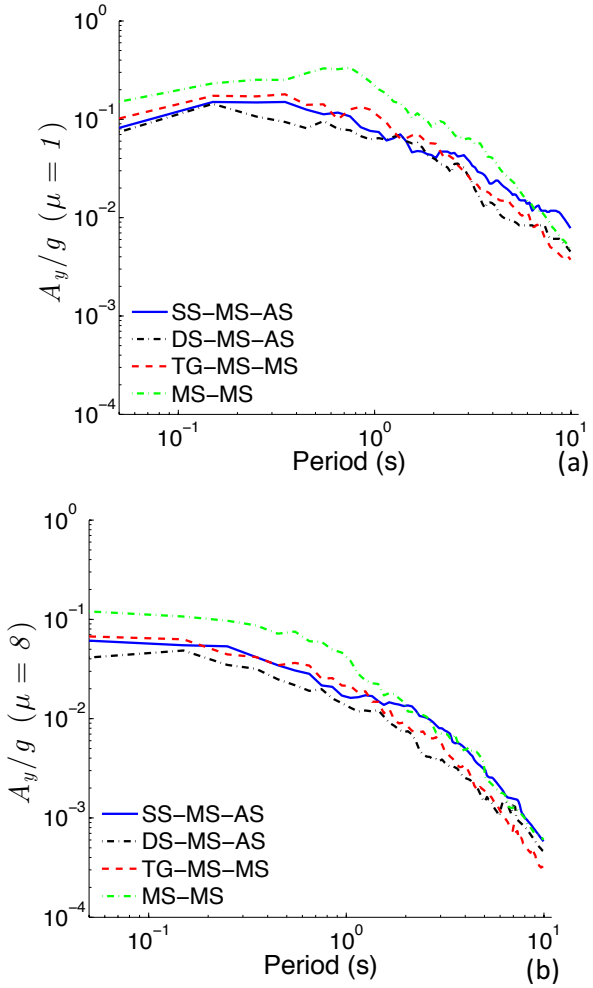

Fig. 2-3. Comparing the median constant-ductility response spectra for the second ground motions in the SS-MS-AS, DS-MS-AS, TG-MS-MS and MS-MS record sets for SDOFs with a) $\boldsymbol{\mu = 1}$ and b) $\boldsymbol{\mu = 8}$

2.3 Mainshock-Aftershock Structural Response and Seismic Performance Assessment

The mainshock-aftershock structural response and seismic performance of a set of RC moment frames is assessed in this section. The goal is to quantify the effects of different record-pairs on story drift demands, collapse risk and vulnerability.

2.3.1 Building Descriptions and Structural Modeling

Five modern, code-conforming RC moment-resisting frame buildings are used in this chapter. The buildings and structural models, adopted from Haselton [46], include 2-, 4-, 8-, 12- and 20-story RC moment frames designed based on the provisions of ASCE 7-05 [47]

and ACI 318-02 [48] for a high seismicity site (Site Class D) in Los Angeles. The buildings were chosen to incorporate a broad period-range (0.66s-2.63s) to evaluate whether the effects of alternate record-pairs varies across structure periods. The seismic response of the 2-story, and to a lesser extent the 4-story, structure is mostly influenced by the high frequency energy of ground motions due to their low first-mode period (T_1). A broader range of frequencies influence the response of taller buildings because of their high T_1 and the presence of significant higher-mode effects. 2-D numerical models of the buildings developed by Haselton [46] in the OpenSees platform [49] are utilized for the nonlinear dynamic analyses. Each model consists of three bays of moment-resisting RC frames. The destabilizing effect of the tributary loads on the gravity frames are included through a $P-\Delta$ column. The beams and columns are modeled as elastic elements with nonlinear flexural hinges that incorporate a trilinear backbone curve and hysteretic rules developed by Ibarra et al. [50]. Fig. 2-4. shows a schematic layout of the model. Table **2-3** summarizes the design information as well as the periods of the first two modes of each building.

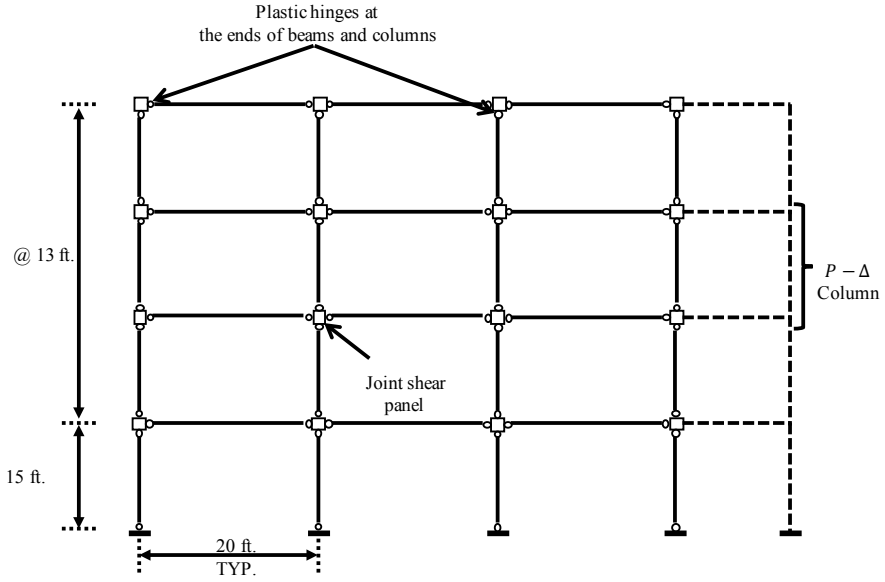

Fig. 2-4. Schematic illustration of the numerical model of the archetypes used for nonlinear dynamic analyses (after Haselton et al. [51])

Table 2-3. Base shear coefficients and periods of the first two modes of examined buildings

Building ID[a]	Number of stories	C_s[b]	$C_{s,y}$[c]	Period (seconds)	
				1st mode	2nd mode

2064	2	0.125	0.392	0.66	0.18
1003	4	0.092	0.143	1.12	0.33
1011	8	0.050	0.077	1.71	0.57
1013	12	0.044	0.075	2.01	0.68
1020	20	0.044	0.070	2.63	0.85

[a] From Haselton et al. [51]
[b] Design base shear coefficient
[c] Yield base shear coefficient

2.3.2 Mainshock and Aftershock Seismic Hazard Analysis

Probabilistic seismic hazard analysis (PSHA) is performed for a site in Southern California, east of downtown Los Angeles (Lat: 33.996, Lon:-118.162). We originally performed PSHA for the selected location using the tool provided by the United States Geological Survey (USGS) [52], including deaggregation to identify the 50 sources that contribute the most to the seismic hazard. We then implemented those 50 sources in a MATLAB code to perform PSHA, using fault properties (latitude, longitude, slip rate etc.) provided by USGS and OpenSHA [53] (the motivation for using the MATLAB code was to enable aftershock PSHA, as described further below). Characteristic magnitudes for each fault were calculated using relationships suggested by UCERF3 [54]. The source geometries and magnitude-recurrence models adopted in this study are simpler than contemporary California seismic source models like UCERF3 [54], but account for the characteristic magnitudes that each source can generate.

The rate of aftershocks decays with time following the causative mainshock [28]. Aftershock probabilistic seismic hazard analysis (APSHA) [11] were performed utilizing a nonhomogeneous recurrence Poisson process with a rate that accounts for the temporal decay in the rate of aftershocks in lieu of a time-independent recurrence assumption made by the conventional PSHA [11]. The parameters that define the spatial distribution of earthquake magnitudes and the temporal decline in the rate of aftershocks are based on the generic California model by Reasenberg and Jones [55]. The magnitude of the largest aftershock is

assumed to be equal to that of the largest mainshock. The minimum magnitude is taken as 5 since events with smaller magnitudes are not expected to induce notable damage in code-conforming structures.

Whereas PSHA considers contributions from all 50 sources, the aftershock hazard is computed for the condition that a mainshock event has occurred; for this purpose, the single fault that contributes the most to the seismic hazard at the location of the building was selected, which is the Los Angeles segment of the Puente Hills fault. The APSHA hazard curves are therefore conditioned on a mainshock rupture of that segment, and a time window of one year following the mainshock. Fig. 2-5 presents the resulting mainshock and aftershock hazard curves that were used to design the buildings. The IM utilized for the hazard analyses is the spectral acceleration at the first mode period of the structure being examined $\left(S_a(T_1)\right)$.

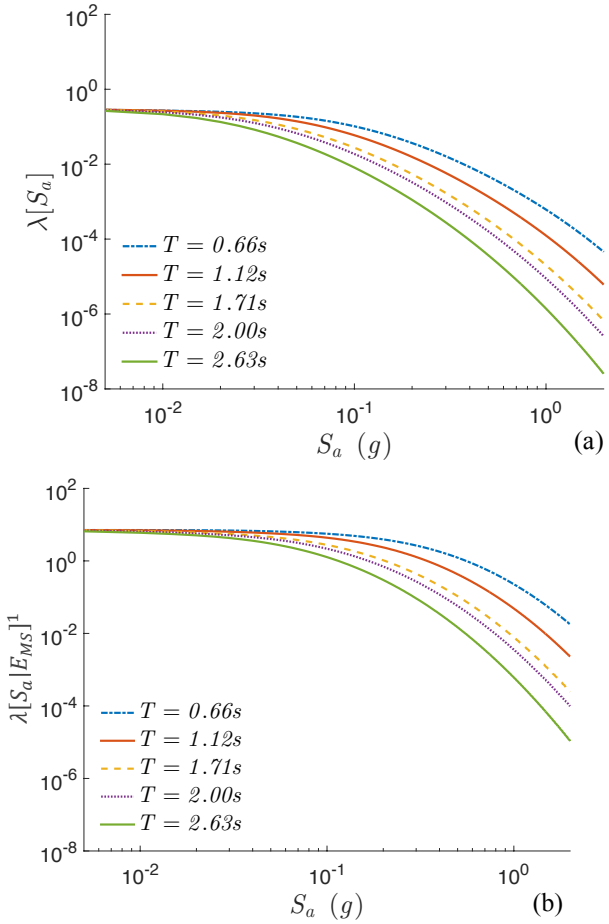

Fig. 2-5. (a) Mainshock and b) Aftershock1 hazard curves corresponding to the fundamental period of the five studied structures

[1] E_{MS} in Fig. 2-5b stands for a mainshock event with a specific magnitude.

2.3.3 Impact of Correlation Between 'Parent' and 'Children' Events in a Seismic Sequence on SDR

In this section, we examine the possible impact of correlation between ground motions from parent mainshock events and their and children aftershock events. Correlation effects have been observed previously on ground motion intensity measures [27]; the present focus is on the maximum SDR of the RC moment frame structures subjected to ground motions from those event sequences.

As discussed before, record selection for this investigation produced 620 recordings from 17 parent mainshocks and 27 children aftershocks and a separate set with 474 only-mainshock ground motions from 18 events. SDR is computed for each nonlinear response history analysis using the five structure models. For a given structure model, we relate the natural log of SDR to the independent variables of moment magnitude (**M**), closest distance to surface projection of fault (R_{JB}), site parameter (V_{S30}) and dummy variables related to fault type (1 for strike slip, 2 for normal slip and 3 for reverse slip) using the following expression (modified from Boore and Atkinson [56]):

$$\ln(SDR) = c_1(\mathbf{M} - 6.6) + c_2 SS + c_3 NS + c_4 RS + c_5 \left(\ln\left(\sqrt{R_{rup}^2 + h^2} - 1\right)\right) + c_6 \ln(V_{s30}/760) \quad (2.1)$$

where SDR is the geometric mean of the two SDRs obtained for the two perpendicular components of the ground motion and c_{1-6} and h are coefficients computed through regression. The regression was performed using the two-step procedure of Joyner and Boore [57] and Joyner and Boore [58], which provides for an event-specific mean misfit, which is similar to an event term in a GMM developed using mixed effects regression. The mean misfit in this case is referred to as the between-event SDR residual, δW_{SDR}. Note that δW_{SDR} is an event property, and as such represents the average misfit of the recordings from that event (as applied in the present analyses) relative to the model in Equation 2.1. Fig. 2-6. shows the predicted maximum SDR values from Equation 2.1 for the 2- and 20-story buildings as a function of distance for three magnitudes. The predicted values are for a strike slip fault and $V_{s30} = 760\, m/s$. The regression coefficients as well as the intra- and inter-event residuals obtained from the two-stage regression analysis are presented in Appendix A.

We investigate correlation between EDPs produced by mainshock and aftershock ground motions by computing correlation coefficients between δW_{SDR} terms for parent mainshocks and their respective children aftershocks. Results of these analyses are provided in Table **2-4**,

which indicates correlation coefficients between 0.10 and 0.32 for the various structural models. To provide a baseline against which these correlations can be compared, we use the second set of 474 mainshock δW_{SDR} terms from 17 events as follows: (1) calculate δW_{SDR} from mainshocks; (2) split the set of 17 events into six parent and eleven children events; (3) each parent event is assigned two children events; and (4) calculate the correlation coefficient of the paired values from Step 3. The resulting correlation coefficients, shown on the right side of Table **2-4**, range from 0.01-0.20 and are always lower than those for the properly paired MS-AS events. The differences observed in the two sets of correlation coefficients indicate that correlation of parent-to-child event ground motions is a potentially relevant factor at the EDP level. If so, then DS-MS-AS and TG-MS-MS pairings, which would not be expected to preserve this correlation structure, would be problematic. This issue is explored further when the collapse performances of the buildings are investigated.

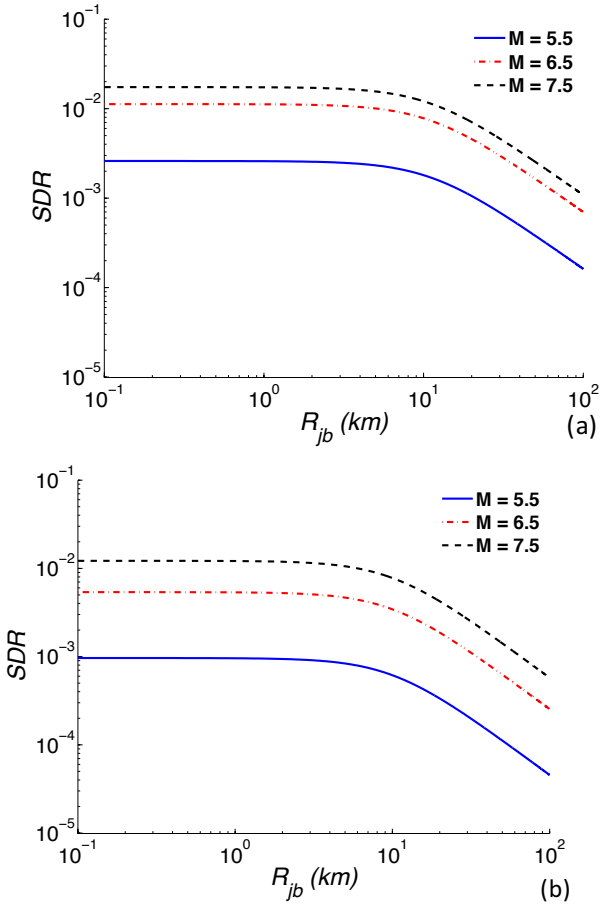

Fig. 2-6. Trends between maximum SDR and distance for three magnitudes for the a) 2-story and b) 20-story buildings

Table 2-4. Correlation coefficients between actual and randomly-assigned 'parent' and mean 'children' SDR event terms

Building	Correlation coefficient between SDR

	event terms	
	Actual	MS-MS
2-story	0.10	0.03
4-story	0.22	0.09
8-story	0.32	0.20
12-story	0.23	0.11
20-story	0.13	0.01

2.4 Collapse Performance Assessment

2.4.1 Methodology

Buildings that have been subjected to a mainshock event and sustained structural damage are usually not repaired during the short period immediately following the mainshock when the rate of aftershocks is highest. This, coupled with the accumulation of structural damage under successive aftershock events, results in significant uncertainty regarding the state of a structure when aftershocks occur. The Markov process [59] accounts for this uncertainty in the state of the structure. The steps that one needs to take to perform seismic risk assessment under sequential ground motions are discussed in details in Chapter 3. Here, a brief overview of the risk assessment methodology adopted in this chapter is given.

Each element P_{ij} of the Markov transition matrix in Equation 2.2 is the probability of transitioning from damage state i when the building is subjected to a seismic event to damage state j under the successive earthquake.

$$\Pi = \begin{bmatrix} P_{11} & P_{12} & \cdots & P_{1r} \\ 0 & P_{22} & \cdots & P_{2r} \\ \vdots & \vdots & \ddots & \vdots \\ 0 & 0 & \cdots & P_{rr} \end{bmatrix} \tag{2.2}$$

Damage states become incrementally more severe as the index of the transition probabilities increases. The Markov transition matrix in Equation 2.2 is of the upper triangular form as no repair measure is assumed to take place to restore the building to a less severe damage state during the time the building is subjected to aftershocks. The last element in each row in Equation 2.2 represents the probability of the most extreme limit state, which herein is defined as collapse. Each element P_{ij} in Equation 2.2 can be obtained using Equation 2.3.

$$P_{ij} = \int \left(P_{i,j}^{DS}\left[EDP > edp_j | IM\right] - P_{i,j+1}^{DS}\left[EDP > edp_{j+1} | IM\right] \right) d\lambda_{IM}(im) \quad (2.3)$$

In Equation 2.3, the integrand is the probability of the structure being in damage state j given that it has already experienced damage state i when subjected to the previous event. λ_{IM} is the mean rate of exceedance of the intensity measure (IM) that links the response of the building to the seismic hazard at the building's location and can be obtained through APSHA. The time-variant rate of aftershocks implies that, in the aftershock environment, the P_{ij} term in Equation 2.3 will be a function of the elapsed time since the mainshock's occurrence. Consequently, the Markov transition matrix in Equation 2.3 is also time-dependent.

An implicit assumption in Equation 2.3 is that, during the time window for which the performance is being evaluated, the likelihood of more than one event triggering the damage state transition is negligible. Therefore, use of Equation 2.3 in the post-mainshock environment requires discretization of time into sufficiently short intervals such that no more than one aftershock is likely within each interval. According to the Markov process [60], at time step m following the mainshock, the probability that the structure is in damage state j given that damage state i has already occurred under the mainshock is equal to the element on row i and column j of matrix P^m in Equation 2.4.

$$P^m = \prod_{i=1}^{m} \Pi^i \quad (2.4)$$

Evaluation of seismic performance without conditioning on the occurrence of a mainshock (i.e., in the pre-mainshock environment) must account for uncertainties in the occurrence of the mainshock as well as the state of the structure following the mainshock. This can be done by multiplying the limit state transition matrix in Equation 2.4 by a vector of P_i^{MS} values as illustrated in Equation 2.5. The vector of P_i^{MS} values represents the probability of the structure being in damage state $i, i = 1, \dots, r$ (where r is the most severe limit state) under mainshock ground motions. The elements of the vector P_i^{MS} can be calculated by integrating building fragility curves obtained by subjecting the building to mainshock ground motions ($P_{MS}^{DS}[EDP > edp_i | IM] - P_{MS}^{DS}[EDP > edp_{i+1} | IM]$ in Equation 2.6) together with the seismic hazard curve obtained through mainshock PSHA (λ_{IM} in Equation 2.6).

$$P^m = (P_1^{MS}, \dots P_r^{MS}) \prod_{i=1}^{m} \Pi^{\mathrm{i}} \tag{2.5}$$

$$P_i^{MS} = \int (P_{MS}^{DS}[EDP > edp_i|IM] - P_{MS}^{DS}[EDP > edp_{i+1}|IM]) d\lambda_{IM}(im) \tag{2.6}$$

To obtain collapse fragility curves for the five buildings, we begin by performing nonlinear response history analyses on the structural models using the first ground motion in each record-pair. The goal of this step is to induce a certain level of SDR in the structure. Four incrementally-increasing damage states, as well as the intact state under the first ground motion in each pair, are targeted. These states range from intact to 5% maximum story drift ratio (SDR_{GM1}). The five SDR_{GM1} values serve as proxies for the possible states of structural and non-structural damage under a mainshock ground motion. Table 2-5 summarizes examples of structural and non-structural damage states associated with each of the SDR_{GM1} values. These four levels of SDR values together with the intact state also serve as the possible damage states that the building could be in under each of the ground motions in a cluster of seismic events before collapse occurs. In other words, they are necessary for populating the elements of the Markov transition matrix in Equation 2.2. Collapse state is defined as the point of dynamic instability or where maximum SDR exceeds 10% [51].

P_{MS}^{DS} values required as input to Equation 2.6 are obtained by fitting a lognormal fragility curve to each of the five damage states [59]. Next, a nonlinear response history analysis is performed using the second ground motion in the record-pairs, to obtain the post-mainshock capacity of the damaged building for each of the maximum SDR_{GM1} values from the previous step. The second-event ground motions are scaled to twelve different $S_a(T_1)$ levels. These S_a values, together with the maximum SDR values obtained by subjecting the building to the scaled aftershocks, are used to estimate the fragility curves needed to compute $P_{i,j}^{DS}[EDP > edp_j|IM]$ in Equation 2.3 using the method described in Baker [61].

Table 2-5. Limit state description

SDR	Damage state description[1]
1%	Severe cracking in partition walls, cracking in floor slabs
2%	Minor damage in beams and columns
2.75%	Concrete cracking and spalling in beams and columns

5%	Significant concrete spalling, fracture or buckling in longitudinal reinforcement, punching shear failure in slabs

[1]From Haselton et al. [62] and FEMA P-58 [FEMA 20127]

2.4.2 Outcomes of Nonlinear Dynamic Analyses under Sets of Sequential Ground Motions

In this section, we compare the outputs of nonlinear dynamic analyses performed on the five structures subjected to the four sets of mainshock-aftershock records shown in Table 2-1. These comparisons are directed towards (1) evaluating whether appropriately selected mainshock records can be used as the second ground motion in a sequence and (2) for the case where aftershock records are used to represent the second event in the sequence, examining the impact of mainshock-aftershock ground motion correlation. We investigate the first question by comparing results from TG-MS-MS and SS-MS-AS record sets; whereas the latter serves as the benchmark against which other options are compared, the former uses only mainshock records but maintains appropriate magnitude and distance relationships between the first and second ground motion (details in Table 2-1). The second question is investigated by comparing results from DS-MS-AS and SS-MS-AS record pairs, the former of which lacks between-record correlation.

Specific results utilized for the aforementioned comparisons are two-fold. First, we consider collapse fragilities for structures subjected to second-event ground motions, conditional on first-event damage levels. These results in effect represent the structural collapse capacity that remains following a mainshock, and hence are independent of relative aftershock ground motion amplitudes at the conditioning intensity measure. The second comparison is of collapse rates, derived from the Markov method presented before.

2.4.2.1 Fragility Curves for Four Ground Motion Sets

Fig. 2-7. shows collapse fragility curves for the 4- and 20-story structures using the benchmark SS-MS-AS ground motions and $S_a(T_1)$ as the conditioning ground motion intensity measure. The 'intact' results in Fig. 2-7. represent a condition of no damage from the mainshock (all damage results from aftershocks). The other results in Fig. 2-7. represent varying levels of mainshock-damaged states as represented by SDR_{GM1} values ranging from 1-5%. Median collapse capacities ($\hat{S}a_{col}$) for the intact structures are 0.70g and 0.40g for the 4- and 20-story buildings, respectively. As expected, performance worsens ($\hat{S}a_{col}$ decreases)

as SDR_{GM1} increases. These reductions are appreciable (factors of 2 to 4) for the most severe damage state, ($SDR_{GM1} = 5\%$).

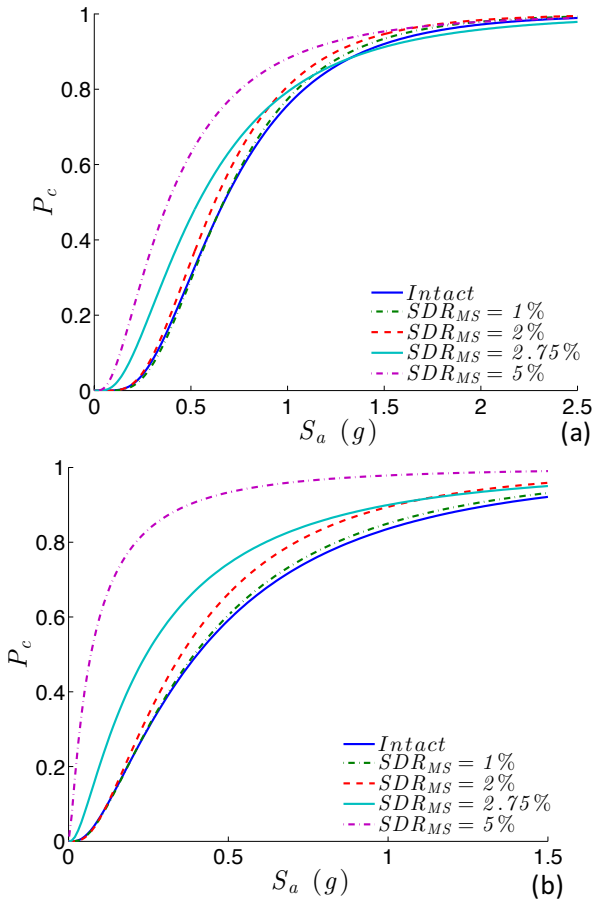

Fig. 2-7. Collapse fragility curves for the intact and incrementally-increasing mainshock-damaged states for the (a) 4- and (b) 20-story structures under the SS-MS-AS set

Fig. 2-8. compares collapse fragility curves for the 2-, 8- and 20-story structures derived using all four ground motion sets. Results are shown for the intact state under the first-event ground motions. We find the SS-MS-AS set collapses structures at lower median ground motions than other options, with MS-MS having the highest median. Keeping in mind the conditioning on $S_a(T_1)$, the variations between these results reflect spectral shape effects for $T > T_1$, with flatter spectra being more damaging and producing lower median collapse ground motions. For example, for the 20-story building with $T_1 = 2.6s$, the steepness of the spectral decay for $T > T_1$ in Fig. 2-2b is ordered as MS-MS > DS-MS-AS > TG-MS-MS ~ SS-MS-AS, which mirrors the median collapse ground motion levels in Fig. 2-8. b. Similar effects are observed for other buildings and conditioning first-event damage levels. This sensitivity to spectral shape occurs because in a nonlinear structure, the role of periods beyond T_1 become more important to the dynamic response as nonlinearities lengthen the first mode period. Depending on the dynamic characteristic of the structure, higher modes of

response with periods smaller than that of the first mode could also have a significant influence on the seismic response.

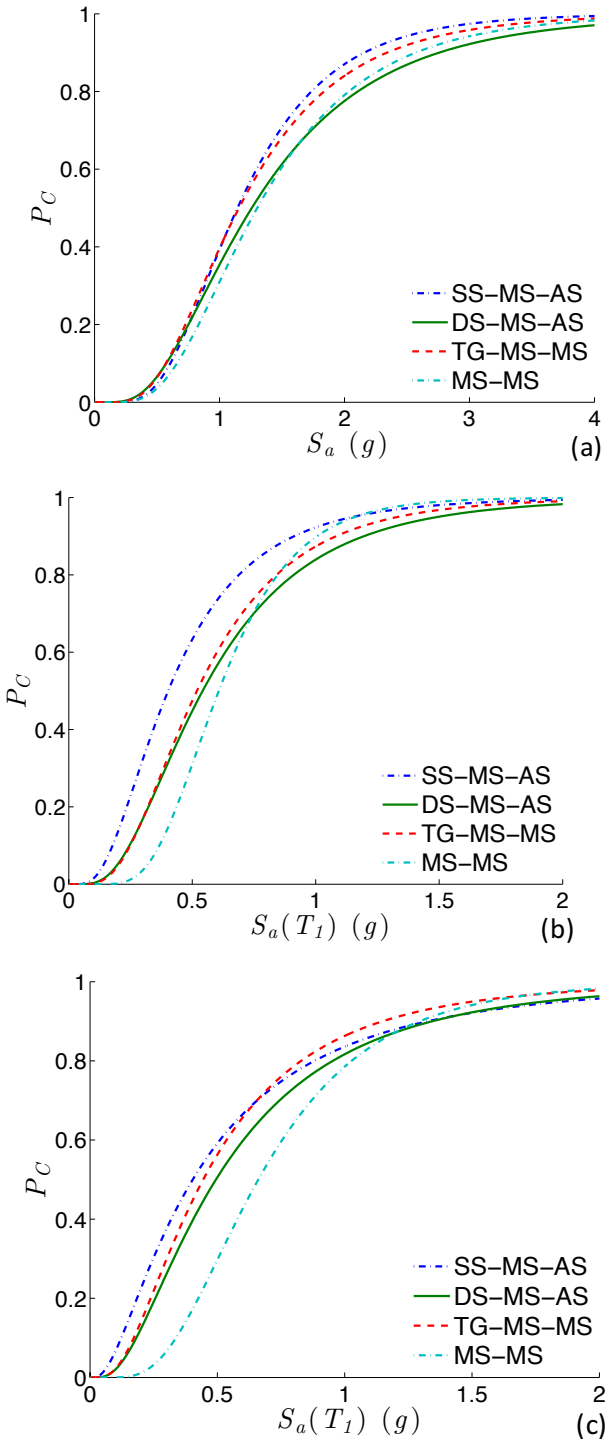

Fig. 2-8. Collapse fragility curves of (a) 2- and (b) 8-story and (c) 20-story structures under the four record-pair sets in the intact state after the first event ground motions

Based on these results, we offer the following findings regarding the two questions from the Introduction:

- Whereas MS-MS ground motions are clearly not suitable, we generally find TG-MS-MS to have similar spectral shapes to those for SS-MS-AS, and hence to produce similar collapse fragilities.
- For the range of structures considered, DS-MS-AS spectra are often slightly steeper than SS-MS-AS, resulting in higher collapse capacities. However, the differences are small and may not be statistically significant. This result is consistent with the weak (but repeatedly observed) parent-to-child event correlation.

2.4.2.2 Service Life Collapse Probabilities

We compute collapse probabilities ($\hat{P}_C$) by convolving the fragility curves from Fig. 2-7. with hazard curves for the example site (Fig. 2-5). Hazard curves at $S_a(T_1)$ do not change between ground motion sets, hence variations of $\hat{P}_C$ are solely a result of the different fragilities. Because the Markov model used to compute $\hat{P}_C$ considers multiple damage states following the mainshock event, multiple versions of the fragility curves for a given structure enter into the calculation.

We consider a lifespan of 50 years for the $\hat{P}_C$ calculation with the results in Fig. 2-9. and Fig. 2-10. . The collapse probability at each time step is obtained using the Poisson distribution in Equation 2.7, where the rate of the collapse limit state (λ_c) is obtained through Equation 2.5. An underlying assumption in Equation 2.7 is that the building will be restored to its pre-damaged state after an event sequence (mainshock and the following aftershocks). In other words, while the state of the building under successive aftershocks is modeled probabilistically, its state before the occurrence of the next cluster of mainshock and aftershock events is modeled deterministically. Based on this assumption, the probability of collapse is computed as:

$$\hat{P}_c = 1 - e^{-\lambda_c T} \tag{2.7}$$

Fig. 2-9. compares $\hat{P}_C$ for the five structures subjected to the SS-MS-AS and TG-MS-MS record sets. For the 2-story building (Fig. 2-9. a), the two record-pair sets yield almost identical $\hat{P}_C$ values. This result can be understood by the similarity of the nonlinear response spectra for the SS-MS-AS and TG-MS-MS record sets for periods <~2 seconds (Fig. 2-3.), which in turn produces similar collapse fragilities. Recall from Table **2-3** that the first mode period of the intact 2-story structure is 0.66 seconds, which even after lengthening is unlikely to exceed the range where the nonlinear spectra significantly differ. The 4-story building

(initial $T_1 = 1.12$s) would be expected to have a dynamic response at the collapse level that is controlled by portions of the nonlinear spectra where the SS-MS-AS set is stronger than the TG-MS-MS set, and indeed this is observed in the form of higher $\hat{P}_C$ values for the SS-MS-AS set.

Fig. 2-9. b shows that the trends between $\hat{P}_C$ obtained under the SS-MS-AS and TG-MS-MS sets for the 8-, 12- and 20-story buildings follow a similar trend to what observed before for the 4-story building. Looking at all the results in Fig. 2-9. , differences observed for the intermediate-height buildings (4, 8, 12 story) arise from differences in fragilities, which in turn are related primarily to steeper spectral shapes in the TG-MS-MS spectra vs the SS-MS-AS spectra for $T > T_1$ (Fig. 2-2b). Likewise, where $\hat{P}_C$ values are similar between groups, fragilities and spectral shapes between record groups are also similar. The longer initial and elongated T_1 of the taller buildings would put their first mode of dynamic response at frequencies where the content of the SS-MS-AS set increasingly exceeds that of the TG-MS-MS set. While the contribution of higher modes effect to the dynamic response in the taller buildings is expected to be more significant, their presence is mostly offset by the proximity of the contents of the SS-MS-AS and TG-MS-MS sets at periods close to the higher mode periods of the 8-, 12- and 20-story buildings (Table **2-3**).

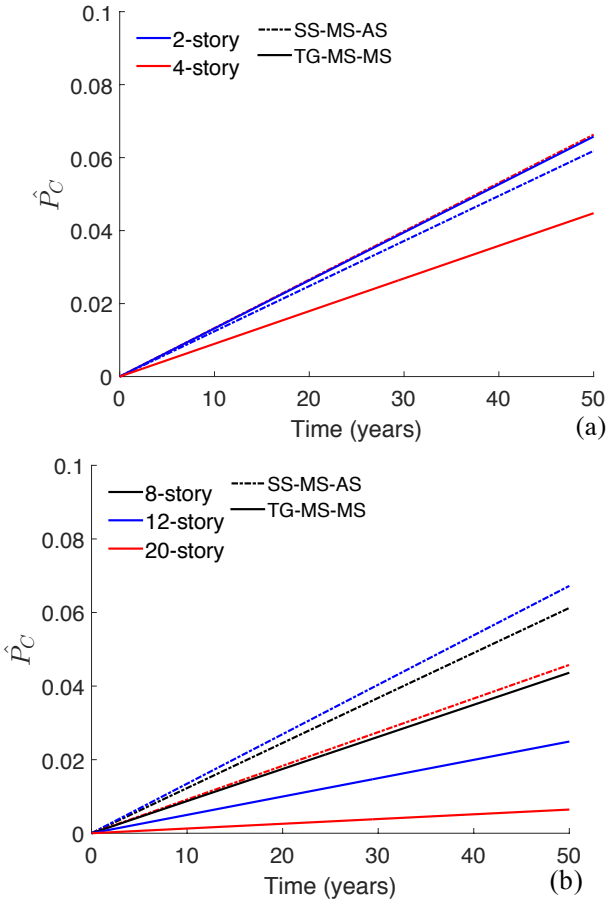

Fig. 2-9. Comparing $\widehat{\boldsymbol{P}}_{\boldsymbol{C}}$ for an assumed lifespan of 50 years for a) 2- and 4-story and b) 8-, 12- and 20-story buildings under the SS-MS-AS and TG-MS-MS sets of ground motions

Fig. 2-10. shows $\left(\hat{P}_C\right)$ values for the SS-MS-AS and DS-MS-AS sets. Differences are encountered for all cases other than the 20-story building, which is caused by different spectral shapes and consequently different fragilities, as explained above.

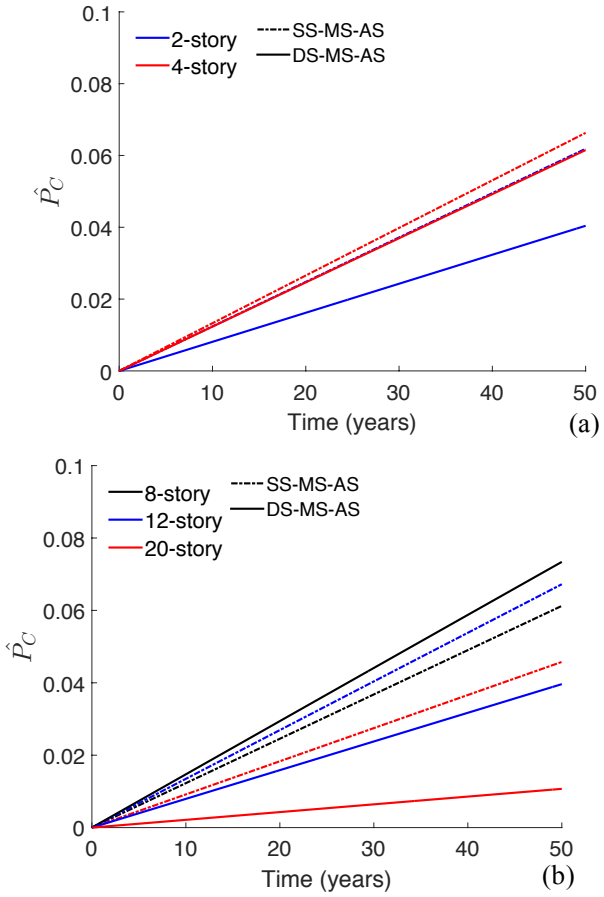

Fig. 2-10. Comparing $\widehat{\boldsymbol{P}}_{\boldsymbol{C}}$ for an assumed lifespan of 50 years for a) 2- and 4-story and b) 8-, 12- and 20-story buildings under the SS-MS-AS and DS-MS-AS sets of ground motions

2.5 Summary and Conclusion

A key to obtaining realistic assessments of the seismic performance of structures from nonlinear dynamic analysis is the proper selection of the ground motions. The selected records must, as much as possible, reflect the ground motion features that the structure is most likely to experience during its service life. In the absence of systematic guidelines for selecting record-pairs for seismic performance assessment under sequential ground motions, using mainshock ground motions to represent both mainshock and aftershock events has become a common practice. However, evidence from past studies on the differences in the frequency content of mainshock and aftershock ground motions casts doubt on the accuracy of such practice. In this chapter, we investigate the impact of two main issues related to mainshock-aftershock record selection: (1) how the frequency contents of mainshock and aftershock events differ, and (2) the presence of correlation in parent mainshock to child aftershock ground motions. The impact of both of these issues on collapse probabilities are illustrated for structures having a range of heights (2 to 20 stories).

Notable differences in the frequency content of mainshock and aftershock ground motions are observed when the elastic and inelastic response spectra of 100 records are compared. The mainshock ground motions are found to contain richer frequency content at lower periods while the aftershock records show higher spectral values at longer periods. Such observations are consistent with predictions of some prior ground motion models. These differences in frequency content produce notable differences in collapse capacities obtained from a benchmark mainshock-aftershock record set and three sets of record-pairs compiled using alternative approaches. The difference in the dynamic response of the studied buildings was found to be influenced primarily by the frequency content differences between the record-pair sets near the first mode period of the structural models.

Based on the findings presented here, we recommend that the current practice of using pairs of mainshock-mainshock ground motions for nonlinear dynamic analysis be discontinued. However, an exception can be made when mainshock records are selected in such a way that they have comparable magnitude, distance, and frequency content to aftershock records, which is achievable through the TG-MS-MS scheme describe above. However, when possible, we recommend use of SS-MS-AS record sets, which places a premium on documentation of aftershock ground motions following major events as ground motion databases continue to expand and develop.

Past studies have reported a mild correlation between the event terms of the ground motions recorded from parent and children events. We demonstrate this effect as being present in the displacement-based EDP of maximum SDR, although the correlation is modest. Not surprisingly, we encounter modest but persistent differences between collapse fragilities and probabilities for the SS-MS-AS and DS-MS-AS record sets. As a result, we consider the use of DS-MS-AS ground motions sub-optimal in comparison to SS-MS-AS, due to aforementioned differences that most often produce an unconservative bias.

2.6 Appendix

Table 2-6 summarizes coefficients $\boldsymbol{c_{1-6}}$ and $\boldsymbol{h}$ obtained through regression analysis on the SDR prediction equation presented in Equation 2.1. Fig. 2-11 shows the intra- and inter-event residuals for the 2- and 20-story buildings obtained in the first and second stages of the two-step regression analysis described before.

Table 2-6. Regression coefficients of Equation 2.1

Building	c_1		c_2	c_3	c_4	c_5	h	c_6
	$\mathbf{M} \leq 6.6$	$\mathbf{M} > 6.6$						
2-Story	1.46	0.21	-1.24	1.74	-1.54	1.25	11.81	-0.64
4-Story	1.59	0.49	-1.77	2.22	-2.21	1.14	9.15	-0.78
8-Story	1.57	0.61	-2.23	2.60	-2.73	1.10	8.02	-0.96
12-Story	1.63	0.69	-2.13	2.54	-2.60	1.21	9.08	-1.02
20-Story	1.72	0.72	-1.98	2.41	-2.43	1.31	10.67	-1.02

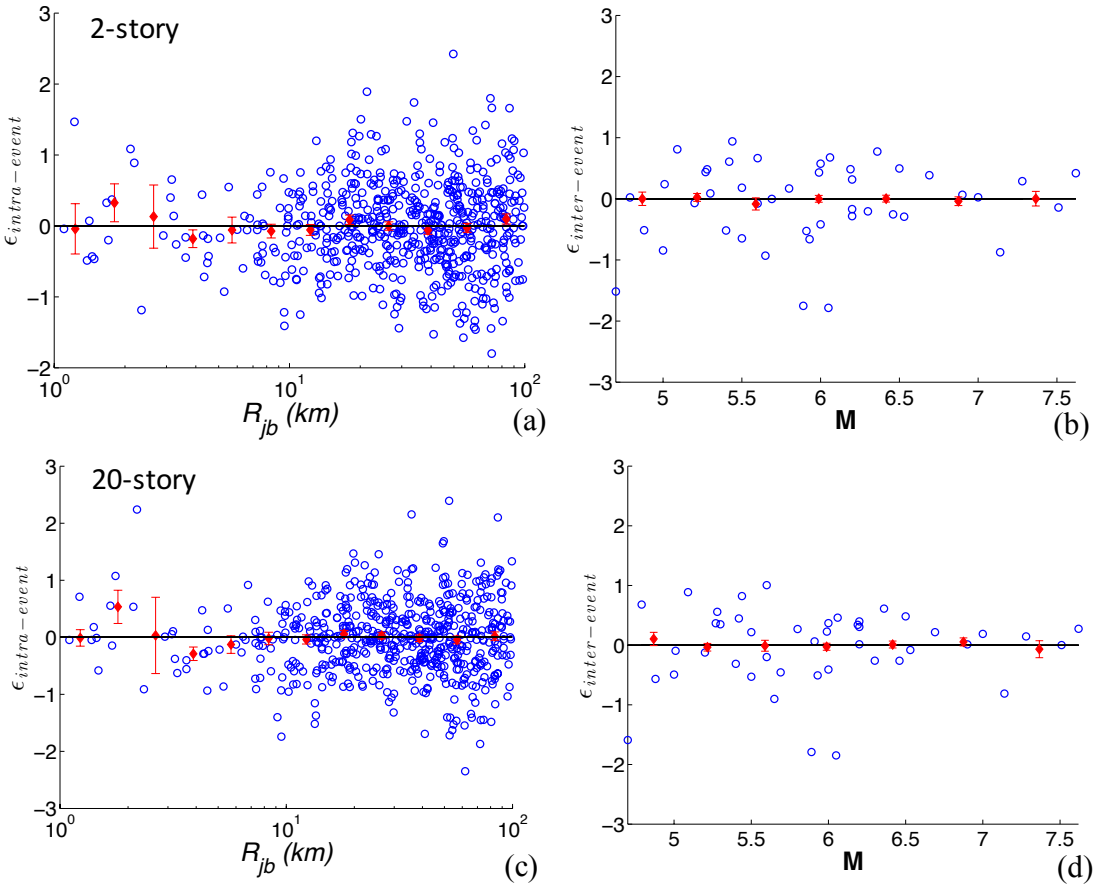

Fig. 2-11. Intra and inter-event residuals obtained from the two-stage regression analysis on the 2- and 20-story buildings

CHAPTER 3: Risk-based assessment of aftershock and mainshock-aftershock seismic performance of reinforced concrete frames

---

This chapter is adopted from the following study:

Shokrabadi, M. and Burton, H. V. (2018). "Risk-based assessment of aftershock and mainshock-aftershock seismic performance of reinforced concrete frames," *Structural Safety,* 73, 64-74.

3.1 Introduction and background

Aftershock events have been shown to exacerbate the damage caused by mainshocks and in some cases, have led to collapse [14, 63]. While aftershocks are generally smaller in magnitude than their preceding mainshock, structures can be particularly vulnerable to aftershocks due to their high rate of occurrence and the reduction in the lateral load-carrying capacity caused by mainshock-damage. In the 1999 Kocaeli earthquake, several buildings that survived the mainshock, which had a moment magnitude (M_w) of 7.4, collapsed during a M_w 5.9 aftershock, which occurred one month later, killing seven people and injuring more than two hundred [64]. The aftershocks that followed the 2008 Wenchuan earthquake damaged 196 dams and claimed more lives. The 2010 M_w 7.1 Darfield earthquake was followed by M_w 6.2 and M_w 6.0 aftershocks, which resulted in 185 fatalities and damaged approximately 100,000 buildings in the city of Christchurch [6]. The five aftershocks with M_w over 7 that followed the 2011 Tohoku earthquake caused additional damage to infrastructure, liquefaction and loss of lives [3].

The risk of aftershock collapse also influences the post-mainshock decisions of owners and occupiers regarding re-occupancy of damaged buildings, thereby affecting the recovery process [63]. A large portion of the central business district in Christchurch was evacuated due to the perceived aftershock collapse risk posed by several damaged buildings [65], resulting in widespread business disruption and substantial indirect losses [66].

In recent years, significant advances have been made in classifying mainshock-aftershock (MS-AS) sequences (e.g., Wooddell and Abrahamson [8]), characterizing their spatial and temporal distribution, and quantifying the time-dependent hazard associated with aftershock events [9-11]. Moreover, recent databases developed as part of the Next Generation

Attenuation (NGA) ground motion projects (particularly NGA-West2 [67], and NGA-Subduction) have increased the availability of recorded ground motions from MS-AS sequences. However, the structural engineering community is still in the early stages of leveraging these developments. While the threat posed by aftershocks is now well recognized, research to quantify the associated risk is still in its infancy, particularly with regards to integrating the time-dependent aftershock hazard with the increased vulnerability to collapse of damaged buildings.

Most studies to date on aftershock performance have focused on quantifying the change in vulnerability experienced by buildings subjected to mainshock damage. Li and Ellingwood [68] examined the damage in the lateral force resisting elements caused by sequential ground motions in 9- and 20-story steel moment frames. Two ground motion suites were selected to represent seismic events with 10% and 2% probability of exceedance in 50 years. They found that the extent of damage under the aftershocks had a higher correlation with the extent of damage under the mainshocks rather than the intensity of the mainshock. Ruiz-García and Aguilar [69] subjected a 4-story steel moment frame building to 14 ground motion pairs from the 1994 Northridge earthquake. Five levels of residual SDR were targeted under the mainshock records followed by collapse analysis under the aftershock ground motions. A reduction of up to 20% in the collapse capacity was observed as the residual story drift ratio under the mainshocks increased to up to 2%.

The performance of reinforced concrete (RC) moment frames under sequential ground motions has also been investigated in several studies. Hatzigeorgiou and Liolios [70] evaluated the response of a set of ductile and non-ductile RC moment frame structures to as-recorded and artificially-generated ground motion sequences. An increase in the displacement demand and a change in the distribution of plastic hinges under the sequential ground motions in comparison with the single record analyses were reported. More recently, Raghunandan et al. [14] evaluated the post-mainshock collapse capacity of code-conforming RC frame buildings. Each ground motion pair in their study consisted of one single record as both the mainshock and the aftershock. For each pair, the buildings were first subjected to the mainshock ground motions to target a specific maximum story drift ratio. The median collapse capacity was reduced by up to 46% when the buildings sustained a maximum story drift ratio of 4% under the mainshocks. The relationship between the reduction in the collapse capacity and eight damage measures was examined and story drift ratios (both maximum and residual) were found to be the best indicators of the reduction in the collapse capacity when the buildings were subjected to a mainshock seismic event. In another study, Jeon et al. [16]

proposed a framework for developing aftershock damage fragility curves for RC frames. The methodology was applied to a set of three non-ductile RC frames and fragility curves were developed for five different damage states, ranging from cosmetic repair measures to replacing structural members. A direct relationship between the damage sustained during mainshocks and the extent of damage under aftershocks was observed. The vulnerability to aftershock damage was shown to increase with building height. Other noteworthy studies on aftershock performance assessment include those by Luco et al. [71], Bazzurro et al. [72], Maffei et al. [73], Ryu et al. [15], Nazari et al. [13], Han et al. [74] and Tesfamariam et al. [75].

A common theme in above-mentioned studies is that they all involved vulnerability-based assessments and did not consider time-dependent aftershock hazard and subsequent risk. It is well established that the rate of seismic events increases significantly after the occurrence of a large-magnitude mainshock [28]. This elevated seismic hazard, combined with the reduction in structural capacity caused by the mainshock damage, can increase the seismic risk to buildings and communities already affected by a major mainshock seismic event.

A necessary step in performing risk-based assessment is the characterization of seismic hazard. Yeo and Cornell [11] used the empirical relationship that describes the exponential decay of aftershocks [55] to formulate a PSHA methodology for quantifying the aftershock seismic hazard at a site given the occurrence of a mainshock. Other aftershock PSHA methodologies developed by Boyd [10] and Iervolino et al. [9] are aimed at predicting the combined seismic hazard due to mainshocks and aftershocks before the occurrence of a causative mainshock. Such methodologies would prove useful when there is a need to account for the aftershock seismic hazard in the design or retrofit of a structure.

Several studies have taken the necessary steps to address the time-dependent nature of seismic risk in the aftershock environment. Yeo and Cornell [76] proposed a methodology for estimating life-time financial losses due to sequential seismic events. Ebrahimian et al. [77] formulated a framework to account for the fact that the transition between discrete structural limit states in the post-mainshock environment is a function of the number of aftershock events that are likely to happen during the time window that the seismic performance is being evaluated. Iervolino et al. [78] examined the application of a state-dependent Markov approach in evaluating time-dependent limit state exceedance probabilities for SDOF systems. Nazari et al. [79] developed a methodology to assess the necessary changes in

structural design to account for aftershock hazards. The methodology was applied to a 2-story woodframe building and the authors found that an approximately 10% increase in strength and stiffness was needed when aftershock collapse risk was considered.

The current chapter seeks to perform a risk-based assessment of the aftershock and mainshock-aftershock (MS-AS) seismic performance of code-conforming RC frame buildings. Section 3.2 describes the steps involved in formulating a time-dependent seismic risk evaluation approach using non-stationary Markov transition probability matrices. The need for such a time-dependent framework for seismic risk assessment is also discussed in Section 3.2. The mainshock and aftershock seismic hazard at a high-seismicity site in Southern California are assessed using the conventional seismic hazard analysis as well as the method proposed by Yeo and Cornell [11] in Section 3.3. The latter seismic hazard assessment method allows for the explicit consideration of the time dependency of seismic hazard in the post-mainshock environment. Hazard curves are developed using the spectral acceleration at the initial first mode period of the structures $\left(S_a(T_1)\right)$ as the intensity measure. Interested readers are referred to Luco and Cornell [32], Tothong and Luco [80] and Eads et al. [81] for alternative intensity measures that could reduce the computational cost of response history analysis and improve the outcomes of seismic risk assessment. A description of the reinforced concrete moment-frame buildings including the structural modeling is presented in Section 3.4. Nonlinear response history analyses are performed using a set of carefully-selected MS-AS sequences (Section 3.5). All the selected ground motion pairs are from the as-recorded ground motions that are designated as MS-AS sequences based on time and distance windowing algorithms [8]. The outcomes of the seismic hazard assessment and response history analyses are combined using the methodology formulated in Section 3.2 to estimate the aftershock and MS-AS seismic risk for the RC frame buildings (Section 3.5).

3.2 Formulating limit state exceedance probability under sequential seismic events

The performance-based earthquake engineering (PBEE) framework comprehensively addresses the limit state exceedance probability (P_{LS}) calculation. The PBEE methodology assumes that the state of the structure prior to the occurrence of the seismic event is known (usually the structure is assumed to be in the intact state) and the structure will return to its pre-damaged state before the next earthquake occurs. These assumptions are valid when the seismic performance is evaluated under major mainshock events. The time interval between major mainshock events is usually long enough to allow for affected buildings to be restored

to their pre-mainshock state. However, buildings that have been subjected to a major mainshock event and sustained a level of structural damage are usually not repaired during the short time period immediately following the mainshock when the rate of occurrence of aftershocks is at its highest. This, coupled with the accumulation of structural damage under successive post-mainshock events, adds to the uncertainty in determining the state of a structure before being subjected to each of the damaging aftershocks. As such, evaluating the seismic performance of structures subjected to sequential seismic events requires explicit consideration of the uncertainty in the state of the structure after being subjected to any of the events in a cluster of a mainshock and subsequent aftershocks.

Assuming that the state of the structure under event i in the sequence only depends on its state under the event $i-1$ and is independent of its states under the events that precede event $i-1$, a Markov process approach is appropriate for quantifying the probability of transitioning from one damage state to the next [63, 78]. The uncertainty in the state of the structure in the Markov process is accounted for through the Markov transition matrix whose elements comprise of the probabilities of transitioning between r predefined limit states as shown in Equation 3.1.

$$\Pi = \begin{bmatrix} P_{11} & P_{12} & \cdots & P_{1r} \\ 0 & P_{22} & \cdots & P_{2r} \\ \vdots & \vdots & \ddots & \vdots \\ 0 & 0 & \cdots & 1 \end{bmatrix} \tag{3.1}$$

The P_{ij} terms in Equation 3.1 represent the probability that the structure transitions to damage state j when subjected to an event in the cluster given that it has already experienced damage state i under the previous event. The damage states become incrementally more severe as the index of the transition probabilities increases. The Markov transition matrix in Equation 3.1 is of the upper triangular form as no repair measure is assumed to take place to restore the building to a less severe damage state. The steps necessary to be taken if repair is assumed plausible in the post-mainshock environment are discussed in Yeo and Cornell [63]. The diagonal element in each row of the transition matrix is the probability that there is no state-transition when the structure is subjected to a seismic event. Thus, by this definition, the diagonal element in each row is the complement of the remaining damage state transition probabilities in that row and can be readily calculated given the off-diagonal terms in that row. The $P_{ij}, j > i$ terms of the transition matrix Π in Equation 3.1 can be calculated using Equation 3.2 [63].

$$P_{ij} = P_S\left(\int \left(P_{i,j}^{DS}\left[EDP > edp_j|IM\right] - P_{i,j+1}^{DS}\left[EDP > edp_{j+1}|IM\right]\right) f_{IM}(im)dim\right) \quad (3.2)$$

In Equation 3.2, $P_{i,j}^{DS}\left[EDP > edp_j|IM\right] - P_{i,j+1}^{DS}\left[EDP > edp_{j+1}|IM\right]$ is the probability of the structure being in damage state j given that the structure has already undergone damage state i when subjected to the preceding event. P_S is the probability of occurrence of the seismic event on the seismic source on which the occurrence of an earthquake would trigger the transition from damage state i to damage state j. $f_{IM}(im)$ is the source-specific probability density function (PDF) of the IM that links the response of the building to the seismic hazard at the building's location, which can be obtained through probabilistic seismic hazard analysis while accounting for all possible significant earthquake scenarios of different magnitudes and source-to-site distances. The decline in the rate of aftershocks with the time elapsed since the occurrence of the causative mainshock is well documented in the literature [28]. Such a temporal decay in the rate of aftershocks is typically modeled using the modified Omori's law [28]. APSHA [11] utilizes a nonhomogeneous recurrence Poisson process with a rate that accounts for the temporal decay in the rate of aftershocks in lieu of a time-independent recurrence assumption made by conventional PSHA. This time-variant rate for aftershocks implies that, in the aftershock environment, the P_{ij} term in Equation 3.2, and consequently the Markov transition matrix in Equation 3.1 will be functions of the elapsed time since the mainshock's occurrence.

As discussed before, in the post-mainshock environment the structure is expected to undergo successive aftershock events during a relatively short period of time without being restored to the pre-damaged state. Thus, each element P_{ij} of the transition probability matrix needs to be calculated by accounting for all the possible transition scenarios where different numbers of aftershocks are likely to happen. This can be done by reformulating Equation 3.2 to take the form shown in Equation 3.3. $P_s(N_{AS} = w)$ in Equation 3.3 is the probability that w aftershocks occur on the contributing source during the time interval after the mainshock for which the seismic performance is being evaluated. The $\sum_{l=1}^{w}\left(P_{ij}^{l}\prod_{o=1}^{l-1}\overline{P_{ij}^{o}}\right)$ term accounts for the fact that the limit state j needs to be exceeded only once when the building is being subjected to a sequence of w aftershocks. The P_{ij}^{l} probabilities are obtained using Equation 3.4 where the $P_{i,j}^{DS}\left[EDP > edp_j|IM, N_{AS} = l\right]$ terms in Equation 3.3 can be calculated by subjecting the structure to l sequential aftershock ground motions in a back-to-back analyses. The $\overline{P_{ij}^{o}}$ terms in Equation 3.3 are simply the complements of the P_{ij}^{o} probabilities $\left(\overline{P_{ij}^{o}} = 1 -\right.$

$P_{ij}^{o}\big)$ [77]. This approach can be adopted if there are significant differences in the frequency content of successive ground motions, which would affect the response of a structure subjected to an earthquake sequence.

The $P_s(N_{AS} = w)$ probability in Equation 3.3 can be obtained using the nonhomogeneous Poisson probability distribution outlined in Equation 3.5 and the process that describes the limit state transition probabilities will be an independent semi-Markov process [60]. Unlike a Markov process, finding the relationship that defines the limit state transition probabilities in successive intervals in a semi-Markov process is not straightforward and usually an analytical relationship similar to Equation 3.9 derived for a Markov process does not exist for a semi-Markov process [60]. However, the problem of finding such an analytical relationship will become much simpler with a change of variable that defines time (t) that would transform the nonhomogeneous Poisson of Equation 3.5 to a homogeneous Poisson process in the new variable space. In the new variable space, Equation 3.8 can be used to calculate limit state transition probabilities in successive intervals. Such a variable transformation is described in Yeo and Cornell [76]. Time in the new variable space $\big(\tau(t)\big)$ can be calculated as $\tau(t) = \int_0^t \mu_{AS}(0,u)du$. μ_{AS} can be calculated through Equation 3.6 which provides a relationship to calculate the mean number of aftershocks on the contributing seismic source with minimum and maximum magnitudes of M_0 and M_m (M_m is usually taken as the mainshock's magnitude) and is obtained by combining the modified Omori's law for the daily rate of aftershocks and the Gutenberg-Richter's relationship for magnitude distribution [11, 55]. t_0 and t_1 in Equation 3.6 mark the start and end of the time window during which μ_{AS} is being calculated and are defined assuming that the occurrence of the mainshock marks the origin of time, a and b are constants that characterize the magnitude distribution and c and ρ are constants that define the temporal decay in the number of aftershocks.

$$P_{ij} = \sum_{w}\left(P_s(N_{AS} = w)\sum_{l=1}^{w}\left(P_{ij}^{l}\prod_{o=1}^{l-1}\overline{P_{ij}^{o}}\right)\right) \tag{3.3}$$

$$\begin{aligned} P_{ij}^{l} = \int \big(P_{i,j}^{DS}\big[EDP > edp_j|IM, N_{AS} = l\big] \\ - P_{i,j+1}^{DS}\big[EDP > edp_{j+1}|IM, N_{AS} = l\big]\big)f_{IM}(im)dim \end{aligned} \tag{3.4}$$

$$P_s(N_{AS} = w) = \frac{(\mu_{AS})^w}{w!}e^{-\mu_{AS}} \tag{3.5}$$

$$\mu_{AS}(t_0, t_1) = \left(10^{a+b(M_m - M_0)} - 10^{a}\right) \frac{(t_1 + c)^{1-\rho} - (t_0 + c)^{1-\rho}}{1 - \rho} \tag{3.6}$$

A major challenge in using Equation 3.3 for seismic risk assessment is the computational cost associated with performing consecutive response history analyses to calculate the P_{ij}^{l} terms. As an alternative, Equation 3.3 can be simplified if the time intervals $[t_0, t_1]$ are chosen to be small enough such that no more than one aftershock is likely within each interval. In this case, P_s and $P_{i,j}^{DS}\left[EDP > edp_j | IM, N_{AS} = l\right]$ are simplified to μ_{AS} and $P_{i,j}^{DS}\left[EDP > edp_j | IM\right]$, respectively. In this approach, a pair of a mainshock and a single aftershock is selected as a representative of a real seismic sequence which usually includes multiple aftershocks. If the characteristics and frequency contents of the aftershocks in a seismic sequence are distinct enough to warrant the involvement of multiple aftershocks in seismic risk assessment, Equation 3.3 can be used to calculate the elements of the Markov matrix of Equation 3.1.

Under the assumption of no more one aftershock in each time interval, Equation 3.3 is simplified to the more familiar form shown in Equation 3.7.

$$\begin{aligned} P_{ij}(t_0, t_1) = \mu_{AS}(t_0, t_1) \int \left(P_{i,j}^{DS}\left[EDP > edp_j | IM\right]\right. \\ \left. - P_{i,j+1}^{DS}\left[EDP > edp_{j+1} | IM\right]\right) f_{IM}(im) dim \end{aligned} \tag{3.7}$$

The Markov transition matrix, which incorporates the effect of the temporal decay in the rate of aftershocks on the limit state transition probabilities, will be "non-homogeneous" or "non-stationary" in time. The elements of the time-dependent Markov transition matrix $\left(\Pi(t_0, t_1)\right)$ in Equation 3.8 can be obtained through Equation 3.7.

$$\Pi(t_0, t_1) = \begin{bmatrix} P_{11}(t_0, t_1) & P_{12}(t_0, t_1) & \cdots & P_{1r}(t_0, t_1) \\ 0 & P_{22}(t_0, t_1) & \cdots & P_{2r}(t_0, t_1) \\ \vdots & \vdots & \ddots & \vdots \\ 0 & 0 & \cdots & 1 \end{bmatrix} \tag{3.8}$$

At time step m after the occurrence of the mainshock, the probability that the structure is in damage state j given that it has already undergone damage state i under the mainshock is equal to the element on row i and column j of matrix P^m in Equation 3.9.

$$P^m = \prod_{i=1}^{m} \Pi(t_{i-1}, t_i) \tag{3.9}$$

The above relationships provide a probabilistic framework for evaluating seismic performance in the post-mainshock environment. Such an evaluation is useful for characterizing the seismic risk in structures that have already sustained some level of damage under a major seismic event and can be subsequently subjected to a series of aftershocks. A structure is in its most vulnerable state during the period immediately following a major mainshock due to the substantial temporary increase in seismic activity and the reduction in lateral load carrying capacity caused by mainshock damage. Hence, it might be worthwhile to consider the additional seismic hazard posed by aftershocks during the design of a structure. A framework for seismic risk assessment due to sequential events in the pre-mainshock environment would follow the same logic as the process discussed above for the post-mainshock risk evaluation. However, unlike the post-mainshock risk evaluation, in the pre-mainshock environment the state of the structure once subjected to a future mainshock is unknown. Moreover, the occurrence of aftershocks is conditioned on the occurrence of the causative mainshock whose occurrence needs to be probabilistically modeled through conventional PSHA. This uncertainty in both the state of the structure once subjected to the mainshock as well the occurrence of the mainshock events can be incorporated into the Markov process by multiplying the aftershock limit state transition matrix in Equation 3.9 by a vector of $P_{i,n}^{MS}$ values as shown in Equation 3.10. The summation in Equation 3.10 is on the all the seismic sources (N_s) that contribute to the seismic hazard at the site location of the building. The vector of $P_{i,n}^{MS}$ values represents the probability of the structure being in damage state $i, i = 1, \dots, r$ under mainshock ground motions.

$$P_{PreMS}^{m} = \sum_{n=1}^{N_s} \left(\left(P_{1,n}^{MS}, \dots P_{r,n}^{MS}\right) \prod_{i=1}^{m} \Pi_n(t_{i-1}, t_i) \right) \tag{3.10}$$

The steps to calculate $P_{i,n}^{MS}$ are similar to what was discussed earlier for P_{ij}. Each element of the P_n^{MS} vector $\left(P_{i,n}^{MS}\right)$ can be obtained by subjecting the structure to the mainshock ground motions such that they would induce a target damage level ($P_{MS}^{DS}[EDP > edp_i|IM] - P_{MS}^{DS}[EDP > edp_{i+1}|IM]$ in Equation 3.11). f_{IM}^{n} in Equation 3.11 is the PDF of the IM and can be obtained through the mainshock hazard curve for seismic source n.

$$P_{i,n}^{MS} = \int (P_{MS}^{DS}[EDP > edp_i|IM] - P_{MS}^{DS}[EDP > edp_{i+1}|IM]) df_{IM}^{n}(im) \tag{3.11}$$

3.3 Mainshock and aftershock seismic hazard analysis and ground motion selection

3.3.1 PSHA and APSHA

As discussed before, this study utilizes the APSHA approach by Yeo and Cornell [11] to develop aftershock seismic hazard curves. Conventional seismic hazard analyses [82] is also performed to develop mainshock seismic hazard curves. The adopted PSHA and APSHA approach uses source and magnitude models that, while simpler relative to the USGS models, account for all the sources that contribute to the seismic hazard at the location of the building as well as the characteristic magnitude that each source can generate. The PSHA and APSHA is done using a MATLAB code written by the first author with the properties of the faults (latitude, longitude, slip rate etc.) adopted from the United States Geological Survey (USGS) [52] and OpenSHA [53] and the characteristic magnitude of each fault is calculated using the relationships suggested by UCERF3 [54].

The seismic hazard analyses are performed for the high seismicity site in Southern California that was the basis of the building designs (Fig. 3-1) [46]. The parameters that define the spatial distribution of the earthquake magnitudes as well as the temporal decline in the rate of aftershocks are adopted from the generic California model by Reasenberg and Jones [55] ($a = -1.67$, $b = 0.91$, $c = 0.05$ days and $\rho = 1.08$). The ground motion prediction equation by Boore and Atkinson [56] is used to estimate the mean and standard deviation of the lognormal distribution of the IM at each magnitude and distance. The magnitude of the largest aftershock is assumed to be equal to that of the largest mainshock. The minimum magnitude is taken as 5 as events with smaller magnitudes are not likely to induce notable damage in modern code-conforming structures. Equation 3.12 shows the well-known relationship of conventional (mainshock) PSHA that is also utilized in this study. ν_i is the rate of occurrence of seismic events with magnitudes larger than 5.0 associated with source i and $G[IM > im|M, R, \varepsilon]$ is an indicator function whose value is one if $IM > im$ and zero otherwise. When performing APSHA, for each time interval k, ν_i is replaced with μ_{AS} from Equation 3.6.

$$\lambda_{IM}[IM > im] = \sum_{i=1}^{N_s} \nu_i \iiint_{M,R,\varepsilon} G[IM > im|\, M, R, \varepsilon]\, f_M(m) f_R(r) f_\varepsilon(\varepsilon) dM dR d\varepsilon \qquad (3.12)$$

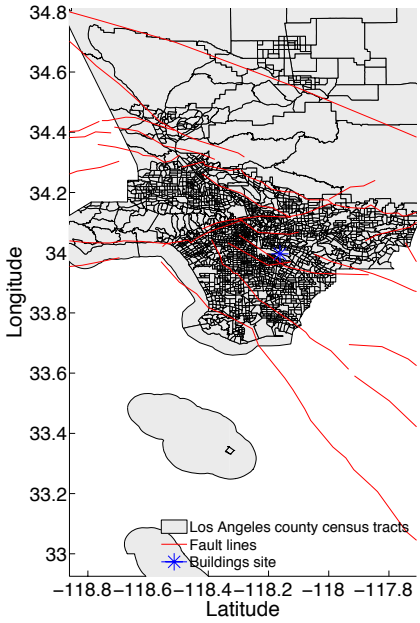

Fig. 3-1 The faults that contribute the most to the seismic hazard at the location of the buildings

Fig. 3-2 shows the hazard curves developed for the aforementioned site based on $S_a(T_1)$, where T_1 is the first mode period of the intact moment frame structure (see description in Section 3.4). The two hazard curves shown in Fig. 3-2 are calculated using (1) conventional PSHA and (2) considering only aftershocks in the post-mainshock environment (APSHA). The mainshock hazard curve is developed using conventional PSHA and incorporating the contribution of all significant faults to the total seismic hazard at the site. On the other hand, the aftershock hazard only considers the fault that contributes the most to the seismic hazard at the location of the building. APSHA is based on the assumption that a mainshock has occurred and the seismic hazard due to the following aftershocks is being calculated. Since it is very unlikely for simultaneous ruptures to happen on multiple faults that participate in the seismic hazard at the site, the single fault that dominates the mainshock hazard is used in APSHA. Deaggregation of the site seismic hazard, which was performed using the tool provided by the USGS, shows that the Los Angeles section of the Puente Hills fault is the main source of seismic hazard. Therefore, the APSHA hazard curves presented in Fig. 3-2 are obtained solely for this fault. The APSHA hazard curves are calculated for a time window of one year starting immediately after the occurrence of the mainshock. A notable difference between the mean annual frequency of exceedance of the spectral acceleration ($\lambda[S_a]$) of the PSHA and APSHA hazard curves can be observed in Fig. 3-2. Such a significant increase in the seismic hazard after a major earthquake is supported by historical evidence from past events. For instance, the 2011 M_w 9 Tohoku earthquake was followed by five hundred and

six aftershocks with magnitudes larger than 5, eighty-two with magnitudes larger than 6 and five with magnitudes 7 or larger within a three-month period after the occurrence of the mainshock [3]. A similar increase in seismic activity was also reported after large earthquakes in California [83].

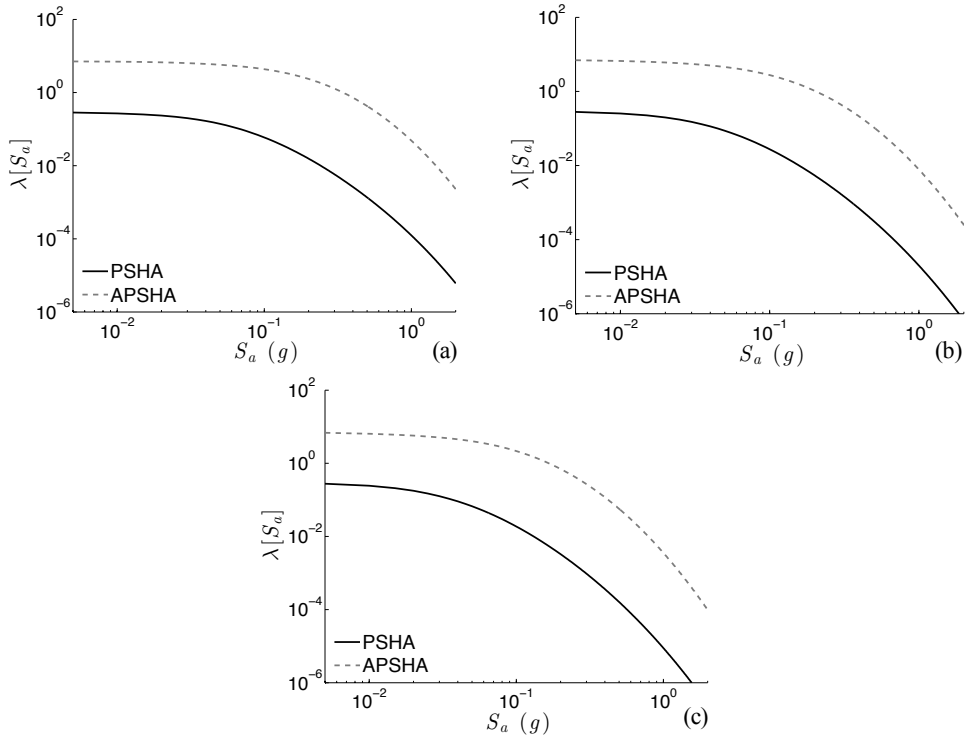

Fig. 3-2 Mainshock and mainshock-aftershock seismic hazard curves developed for a) $\boldsymbol{T = 1.12\ s}$, b) $\boldsymbol{T = 1.71\ s}$ and c) $\boldsymbol{T = 2.01\ s}$

3.3.2 Ground motion selection for MS-AS nonlinear dynamic analysis

As we discussed in Chapter 2, differences in the frequency content of mainshock and aftershock ground motions could have a significant impact on the outcomes of seismic performance assessment under sequential ground motions. Similar findings have also been reported in other studies [23, 36, 37] Goda [29] compared the collapse performance of a 2-story wood-frame building under both MS-MS and MS-AS ground motion pairs. The MS-MS sequence used the same records in the second event as in the first. The MS-MS sequence produced higher collapse probabilities than MS-AS. Ruiz-García [22] did a similar study using two low- and mid-height steel frames and reached the same conclusion. In developing a ground motion prediction equation, Abrahamson et al. [36] found that the median of spectral values of aftershocks at short periods are smaller than those from similar mainshocks, whereas at longer periods (> 0.75 sec) the aftershock spectral ordinates were larger. Chiou and Youngs [37] also reached a similar conclusion. Based on the documented differences in

the frequency content of mainshock and aftershock ground motions and the impact on the mainshock-aftershock seismic performance of structures, 24 record-pairs of real as-recorded MS-AS ground motion pairs are used in the study for sequential response history analysis.

The aftershock records are selected from the ground motions that are specifically identified as the aftershocks of major seismic events through the use of time and distance windowing algorithms [8, 84]. The ground motion pairs are from the Class 1 (mainshock) and Class 2 (aftershock) records of the Northridge, Livermore, Coalinga, Landers, Mammoth Lakes 01, Whittier Narrows, Darfield and Chi-Chi earthquakes, which are available in the PEER-NGA West2 database [67]. A magnitude-dependent time window and a distance threshold of 40 km measured in terms of the centroidal Joyner-Boore distance [8] is used to identify the aftershock ground motions following a mainshock event. The magnitudes of the events that produced the selected ground motions range from 5.8 and 7.62 for mainshocks and 5.2 and 6.46 for aftershocks. Pulse-like ground motions are excluded from the set of 24 record-pairs. Table 3-1 summarizes the properties of the records in each ground motion sequence. The response spectra of the mainshock and aftershock ground motions are shown in Fig. 3-3.

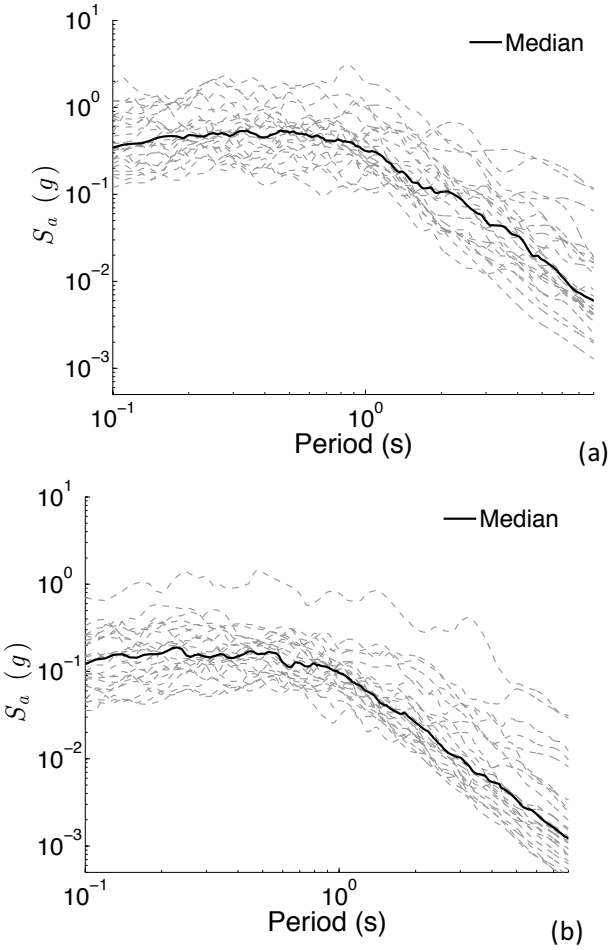

Fig. 3-3 Response spectra of a) mainshock and b) aftershock ground motions

Table 3-1. Properties of the mainshock-aftershock ground motion sequences

Sequence ID	Event name	Mainshock ground motion			Aftershock ground motion		
		M_w	R_{jb} (km)	V_{s30} (m/s^2)	Mw	Rjb (km)	Vs30 (m/s^2)
1	Northridge	6.69	12.39	545.66	5.2	20.08	508.08
2	Livermore	5.8	23.92	403.37	5.42	27.76	517.06
3	Livermore	5.8	15.19	377.51	5.42	26.07	367.57
4	Coalinga	6.36	7.69	257.38	5.38	12.89	352.2
5	Landers	7.28	69.21	382.93	6.46	76.13	416.15
6	Landers	7.28	2.19	1369	6.46	47.6	328.09
7	Landers	7.28	23.62	353.63	6.46	34.98	296.97
8	Mammoth Lakes 01	6.06	12.56	537.16	5.94	41.75	370.94
9	Whittier Narrows	5.99	18.32	266.9	5.27	22.21	316.02
10	Whittier Narrows	5.99	14.95	271.9	5.27	19.12	301
11	Whittier Narrows	5.99	18.23	301	5.27	23.98	297.07
12	Whittier Narrows	5.99	11.07	329.06	5.27	22.93	270.96
13	Whittier Narrows	5.99	16.77	241.41	5.27	21.82	267.35
14	Whittier Narrows	5.99	24.61	302.73	5.27	27.55	311.86
15	Umbria Marche	6	35.79	492	5.5	35.83	492
16	Darfield	7	43.6	638.39	6.2	85.42	638.39
17	Darfield	7	11.86	344.02	6.2	71.47	485.04
18	Darfield	7	1.22	344.02	6.2	5.52	187
19	Chi-Chi	7.62	3.12	542.6	6.2	36.38	378.7

				1			5
20	Chi-Chi	7.62	14.82	378.7	6.2	33.86	573.0
				5			4
21	Chi-Chi	7.62	12.6	573.0	6.2	35.78	233.1
				4			4
22	Chi-Chi	7.62	0.11	496.2	6.2	40.79	492.2
				1			6
23	Chi-Chi	7.62	27.57	665.2	6.2	49.36	665.2
24	Chi-Chi	7.62	43.17	459.3	6.2	75.92	225.7
				2			7

3.4 Numerical models

Three modern, code-conforming RC moment-resisting frame buildings are used for this study. The building models are adopted from the set of models developed by Haselton [46]. The buildings are designed following the provisions of ACI 318-02 and ASCE 7-05 [ASCE 47, ACI 48]. The design requirements of Chapter 21 of ACI 318-02 for the seismic design of special moment frames are also adopted. To investigate the effect of building height on aftershock and MS-AS collapse risk, 4-, 8- and 12-story buildings are used. The variation in height would provide a means to more thoroughly study the relationship between the reduction in structural capacity and increase in seismic hazard in the post-mainshock environment. The lateral force-resisting system for each of the studied buildings consists of a three-bay perimeter moment frame. Two-dimensional nonlinear models of the buildings are constructed using the OpenSees platform [49] (Fig. 2-4). $P-\Delta$ effects are incorporated with a leaning column. Beams and columns are represented with flexural plastic hinges at the member-ends connected through an elastic element. The nonlinear behavior of the flexural hinges is modeled using the trilinear backbone curve developed by Ibarra et al. [50], which is capable of capturing both in-cycle and cyclic strength and stiffness deterioration. While the plastic hinge model is unable to account for axial-flexure interaction, its ability to capture strength and stiffness deterioration has strong implications to the residual capacity of the structure after a seismic event [46]. The properties of the plastic hinges are obtained through the empirical relationships developed by Haselton [46]. The joint shear panels are modeled with an elastic element as the detailing requirements for special moment frames are expected to prevent shear failure in the joints. Key building properties are summarized in Table **3-2**. It is worth noting that the use of a two-dimensional model to simulate the seismic response of a building structure has its limitations. Three dimensional effects such as bi-axial bending in columns and accidental torsion are not captured. Moreover, ignoring the contribution of

gravity frames could potentially underestimate the strength and stiffness of the structure [62]. More detailed information on the design and structural modeling approach and its limitations can be found in Haselton et al. [62].

Table 3-2. Properties of the studied buildings[a]

Building ID	Stories	$T_1(s)$[b]	C_s[c]	Yield base shear coefficient	Ω[d]
1003	4	1.12	0.0	0.143	1
1011	8	1.71	0.0	0.077	1
1013	12	2.01	0.0	0.075	1

[a] From Haselton et al. [85]
[b] First-mode period
[c] Design base shear coefficient
[d] Static overstrength factor

3.5 Nonlinear dynamic analysis

3.5.1 Nonlinear dynamic analysis under sequential ground motions for collapse risk assessment

As discussed in Section 3.2, to simplify the limit state probability calculations, the time window after mainshock during which the seismic performance of the buildings is evaluated is broken into small intervals such that no more than one aftershock will be likely during each interval. The first interval marks the limit state transition from immediately after the building is subjected to a mainshock event to the first time that the building is subjected to a following aftershock. Any limit state transition in the subsequent time steps would happen solely under the aftershock ground motions. As such, the elements of the Markov transition matrix in Equation 3.8 that represent the limit state transition probabilities at the first time step need to be obtained by subjecting the buildings first to the mainshock ground motions and then to the following aftershock records; whereas, the elements of the Markov transition matrices in all the following intervals are obtained by subjecting the buildings only to the aftershock ground motions.

In this study, performance of the three described buildings is evaluated using a two-step nonlinear response history analysis approach. The goal of the first step is to induce a certain level of maximum SDR in the structure. Ten maximum SDR levels, ranging from 0.5% to 5% with 0.5% increments [14], as well the intact state are targeted in this stage. A twelfth and final damage state is defined as the global collapse point where dynamic instability occurs in

the structure or maximum SDR exceeds 10%. These twelve limit states define the possible states of building damage after being subjected to mainshock or aftershock ground motions and will be used in two stages of performance evaluation. First, in calculating the elements of the $\left(P_{1,n}^{MS}, \ldots P_{r,n}^{MS}\right)$ vector in Equation 3.10, the target SDR levels serve as proxies for the limit states that the **intact** buildings are likely to experience when subjected to the mainshock ground motions. Second, for populating the elements of the Markov transition matrix, the target SDR levels serve as proxies for the limit states that the **damaged** buildings are likely to experience when subjected to the aftershock ground motions.

To obtain the $P_{i,n}^{MS}$ values that are necessary to perform pre-mainshock MS-AS risk assessment (Equations 3.10 and 3.11), stripe analysis [61] is used. For each of the three structures, the mainshock ground motions are scaled to twenty incrementally-increasing spectral accelerations at the first mode period of the building (ranging from 0.05g to 2.5g) and nonlinear response history analyses are performed. The maximum story drift ratios obtained at the twenty spectral acceleration levels are used in a maximum likelihood method to estimate the medians and standard deviations of the lognormal distributions that define the eleven non-intact damage states described earlier [61].

The next step involves obtaining the limit state transition probabilities ($P_{i,j}^{DS}\left[EDP > edp_j|IM\right]$ in Equation 3.7) for each of the target damage states described before under the aftershock ground motions. To do so, once the building has sustained damage level i under either the mainshock ground motions (when calculating Markov transition matrix for the first time interval after mainshock) or the aftershock records (for Markov transition matrices of all the subsequent time intervals), the 25 aftershock ground motions are applied successively to the damaged building. The building is allowed to come to a halt between each of the two consecutive ground motions. The aftershock records are again scaled to twenty different aftershock spectral accelerations using the buildings' first mode periods as the intensity measure. These twenty spectral acceleration values together with the maximum SDR values obtained by subjecting the building to the scaled aftershocks (SDR_{AS}) is utilized to estimate the probability distribution functions needed to compute the conditional fragility curves in a manner similar to what described for obtaining fragility functions for the mainshock ground motions. The limit state probability distributions obtained in this stage together with the aftershock $\lambda_{IM}(im)$ functions discussed in Section 3.2 will be used as the inputs for Equation 3.7 to obtain the time-dependent limit state transition probabilities that form the elements of the Markov transition matrices in Equation 3.8.

Fig. 3-4a-c compare the aftershock limit state exceedance probability distributions for the 8-story building and the limit states defined before when it has already experienced three specific levels of SDR under the mainshock ground motions (SDR_{MS}). As expected, the probability of exceedance of the limit states under the aftershock ground motions increases as the structure sustains more damage under the mainshock records. For instance, the aftershock median collapse spectral acceleration declines by approximately 60% when the building sustains an SDR_{MS} of 4.0% compared to when it remains intact under the mainshock ground motions.

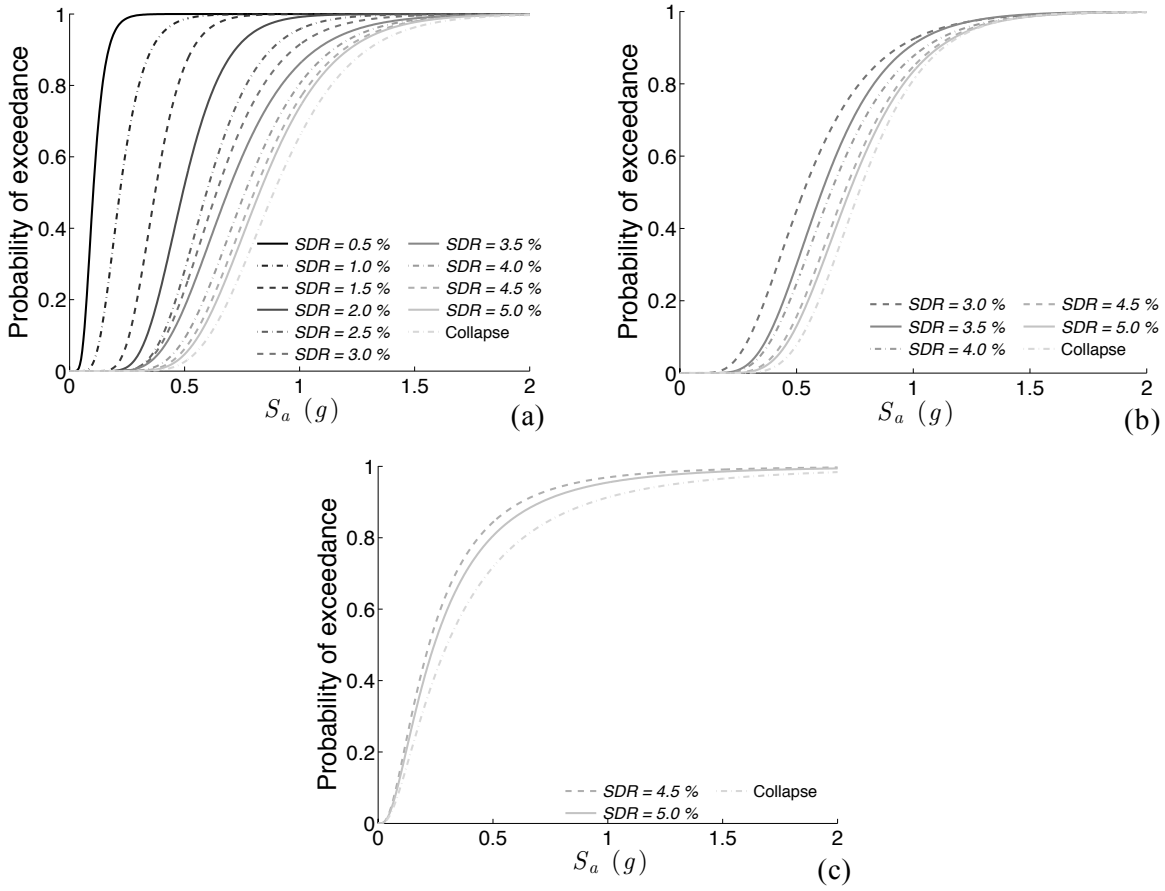

Fig. 3-4 Aftershock limit state exceedance probability distributions for the 8-story building for the initial states of a) intact, b) $\boldsymbol{SDR_{MS} = 2.5\%}$, c) $\boldsymbol{SDR_{MS} = 4.0\%}$

3.5.2 Seismic risk in the post-mainshock environment

In this section, the probability of transitioning between the twelve damage states given the time elapsed since the mainshock is used to quantify the increase in the seismic risk due to the additional hazard from aftershocks and the reduction in the structural capacity due to unrepaired damage under successive events. The transition probabilities are obtained using Equation 3.8 with the assumption that a mainshock has happened on the LA section of the

Puente Hills fault, the building is in one of the damage states defined in Section 3.5.1 and is now being subjected to the aftershocks that follow the mainshock. A period of 30 days after the mainshock is selected for the seismic risk assessment as the decline in the rate of aftershocks as well as the likely initiation of repair measures after this time window would eliminate the need for the type of aftershock risk assessment performed in this study. A value of 0.001 day is selected as the length of each of the time intervals as the occurrence of more than one aftershock on any of the contributing faults is unlikely during this time increment. Fig. 3-5. shows the how the likelihoods of the limit state transition ($P[LS]$) change in the post-mainshock environment for the 4-story building within the period of 30 days after mainshock. For brevity, the $P[LS]$ values are presented for the four limit states of intact, $SDR_{MS} = 1\%$, $SDR_{MS} = 2.5\%$ and $SDR_{MS} = 5\%$ when subjected to the mainshock ground and five limit states, from intact to collapse, under the aftershock records. The exceedance probabilities for the limit states in Fig. 3-5. show a sharp increase within the first few days after the mainshock when the rate of aftershocks is at its peak while the likelihood of the building remaining intact declines simultaneously. If the building remains intact when subjected to the mainshock ground motions (an unlikely scenario), the likelihood that it will also remain intact under the following aftershocks will be about 30% while the probability of collapse at the end of the 30-day period remains below 1%. Expectedly, as the extent of damage under the mainshock ground motion increases from **Fig.** 3-5a to **Fig.** 3-5d, the likelihood of transition to more severe damage states under the aftershock ground motions increases, too; such that collapse under the aftershock records is more than 15 times more likely when $SDR_{MS} = 5\%$ compared to when the building remains intact during the mainshock event.

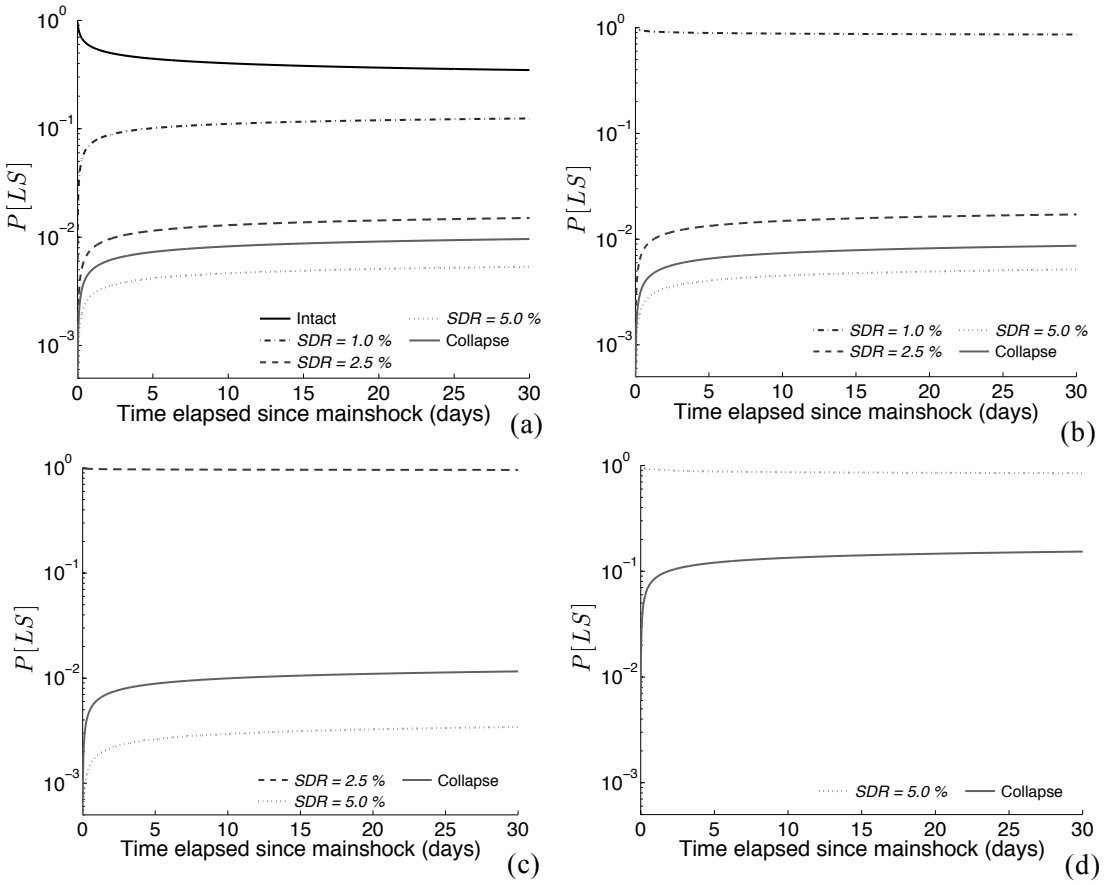

Fig. 3-5. Limit state transition probabilities in the 4-story building under aftershock records for a) intact, b) $\boldsymbol{SDR_{MS} = 1\%}$, c) $\boldsymbol{SDR_{MS} = 2.5\%}$ and d) $\boldsymbol{SDR_{MS} = 5\%}$ limit states under mainshocks

Fig. 3-6 shows how the aftershock collapse probability (P_c) changes with the extent of the demand that the buildings sustain under the mainshock ground motions. The aftershock P_c values are presented for the very end of the 30-day period during which the aftershock seismic performance is assessed. The results in Fig. 3-6 suggest that there is no noticeable increase in P_c up to an SDR_{MS} value of 2%. However, once the maximum SDR value sustained under the mainshocks passes 2%, the collapse probability under the aftershock ground motions rapidly increases, especially in the taller buildings; such that after experiencing an SDR_{MS} of 3%, the collapse probability at the end of the 30-day period will increase by a factor of 1.5 in the 4-story building while collapse will be 3 and 9 times more likely in the 8- and 12-story structures for the same SDR_{MS}. These results highlight the fact that, under these conditions, the buildings will require extensive repair and will be unsafe to occupy prior to the completion of those repairs.

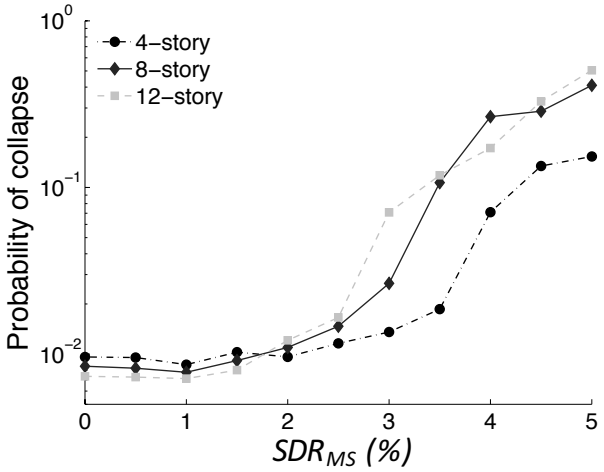

Fig. 3-6. Trends between mainshock demand and aftershock collapse probability on day 30 after mainshock in the studied buildings

3.5.3 Seismic risk in the pre-mainshock environment

This section addresses seismic performance assessment under clusters of mainshock-aftershock events in the pre-mainshock environment where the mainshock that triggers the cluster of seismic sequences has not yet happened. The limit state probabilities obtained through Equation 3.10 together with the exponential distribution of Equation 3.13 form the basis for the calculations performed in this section. The seismic risk is evaluated for an assumed service life of 50 years for all three buildings. We will refer to the approach adopted in this section for seismic performance evaluation under mainshock-aftershock sequences in the pre-mainshock environment as "Pre-Mainshock MS-AS" throughout the rest of this chapter. The contribution of aftershocks to the total hazard is again assumed significant for a period of 30 days after the mainshock occurs.

The damage state probability at each time step during the life span of the structure is obtained using the exponential distribution in Equation 3.13. The rates of the occurrence of each limit state (λ_{LS}) are obtained by multiplying the mainshock limit state probabilities obtained from Equation 3.10 for each seismic source by the mean annual rate of occurrence of mainshock seismic events on that source. Equation 3.13 can be utilized in calculating limit state transition probabilities under clusters of mainshock-aftershock events conditioned on the assumption that the building will be restored to its pre-damaged state after it sustains some level of damage when subjected to a mainshock and the following aftershocks in each cluster and before the next cluster of mainshock-aftershock events strikes the building. This assumption implies that, while the state of the building under successive aftershocks is modeled probabilistically, its state before the occurrence of the next cluster of mainshock and

aftershock events is modeled deterministically. This deterministic assumption for the state of the building at the initiation of each cluster is justified by the low λ_{LS} values (high return periods) observed for the examined buildings as listed in Table **3-3**. A low λ_{LS} (i.e., a long return period for limit state transition events compared to the lifetime of the building), would allow the building to be replaced with an intact structure before the next event that could trigger a limit state transition occurs.

$$P_{LS} = 1 - e^{-\lambda_{LS}T} \tag{3.13}$$

Table 3-3. Mean annual frequency of exceedance of limit states in the pre-mainshock environment

Building	λ_{LS} ($\times 10^{-3}$) (Return period – years)										
	$SDR =$										Collapse
	0.5%	1.0%	1.5%	2.0%	2.5%	3.0%	3.5%	4.0%	4.5%	5.0%	
4-Story	53.6 (19)	7.5 (133)	2.8 (357)	1.1 (909)	0.5 (2000)	0.2 (5000)	0.1 (1000)	0.1 (10000)	0.1 (10000)	0.2 (5000)	0.2 (5000)
8-Story	46.7 (21)	13.4 (75)	2.1 (476)	0.7 (1429)	0.4 (2500)	0.2 (5000)	0.2 (5000)	0.1 (10000)	0.0 (12500)	0.1 (10000)	0.4 (2500)
12-Story	47.5 (21)	8.1 (123)	2.3 (435)	0.6 (1667)	0.3 (3333)	0.1 (10000)	0.1 (10000)	0.1 (10000)	0.0 (12987)	0.1 (10000)	0.4 (2500)

Limit state transition probabilities in the pre-mainshock environment are also obtained under a second scenario where the transition probabilities are calculated assuming that the buildings are only subjected to the mainshock ground motions. This scenario, denoted as "Only Mainshock" herein, is similar to the approach most commonly used in the current practice and literature where the contribution of aftershocks to the total seismic risk is absent from the performance evaluation. The underlying assumptions of the Only Mainshock scenario are similar to those of the Pre-Mainshock MS-AS approach. Assuming that the building is repaired after each major mainshock event, the $P_{i,n}^{MS}$ values obtained from Equation 3.10 multiplied by the mean annual rate of seismic events of each source and summed over all the contributing sources can be used as the input rates for Equation 3.13 to calculate the Only Mainshock damage state probabilities.

Fig. 3-7 compares the transition probabilities for the $SDR = 1\%$, $SDR = 2.5\%$ and collapse limit states under the two described scenarios. The $SDR = 1\%$ is associated with

minor concrete cracking in the floor slabs of the special RC frame buildings [62] whereas the $SDR = 2.5\%$ approximately marks moderate damage in the beams and columns of the RC moment frame buildings [7]. Under both scenarios, the probability of exceeding the $SDR = 1\%$ limit state over the service life of the building is about 17% under the Only Mainshock scenario for all three structures and increases to 30% - 50% when aftershocks are considered. Over the service life, collapse is between 1.5 to 3.5 times more likely when the contribution of aftershocks is considered compared to when aftershocks are excluded from the seismic risk assessment. In fact, the lifecycle collapse probability is between 0.25% to 1.25% for the three structures when only mainshocks are considered, which is within range of the 1%-in-50 years target collapse risk that is the basis of the latest USGS design maps. It is worth noting that the buildings are designed based on the uniform hazard design ground motions in ASCE 7-02 and not the risk targeted design ground motions of the ASCE 7-10/2013 errata. However, once aftershocks are included in the risk assessment, the lifecycle collapse probability increases to 2% for the taller buildings. Such an observation highlights the role that aftershocks can potentially play in the design process of buildings in order to meet certain performance objectives in their lifetimes.

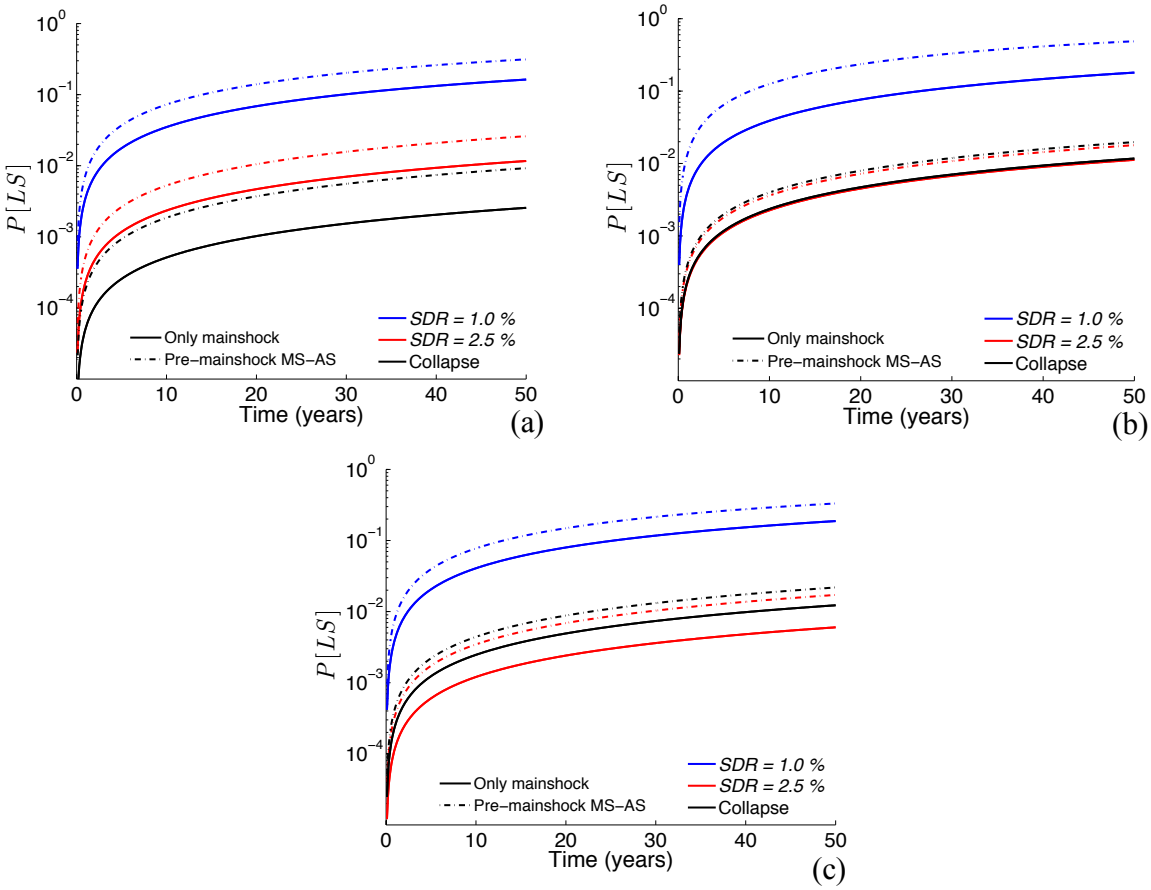

Fig. 3-7 Pre-mainshock likelihood of limit state transition in a) 4-story, b) 8-story and c) 12-story buildings

3.6 Summary and conclusion

The significant human and financial toll of mainshock-aftershock earthquake sequences on communities has highlighted the importance of considering the additional hazard that aftershocks impose on structures. While the current framework of the performance-based earthquake engineering provides a powerful tool for seismic risk assessment, it relies on the implicit assumption that the state of the structure being examined is known before the occurrence of a seismic event. Such a deterministic assumption for the state of the structure will not be valid for seismic risk assessment in the aftershock environment where structures are likely to undergo successive aftershocks during a short period of time without being restored to their pre-damaged state. Moreover, any seismic risk assessment under sequential seismic events needs to take the time-dependent nature of seismic hazard in the post-mainshock environment into account. In this chapter, a time-inhomogeneous Markov seismic risk assessment approach was adopted for seismic risk assessment that is capable of incorporating both the uncertainty in the state of the structure as well as the time-dependency of seismic hazard in the post-mainshock environment into the risk evaluation process. The

methodology leverages the ability of the performance-based earthquake engineering framework to combine a building's seismic vulnerability with its site seismic hazard through a rigorous probabilistic framework.

The Markov process was used to examine the variation in the limit state exceedance probability with time as the metric for evaluating the seismic performance of a set of special reinforced concrete moment frame subjected to mainshock-aftershock ground motion sequences. 25 pairs of ground motions were used to develop fragility curves for five structural limit states. Two scenarios were considered for the seismic performance evaluation of mainshock-damaged structures. In the first scenario, it was assumed that the mainshock earthquake has occurred and the seismic performance of the building is to be evaluated for the subsequent aftershock events. The second scenario involved assessing the performance of the building under sequential seismic events prior to the occurrence of the mainshock.

It was shown that the increase in the seismic hazard, when coupled with the reduction in the structural capacity of the mainshock-damaged buildings, would impose a significant seismic risk on the buildings in the post-mainshock environment. We also found that considering the contribution of aftershocks to the total seismic risk in the pre-mainshock environment could result in an increase of up to three times in the likelihood of collapse during an assumed lifetime of 50 years. These findings suggest that the additional seismic risk that aftershocks can potentially impose on a structure should be accounted for during the building's design process. It is important to note that the findings of the present chapter are limited to the set of buildings, ground motions and the hypothetical site described in the body of the manuscript. The impact of aftershocks on seismic risk can be more broadly quantified once the outcomes of seismic risk assessment under sequential ground motions are available for a variety of buildings, ground motions and sites with different characteristics. Moreover, due to changes in strength and stiffness as well as the contribution of higher modes to the dynamic response, a structure that undergoes significant mainshock damage is expected to have a fundamental period that is different than that corresponding to its intact first mode. As such, alternative intensity measures to $S_a(T_1)$ may prove to be a more effective (efficient and sufficient) for assessing the seismic performance of mainshock-damaged buildings and should be investigated in future studies.

CHAPTER 4: BUILDING SERVICE LIFE ECONOMIC LOSS ASSESSMENT UNDER SEQUENTIAL SEISMIC EVENTS

This chapter is adopted from the following study:

Shokrabadi, M. and Burton, H. V. (2018). "Building service life economic loss assessment under sequential seismic events," *Earthquake Engineering Structural Dynamics*, 47(9), 1864-1881.

4.1 Introduction and Background

Modern seismic design requirements primarily seek to protect life safety during a major seismic event. However, earthquake-induced direct and indirect economic losses can place a significant financial burden on stakeholders. Evaluating and designing to minimize such losses have been a topic of interest to several researchers in the recent past [86-90]. With the advancements of the second generation of performance-based earthquake engineering (PBEE) [91], there has been a growing recognition of the need to expand seismic performance objectives to include other metrics besides life safety, which are related to the general welfare of the public (e.g. [92]). While the current framework of PBEE lays the foundation for robust probabilistic seismic loss assessment, the implicit assumption of long return periods for significant seismic events renders it unsuitable for performance evaluation under sequential seismic events. Major mainshock events are known to be followed by a cluster of subsequent earthquakes referred to as "aftershocks" during a relatively short period of time. While aftershocks are generally smaller in magnitude than their preceding mainshock, their high rate of occurrence as well as the reduction in lateral load-carrying capacity caused by mainshock damage makes structures particularly vulnerable to aftershocks.

Aftershocks can exacerbate earthquake-induced financial losses by causing further damage to structural and nonstructural components in buildings that have already been affected by a mainshock event and increasing the duration of disrupted functionality. One of the most notable examples of the compounding effects of earthquake sequences in recent memory is the two **M** 6.2 and **M** 6.0 aftershocks that followed the 2010 **M** 7.1 Darfield earthquake. In addition to the 185 deaths, the combined direct and indirect losses from over 150 thousand impacted buildings added up to over 30 billion dollars [1]. Documented losses from the 1999 Chi-Chi, 2008 Wenchuan, 2011 Tohoku and 2016 Central Italy earthquakes

have also highlighted the added burden that aftershocks can impose on communities that have already experienced a major seismic event [3, 5].

Seismic loss assessment under sequential events has been partially addressed in several past studies. Yeo and Cornell [11] formulated an approach for quantifying direct and indirect losses under mainshock-aftershock seismic sequences. Through the application of a Markov process, their methodology accounts for the major sources of uncertainty when assessing building performance under sequential seismic events. The time-dependent nature of seismic hazard in the post-mainshock environment is also addressed. Jalayer et al. [93] proposed a probabilistic decision-making framework for lifecycle safety and cost analysis for civil infrastructure subjected to multiple hazards. Their methodology allows for the direct consideration of deterioration in the capacity of a structure when it is subjected to multiple events without being restored to its pre-damaged state. The multi-hazard life cycle cost analysis framework was applied to a generic RC moment frame building subjected to earthquake and blast hazards. Alessandri et al. [94] formulated a decision-making framework to support the evaluation of bridge structures in the post-mainshock environment. Both the increase in seismic hazard as well as the reduction in the structural capacity were addressed in their methodology with the possibility of updating analytical structural fragility curves with the information available on the state of the structure from field inspections. A recursive process was used by Fereshtehnejad and Shafieezadeh [95] to update limit state transition probabilities under successive loss events based on the repair time and state of the structure under the preceding event.

The focus of the current chapter is placed on formulating a framework for performing building-specific loss assessment considering mainshock-aftershock hazard and demonstrating its feasibility through application to a RC moment frame building. The proposed methodology accounts for the uncertainties in the state of the building as it is being subjected to successive seismic events. This is achieved by using a Markov approach to quantify the probability of transition between different states of damage that the building can experience when subjected to a cluster of mainshock-aftershock events.

The application of the Markov model for performing mainshock-aftershock loss assessment has been presented by Yeo and Cornell [11]. However, there are limitations in this pioneering work that we seek to address here, specifically:

1. The framework presented in this chapter adopts an alternative formulation that significantly reduces the complexity of the overall methodology.

2. The Yeo and Cornell paper used a structure that was idealized as a single-degree-of-freedom system and incorporated a single global damage measure. The current chapter utilizes a multi-degree of freedom system and incorporates structural and non-structural component-level (acceleration- and drift-sensitive) damage and loss assessment as well as disaggregation of losses in the pre- and post-mainshock environment.
3. The Yeo and Cornell study utilized the same record (from a mainshock event) as the first and second ground motion in the mainshock-aftershock sequence. In the current study, the first and second event records are taken from recordings of mainshock and aftershocks from the same sequence (e.g., Northridge earthquake mainshock and Northridge aftershocks). Prior studies [96] have demonstrated that the use of mainshock-mainshock ground motion sequence can bias the results of mainshock-aftershock building performance assessment.
4. A detailed discussion on how the contribution of different structural and non-structural elements to the total losses compare without and with the incorporation of aftershocks in loss assessment is presented in the current chapter.

For the post-mainshock scenario, the mainshock is assumed to have occurred and the building, which is in a known state of damage, is subjected to subsequent aftershocks, whereas in the pre-mainshock environment, the uncertainties in the occurrence and effect of both mainshocks and aftershocks are considered. The methodology presented in this chapter can inform pre- (e.g. component-level design strategies) and post-event decisions (e.g. timing of repairs) that would minimize the adverse effects of earthquake sequences.

4.2 methodology

Predicting building life-cycle costs considering multiple seismic sequences requires an approach that accounts for uncertainties in the hazard, accumulation of earthquake-induced damage and the resulting economic losses. PSHA is a methodology that enables direct consideration of the uncertainties in magnitude, distance and shaking intensity of future seismic events. The outcome of PSHA can be described in terms of the frequency of exceeding a range of shaking intensities over a specific time window. The PSHA methodology for mainshocks assumes a homogeneous Poisson distribution for the recurrence rate of earthquakes. However, it has been well established that the rate of occurrence of aftershocks decays with the time elapsed since the occurrence of the causative mainshock [28] and is typically modeled using the modified Omori's law [28]. Combined with the

Gutenberg-Richter relationship for the magnitude distribution of earthquakes, Yeo and Cornell [11] proposed an approach for APSHA where the constant rate of occurrence of earthquakes in conventional PSHA is replaced by a time-varying rate. In APSHA, a nonhomogeneous recurrence Poisson process is used to account for the temporal decay in the rate of aftershocks.

Another source of uncertainty in building lifecycle cost analysis is the damaged state of the building after it is subjected to earthquake shaking. The long return period of events that are generally classified as mainshocks compared to the repair and reconstruction times means that a building is most likely to be returned to its pre-damaged state before being subjected to subsequent mainshocks [11]. However, in the post-mainshock environment, buildings that have sustained structural damage are usually not repaired during the short period immediately following the mainshock when the rate of aftershocks is highest. As such, the accumulation of damage under successive aftershock events creates uncertainty in the state of the building when subsequent aftershocks occur. Past studies have used the Markov process [11, 78] to account for this uncertainty.

The life-cycle cost of a building is a function of the cost of new construction (C_0), the maintenance required to maintain its functionality (C_M) and the cost required to repair the damage (C_E) induced by a random number (N_E) of extreme events (earthquake, fire, flooding, …) as outlined in Equation 4.1 [86].

$$C_T = C_0 + C_M + \sum_{i=1}^{N_E} C_{E,i} \tag{4.1}$$

In this chapter, the primary focus is the economic loss caused by major mainshock events and subsequent aftershocks that occur within a specific time window. Section 4.2.1 addresses the earthquake-induced loss assessment problem in the post-mainshock environment. Evaluation of financial losses due to mainshock-aftershock ground motions in the pre-mainshock environment is discussed in Section 4.2.2.

4.2.1 Loss assessment in the post-mainshock environment

This section presents a framework for performing economic loss assessment in the post-mainshock environment where a mainshock has occurred and the building is exposed to subsequent aftershocks sequences. It is assumed that the building is in one of a predefined set of damage states, DS_i, immediately after the mainshock and can transition to a more severe state of damage when subjected to the ensuing aftershocks or conversely, be restored to the

pre-damaged state upon completion of any necessary repairs. The expected value of the aftershock-induced losses during the time window $[t_0, t_1]$ given the occurrence of damage state DS_i under the mainshock $\left(E^{[t_0,t_1]}[C_{AS}|DS_i]\right)$ can be obtained using Equation 4.2. The occurrence of the mainshock marks the origin of time when defining the time window $[t_0, t_1]$.

$$\begin{aligned} & E^{[t_0,t_1]}[C_{AS}|DS_i] \\ &= \sum_{p=1}^{\infty} P^{[t_0,t_1]}[N_{AS} \\ &= p]\left(\sum_{j=i+1}^{N_{DS}} P_{|N_{AS}}[DS_{ij}]E_{ij} + \sum_{k=1}^{N_{DS}-1} \sum_{j=i+1}^{N_{DS}} P_{|N_{AS}}[DS_{ik}]P_{|N_{AS}}[DS_{kj}]E_{ij} \right. \\ &\left. + \sum_{k=1}^{N_{DS}} \sum_{o=1}^{N_{DS}-1} \sum_{j=i+1}^{N_{DS}} P_{|N_{AS}}[DS_{ik}]P_{|N_{AS}}[DS_{ko}]P_{|N_{AS}}[DS_{oj}]E_{ij} + \cdots \right) \end{aligned} \tag{4.2}$$

N_{AS} is the number of aftershocks that is likely to occur and N_{DS} is the assumed number of possible states of building damage. The first summation on damage states accounts for the possibility that the building transitions directly (without intermediate state transitions) from state i after a mainshock to the more severe state j under aftershocks. The remaining summations account for the intermediate damage states that the structure can occupy starting from state i after a mainshock before finally residing in damage state j under aftershocks. Intermediate damage states refer to those that range from the onset of damage to just prior to most severe damage state. As described in further detail in Section 4.3.2, peak story drift ratios are used as the proxy for building-level damage, which ranges from 0 (intact state) to 5% (most severe damage state) at 0.5% increments. As such, the intermediate damage states in this chapter are all the damage states from 0.5% to 4.5% story drift ratio. Note that, except for the inner-most summation, the summations on damage states in Equation 4.2 always start from the lowest damage state (damage state 1) as the possibility of the structure being restored to its pre-damaged state is included in the relationship. The E_{ij} terms in Equation 4.2 represent the expected losses due to transition from damage state i to j under p events, which can be obtained from Equation 4.3.

$$E_{ij} = E\left[C_{ij}e^{-\alpha T_p} + \int_{t_0}^{T_p} C_{d_i} e^{-\alpha t} dt + \int_{T_p}^{t_1} C_{d_j} e^{-\alpha t} dt \,|DS_{ij}, N_{AS} = p \right] \tag{4.3}$$

C_{ij} is the loss associated with the building transitioning from damage state i to j, $e^{-\alpha T_p}$ is the term that discounts the monetary losses due to the *p-th* aftershock with a random arrival time T_p back to the initiation of the aftershock sequences with a discount factor α. C_{d_i} and C_{d_j} are the losses due to the disruption in the functionality of a building that is in damage state i after the mainshock during the time interval $[t_0, T_p]$ and moves to damage state j after an aftershock that occurs at the random arrival time T_p. $P_{|N_{AS}}[DS_{ij}]$ is the probability of transition from damage state i to j under p aftershocks. The probability of occurrence of p aftershocks in the time interval $[t_0, t_1]$ is equal to $P^{[t_0,t_1]}[N_{AS} = p]$. The damage state transition and disruption losses (C_{ij} and C_{d_i}) are functions of the initial and final states of building damage and independent of the number of aftershocks. Assuming the disruption losses are time-invariant and the disruption and transition losses are independent, the E_{ij} term can be obtained from Equation 4.4.

$$\begin{aligned} E_{ij} &= E\left[e^{-\alpha T_p}\left(C_{ij} - \frac{C_{d_i}}{\alpha}e^{-\alpha t_0} + \frac{C_{d_j}}{\alpha}e^{\alpha t_1}\right)|DS_{ij}, N_{AS} = p\right] \\ &= E[e^{-\alpha T_p}|N_{AS} = p]\left(E[C_{ij}] - \frac{e^{-\alpha t_0}}{\alpha}E[C_{d_i}] + \frac{e^{\alpha t_1}}{\alpha}E\left[C_{d_j}\right]\right) \end{aligned} \tag{4.4}$$

Equation 4.2 can be written in the matrix form shown in Equations 4.5 and 4.6.

$$\boldsymbol{E}^{[t_0,t_1]}[\boldsymbol{C_{AS}}] = \sum_{p=1}^{N_{AS}} \sum_{m} P^{[t_0,t_1]}[N_{AS} = p]\boldsymbol{P}^{\boldsymbol{m}}_{|\boldsymbol{N_{AS}}} \circ \boldsymbol{E} \tag{4.5}$$

$$\boldsymbol{P}^{\boldsymbol{m}}_{|\boldsymbol{N_{AS}}} = \sum_{l_1=1}^{p} \sum_{l_2>l_1}^{p} \dots \sum_{l_m>l_{m-1}}^{p} \prod_{r=1}^{m} \boldsymbol{P}_{|\boldsymbol{N_{AS}}} \tag{4.6}$$

$\boldsymbol{P}_{|\boldsymbol{N_{AS}}}$ is a matrix whose elements are the $P_{|N_{AS}}[DS_{ij}]$ terms in Equation 4.2, $\boldsymbol{E}$ is the matrix with the E_{ij} terms and $\circ$ is the symbol for the element-by-element multiplication of $\boldsymbol{P}^{\boldsymbol{m}}_{|\boldsymbol{N_{AS}}}$ and $\boldsymbol{E}$. $E^{[t_0,t_1]}[C_{AS}|DS_i]$ is the summation of the elements on row i of the $\boldsymbol{E}^{[t_0,t_1]}[\boldsymbol{C_{AS}}]$ matrix. $\boldsymbol{P}_{|\boldsymbol{N_{AS}}}$ is equivalent to the matrix often used to characterize the state-dependent transition probabilities in a Markovian stochastic system. For $j > i$, the damage state transition probabilities can be calculated using Equations 4.7 and 4.8.

$$P[DS_{ij}] = \sum_{l_m} P[DS_{ij}|N_{AS} = l_m]\left(\prod_{o=l_{m-1}}^{l_m-1}\left(1 - \sum_{w\neq i}^{N_{DS}} P[DS_{iw}|N_{AS} = o]\right)\right) \tag{4.7}$$

$$P\left[DS_{ij}|N_{AS}=l\right] = \int \left(P_{i,j}^{DS}\left[EDP > edp_j|IM, N_{AS}=l\right] - P_{i,j+1}^{DS}\left[EDP > edp_{j+1}|IM, N_{AS}=l\right]\right) f_{IM}(im)dim \quad (4.8)$$

$P_{i,j}^{DS}\left[EDP > edp_j|IM, N_{AS}=p\right]$ is the probability of transitioning to damage state j when the building is subjected to p aftershocks given that it is in damage state i after the first event in the sequence. The $P_{i,j}^{DS}\left[EDP > edp_j|IM, N_{AS}=p\right]$ term in Equation 4.8 can be calculated by subjecting the structure to p sequential aftershock ground motions in a back-to-back analysis under p records. Later in this section, we will show how the computational effort required to perform sequential response history analyses under p ground motions can be avoided without losing the essence of the proposed framework. f_{IM} is the probability density function (PDF) of the IM and is specific to the fault considered in the loss assessment. f_{IM} links the response of the building to the seismic hazard at the building's location and is a direct output from probabilistic seismic hazard analysis.

As discussed earlier, the probability of occurrence of aftershocks can be described by a nonhomogeneous Poisson distribution (Equation 4.9) with a rate (λ_{AS}) that characterizes both the temporal distribution of aftershock magnitudes as well as the temporal decay in their rate [55]. The rate of the Poisson distribution within the time interval t and $t + \Delta t$ can be obtained from Equation 4.10 [11]. The magnitudes of the aftershocks are bounded between M_0 and M_m where M_m is usually taken as the magnitude of the causative mainshock.

$$P^{[t_0,t_1]}[N_{AS}=p] = \frac{(\lambda_{AS}[t_0,t_1])^p}{p!} e^{-\lambda_{AS}[t_0,t_1]} \quad (4.9)$$

$$\lambda_{AS}[t_0,t_1] = \left(10^{a+b(M_m-M_0)} - 10^a\right)\frac{(t_1+c)^{1-\rho} - (t_0+c)^{1-\rho}}{1-\rho} \quad (4.10)$$

a and b in Equation 4.10 are constants that characterize the magnitude distribution and c and ρ are constants that define the temporal decay in the number of aftershocks. The rate of aftershocks defined in Equation 4.10 is used to calculate the $E[e^{-\alpha T_p}|N_{AS}=p]$ using Equation 4.11 [11, 86], which also incorporates the conditional PDF of the arrival time for a single aftershock given its occurrence in the time interval $[t_0, t_1]$, $f_{t|N_{AS}}$. The relationship that defines $f_{t|N_{AS}}$ is in the form of $f_{t|N_{AS}} = \frac{1-\rho}{(t_1-t_0+c)^{1-\rho}-(c)^{1-\rho}}(t+c)^{-\rho}$ (see Appendix A). The last integral of Equation 4.11 can be computed numerically.

$$E[e^{-\alpha T_p}|N_{AS}=p] = E\left[\sum_{o=1}^{p} e^{-\alpha T_o}\right] = \sum_{o=1}^{p} E[e^{-\alpha T_o}]$$

$$= \sum_{o=1}^{p}\left(\int_{t_0}^{t_1} \frac{1-\rho}{(t_1-t_0+c)^{1-\rho}-(c)^{1-\rho}}(t+c)^{-\rho}\, e^{-\alpha t} dt\right) \tag{4.11}$$

$$= p\,\frac{1-\rho}{(t_1-t_0+c)^{1-\rho}-(c)^{1-\rho}}\left(\int_{t_0}^{t_1} \frac{e^{-\alpha t}}{(t+c)^{\rho}}\, dt\right)$$

The proposed post-mainshock loss assessment framework accounts for the possibility that repair activities are completed during the time-window $[t_0, t_1]$ when aftershock sequences happen. In order for the repair activities to restore the building from damage state *j* to the pre-damaged state during the time interval $[t_0, t_1]$ where N_{AS} aftershocks are known to have occurred, the arrival times of two consecutive aftershocks should be greater than the repair time (τ_j). Assuming repair activities are Poisson random variables and that repairs could only restore the building to its pre-damaged state (there are no intermediate damage states due to incomplete repair), Equation 4.12 can be used to find the probability that the building is restored to its pre-damaged state during the time interval $[t_0, t_1]$.

$$P\left[DS_{j1}|N_{AS}=p\right]$$

$$= P\left[T_1 - t_0 > \tau_j\right] + \sum_{i=2}^{p-1} P\left[T_i - T_{i-1} > \tau_j\right] P\left[DS_j|N_{AS}=i\right] \tag{4.12}$$

$$+ P\left[t_1 - T_p > \tau_j\right] P\left[DS_j|N_{AS}=p\right]$$

If the repair activities are assumed to be Poisson random variables, for the first and last aftershocks, the probabilities $P\left[T_1 - t_0 > \tau_j\right]$ and $P\left[t_1 - T_p > \tau_j\right]$ can be calculated using the PDF of the arrival time given in Equation 4.28. For the remaining aftershocks, the distribution that defines the distance between the arrival times $\left(P\left[T_i - T_{i-1} > \tau_j\right]\right)$ is needed. While the conditional PDF of the arrival times of aftershocks given in Equation 4.28 can be directly used to derive $P\left[T_i - T_{i-1} > \tau_j\right]$, the complexity of the calculations can be significantly reduced with a change of variable t in Equation 4.28 such that the new conditional PDF of the arrival times will take on a standard uniform distribution in the transformed time space [11] (see Appendix B for the relationship between the two time spaces). In the new time space, the distance between the arrival times would have a triangular distribution with the PDF shown in 12 where z is defined as $z = T_i - T_{i-1}$. t_0^* and t_1^* are the lower and upper limits of the time interval $[t_0, t_1]$ in the new time space and can be calculated using Equation 4.2.

$$f_Z(z) = \begin{cases} -z, & t_0^* - t_1^* \le z \le 0 \\ z, & 0 < z \le t_1^* - t_0^* \end{cases} \tag{4.13}$$

$P\left[DS_j | N_{AS} = i\right]$ in Equation 4.12 is the probability that the building would remain in damage state j given the occurrence of i aftershocks and can be calculated as shown in Equation 4.14.

$$\begin{aligned} & P\left[DS_j | N_{AS} = i\right] = P\left[edp_{j-1} < EDP < edp_{j+1} | N_{AS} = i\right] \\ & = P\left[EDP < edp_{j+1} | N_{AS} = i\right] - P\left[EDP > edp_{j-1} | N_{AS} = i\right] \\ & = 1 - P\left[EDP > edp_{j+1} | N_{AS} = i\right] - P\left[EDP > edp_{j-1} | N_{AS} = i\right] \\ & = 1 \\ & - \int \left(P\left[EDP > edp_{j+1} | IM, N_{AS} = i\right]\right. \\ & \left. + P\left[EDP > edp_{j-1} | IM, N_{AS} = i\right]\right) f_{IM}(im) dim \end{aligned} \tag{4.14}$$

Equations 4.2 through 4.14 form the backbone of the methodology for loss analysis under sequential seismic events. However, the computational effort associated with performing sequential nonlinear dynamic analyses to compute the $P_{i,j}^{DS}\left[EDP > edp_j | IM, N_{AS} = p\right]$ term in Equation 4.8 can be significantly reduced by breaking the time window of the aftershock sequence into small steps such that no more than one aftershock is likely during each interval. If the time intervals are selected to be small enough compared to the period over which the discount factor is defined, then Equation 4.2 can be written as follows.

$$\boldsymbol{E^{t_m}[C_{AS}]} = \boldsymbol{P^m} \circ (\boldsymbol{E_C} + \boldsymbol{E_D}) + \boldsymbol{E_D^{t_{m-1}}} \tag{4.15}$$

$$\boldsymbol{P^m} = \prod_{r=1}^{m} \boldsymbol{P(t_{r-1}, t_r)} \tag{4.16}$$

$\boldsymbol{E^{t_m}[C_{AS}]}$ is the matrix with the total expected cumulative aftershock-induced losses in time step m after the occurrence of the mainshock, which are due to the damage state transitions that can happen in the time interval $[0, t_m]$. $\boldsymbol{E_C}$ is the matrix with the expected losses due to building structural and non-structural damage and $\boldsymbol{E_D}$ is the matrix that contains the expected losses due to the disruption in the normal functionality of the building. Similar to Equation 4.5, $\boldsymbol{E^{t_m}[C_{AS}|DS_i]}$ is the sum of the losses on row i of $\boldsymbol{E^{t_m}[C_{AS}]}$**.** Note the addition of $\boldsymbol{E_D^{t_{m-1}}}$, the disruption losses in the previous step, to the total aftershock-only losses at each subsequent step. The presence of $\boldsymbol{E_D^{t_{m-1}}}$ in Equation 4.15 accounts for the fact that the disruption losses accumulate as the building progresses through the time intervals. The accumulation of losses caused by building damage, (E_c), is reflected in the $\boldsymbol{P^m}$ matrix.

The elements of the $\boldsymbol{E_C + E_D}$ matrix at each step can be calculated as $E_{ij} = e^{-\alpha T_m} E\left[C_{ij} + C_{d_j}\right]$.

For the first time interval after the mainshock, $\boldsymbol{E^{t_m}[C_{AS}]}$ yields the expected losses given the first transition from the immediate post-mainshock damage state to the damage state following the first aftershock, whereas, in the subsequent intervals $\boldsymbol{E^{t_m}[C_{AS}]}$ gives the expected losses due to damage state transitions under successive aftershocks. The elements of $\boldsymbol{P^m}$ are the cumulative probabilities of damage state transition at time step m after the occurrence of the mainshock. To calculate the $\boldsymbol{P(t_{r-1}, t_r)}$ matrix in Equation 4.16, damaged state transition probabilities are needed. Similar to Equation 4.5, the damage state transition probabilities are represented by a Markov transition matrix. Each element P_{ij} of the Markov transition matrix in Equation 4.17 is the probability of transitioning from damage state i sustained in the time interval $[t_{i-2}, t_{i-1}]$, to damage state j in the successive interval $[t_{i-1}, t_i]$.

$$\boldsymbol{P(t_{r-1}, t_r)} = \begin{bmatrix} P_{11}(t_{r-1}, t_r) & P_{12}(t_{r-1}, t_r) & \cdots & P_{1l}(t_{r-1}, t_r) \\ P_{21}(t_{r-1}, t_r) & P_{22}(t_{r-1}, t_r) & \cdots & P_{2l}(t_{r-1}, t_r) \\ \vdots & \vdots & \ddots & \vdots \\ P_{l1}(t_{r-1}, t_r) & 0 & \cdots & P_{ll}(t_{r-1}, t_r) \end{bmatrix} \tag{4.17}$$

Damage states become incrementally more severe as the index of the transition probabilities increases. On the other hand, the completion of repair activities returns the building to the pre-damaged state with a probability P_{j1} where j is the damage state before the initiation of repairs. P_{ij} $j > i$ in Equation 4.17 can be calculated through Equation 4.18 where $\lambda_{IM}^{t_{r-1}, t_r}$ is the mean rate of exceedance of the IM in the time window of $[t_{r-1}, t_r]$ obtained using APSHA.

$$\begin{aligned} P_{ij}(t_{r-1}, t_r) = \mu_{AS}(t_{r-1}, t_r) \int \left(P_{i,j}^{DS}\left[EDP > edp_j | IM\right]\right. \\ \left. - P_{i,j+1}^{DS}\left[EDP > edp_{j+1} | IM\right]\right) df_{IM}(im) \end{aligned} \tag{4.18}$$

4.2.2 Losses in the pre-mainshock environment

This section focuses on seismic loss assessment in the pre-mainshock environment, where the uncertainty in the occurrence of the mainshock and the ensuing damage state

transitions are incorporated. The first step in the pre-mainshock loss is to formulate a relationship for losses under mainshock events.

$$E_i[C_{MS}] = \sum_{n=1}^{N_S} \sum_{p=1}^{N_{MS}} E[C_{1i} e^{-\alpha T_p} | N_{MS} = p] P[DS_{1i}] \tag{4.19}$$

In Equation 4.19, $E_i[C_{MS}]$ is the expected losses associated with damage state i. The first summation is over all N_S sources that contribute to the seismic hazard at the location of the building. N_{MS} is the random number of mainshocks during the period over which mainshock-induced losses are being evaluated (usually lifetime of the building). $P[DS_{1i}^n]$ is the probability of transition from the pre-damaged state to damage state i due to the probable mainshock events on source n. Note that the damage state transitions always happen from the pre-damaged state to a more severe damage state as the building is always assumed to be pre-damaged when a mainshock occurs. This assumption is based on the long return periods of major mainshocks, which would allow the structure to be restored to its pre-damaged state [11]. The total expected losses due to mainshocks can be obtained by multiplying the expected number of mainshocks ($E[N_{MS}]$) by the ensuing expected losses ($E[C_{1i} e^{-\alpha T_p} | N_{MS} = p] P[DS_{1i}^n]$) as described in Equation 4.20 [97].

$$E_i[C_{MS}] = \sum_{n=1}^{N_S} E[N_{MS}]\, E[C_{1i} e^{-\alpha T_p} | N_{MS} = p] P[DS_{1i}^n] \tag{4.20}$$

Given that mainshocks are usually modeled as a homogeneous Poisson process, the expected number of mainshocks during the building's lifetime (T_L) can be computed as $E[N_{MS}] = \lambda_n T_L$ where λ_n is the rate of mainshocks on source n. The arrival time of mainshocks follow a uniform distribution given $N_{MS} = n$ [97]. Again, assuming C_{1j} is independent of the arrival times and number of mainshocks, the discounted expected losses is computed as follows [11, 86].

$$\begin{aligned} E[e^{-\alpha T_p} | N_{MS} = n] &= E\left[\sum_{o=1}^{n} e^{-\alpha T_o}\right] = \sum_{o=1}^{n} E[e^{-\alpha T_o}] = \sum_{o=1}^{n} \left(\int_0^{T_L} \frac{1}{T_L} e^{-\alpha u} du \right) \\ &= \frac{n}{\alpha T_L} (1 - e^{-\alpha T_L}) \end{aligned} \tag{4.21}$$

Consequently, the expected mainshock-induced life-cycle losses can be computed using Equation 4.22.

$$E_i[C_{MS}] = \sum_{n=1}^{N_S} \frac{\lambda_n(1 - e^{-\alpha T_L})}{\alpha} E[C_{1i}] P[DS_{1i}^n] \tag{4.22}$$

$P[DS_{1i}^n]$ can be calculated using a relationship similar to the one shown in Equation 4.8 after subjecting the building to the mainshock ground motions such that they would induce a target damage level in the building ($P_{MS}^{DS}[EDP > edp_i|IM] - P_{MS}^{DS}[EDP > edp_{i+1}|IM]$ in Equation 4.23).

$$P[DS_{1i}^n] = \int (P_{MS}^{DS}[EDP > edp_i|IM] - P_{MS}^{DS}[EDP > edp_{i+1}|IM]) df_{IM}^n(im) \tag{4.23}$$

Finally, Equation 4.24 can be used to combine the total discounted losses due to probable mainshocks and aftershocks during the service life of the building. $E[C_{AS}|DS_i]$ is the expected losses induced by aftershocks that would follow each probable mainshock and can be calculated using the procedure described in Section 4.2.1.

$$E_i[T_L] = \sum_{n=1}^{N_S} \frac{\lambda_n(1 - e^{-\alpha T_L})}{\alpha} P[DS_{1i}^n](E[C_{1i}] + E[C_{AS}|DS_i]) \tag{4.24}$$

4.3 Application of Mainshock-Aftershock Loss Assessment Methodology

The loss assessment methodology described in Section 4.2 is applied to a 4-story special RC moment-resisting frame building. The building is designed following the provisions of ACI 318-02 and ASCE 7-05 [98, 99] and modeled in the *OpenSees* platform as part of the study by Haselton [46] (Fig. 2-4). $P - \Delta$ effects are incorporated with a leaning column. Beams and columns are modeled using flexural plastic hinges at the member-ends with a trilinear backbone curve developed by Ibarra et al. [50]. The first-mode period of the numerical model is 1.12s. More detailed information on the design and structural modeling approach can be found in Haselton [46].

Assuming a construction cost per square foot of 237 dollars based on the estimate provided by the Seismic Performance Prediction Program (SP3) [100], the total construction cost of the building is 9,480,000 dollars. The replacement cost is assumed to be 25% greater than the initial construction cost to account for the cost of demolishing the collapsed or irreparable building and removing debris from the site; both of which are necessary steps before the reconstruction begins [101]. All losses reported in later sections are normalized with respect to the building's replacement cost to offset the impact of errors in the cost estimation on the loss evaluation [88]. A list of the damageable structural and nonstructural

components is summarized in Table 4-1. This information is used as the input for SP3 to evaluate the earthquake-induced losses at different building damage states under mainshock and aftershock ground motions.

Table 4-1 Damageable components (adopted from [100])

Component Category	Building Component	Unit	EDP	Quantity per story
Structural	Special moment frame concrete beams and columns	Each	SDR[a]	16
	RC slab column connection	Each	SDR	25
Exterior cladding	Curtain walls	30 ft^2	SDR	87
Partition walls	Partition walls	100 ft	SDR	10
Interior finishes	Wall partition finishes	100 ft	SDR	0.8
	Suspended ceiling	250 ft^2	PFA[b]	15
	Independent pendant lighting	Each	PFA	15
Plumbing and HVAC	Potable water piping	1000 ft	PFA	1.7
	Potable water pipe bracing	1000 ft	PFA	1.7
	HVAC ducting	1000 ft	PFA	1.0
Other nonstructural	Fire sprinkler water piping	1000 ft	PFA	2.0
	Traction elevator	Each	PFA	3[c]
	Fire sprinkler drop	$\times 100$	PFA	0.9

[a] Story drift ratio

[b] Peak floor acceleration

[c] Entire building

Nonlinear dynamic analyses are performed on the numerical models using a set of 25 record-pairs. Each pair consists of an as-recorded mainshock-aftershock ground motion sequence. The classification of the second ground motions in the record-pairs as aftershocks is done using the time and distance windowing algorithms developed by Knopoff and Gardner [84] and Wooddell and Abrahamson [8]. The ground motion pairs are from the Class 1 (mainshock) and Class 2 (aftershock) records of the Northridge, Livermore, Coalinga, Landers, Mammoth Lakes 01, Whittier Narrows, Darfield and Chi-Chi earthquakes, which are available in the PEER-NGA West2 database [102]. A magnitude-dependent time window and a distance threshold of 40 km measured in terms of the centroidal Joyner-Boore distance [8] is used to identify the aftershock ground motions following a mainshock event. The magnitudes of the events that produced the selected ground motions range from 5.8 and 7.6 for mainshocks and 5.2 and 6.5 for aftershocks. Pulse-like ground motions are excluded from

the set of 25 record-pairs. The response spectra of the mainshock and aftershock ground motions are shown in Fig. 4-1.

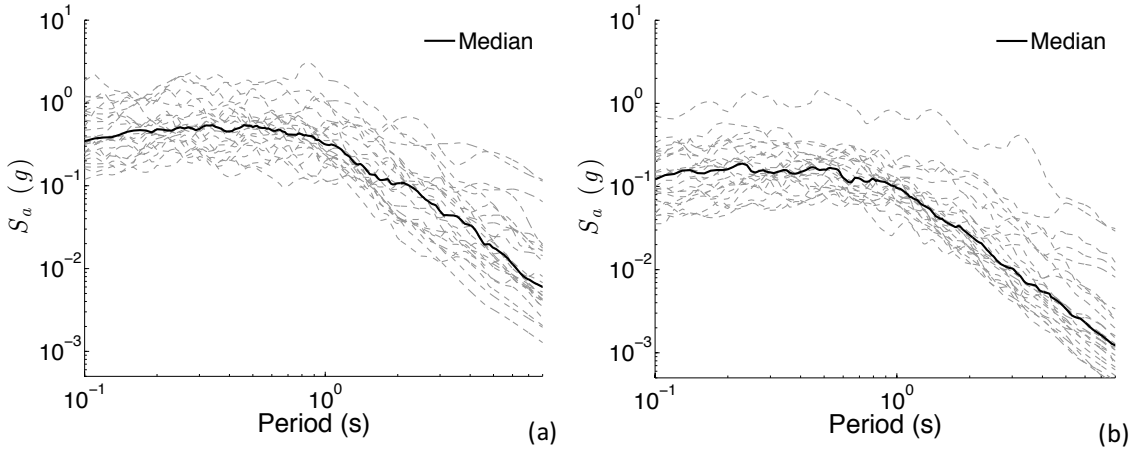

Fig. 4-1. Response spectra of a) mainshock and b) aftershock ground motions

4.3.1 Seismic hazard analysis

Conventional PSHA [82] and APSHA [11] are used to quantify seismic hazard due to the occurrence of mainshocks and aftershocks, respectively. The seismic hazard analyses are performed for the high seismicity site in Southern California used to design the building [46]. The adopted PSHA and APSHA approach uses source and magnitude models that, while simpler relative to the USGS models, account for all the sources that contribute to the seismic hazard at the location of the building as well as the characteristic magnitude that each source can generate. The parameters that define the spatial distribution of earthquake magnitudes and the temporal decline in the rate of aftershocks are based on the generic California model by Reasenberg and Jones [55]. The Boore and Atkinson [56] ground motion prediction equation is used to estimate the median and standard deviation of the lognormal distribution of the IM for each magnitude and distance. The magnitude of the largest aftershock is assumed to be equal to that of the largest mainshock. Note that this assumption is adopted on the basis of prior studies [11, 55] and is expected to influence the results of the loss assessment. For example, lower aftershock-induced losses will likely be obtained if the upper limit on the magnitude of the aftershock is not set to match that of the mainshock. The minimum magnitude is taken as 5 since events with smaller magnitudes are not expected to induce notable damage in code-conforming structures.

Fig. 4-2 shows the hazard curves developed for the site of interest based on $S_a(T_1)$, where T_1 is the first mode period of the pre-damaged 4-story moment frame structure. The mainshock hazard curve is developed using conventional PSHA and accounts for the

contribution of all significant faults to the total seismic hazard at the site. On the other hand, the aftershock hazard, which was developed using APSHA, only considers the fault that contributes the most to the seismic hazard at the location of the building. Recall that APSHA is for seismic hazard analysis in the post-mainshock environment where a mainshock has occurred and the seismic hazard due to the following aftershocks is being calculated. Since it is very unlikely for simultaneous ruptures to happen on multiple faults that participate in the seismic hazard at the site, the single fault that dominates the mainshock hazard is used in APSHA. Deaggregation of the site seismic hazard, which was performed using the tool provided by the United States Geological Survey (USGS) [52], shows that the Los Angeles section of the Puente Hills fault is the main source of seismic hazard. Therefore, the APSHA hazard curve presented in Fig. 4-2 is obtained solely for the Los Angeles section of the Puente Hills fault system. The APSHA hazard curve is developed for a time window of one year starting immediately after the occurrence of the mainshock. A quick comparison between PSHA and APSHA hazard curves in Fig. 4-2 reveals substantially higher seismic hazard in the post-mainshock environment compared to the mainshock-only seismic hazard.

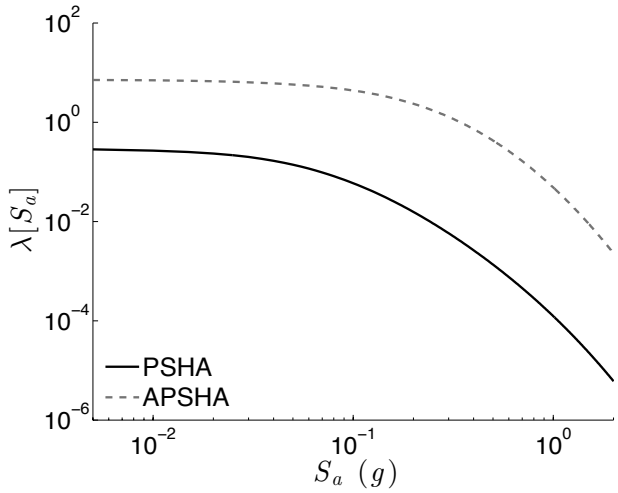

Fig. 4-2. Mainshock and mainshock-aftershock seismic hazard curves for $\boldsymbol{T = 1.12s}$

4.3.2 Nonlinear dynamic analysis

Nonlinear dynamic analyses are performed using sequential ground motions to generate the data needed to compute the building damage state transition probabilities. The nonlinear structural model is subjected to both ground motions in each record-pair such that under each ground motion in the pair, the building experiences a predefined maximum SDR. Ten incrementally-increasing SDR levels, ranging from 0.5% to 5% maximum SDR with increments of 0.5% [14], as well as the pre-damaged state are targeted. These SDR values serve as proxies for the possible states of structural and non-structural damage that the

building can sustain under a seismic event. The outputs of the nonlinear dynamic analysis yield the numerical values of the $P_{i,j}^{DS}$ terms in Equations 4.18 and 4.23. These terms will ultimately be used to populate the elements of the Markov transition matrix (Equation 4.17) and perform the pre-mainshock loss assessment (Equation 4.24). The first step in obtaining damage state transition probabilities involves subjecting the structure to the mainshock ground motions and calculating the P_{MS}^{DS} values required as input to Equation 4.23, by fitting a lognormal distribution to the ground motion spectral accelerations associated with each of the damage states [59]. The parameters that define the lognormal distributions are obtained using stripe analysis and the method discussed in Baker [61]. The maximum SDR and PFA profiles obtained for each of the ten SDR limit states are used as the inputs for SP3 to calculate the earthquake-induced losses. Next, nonlinear response history analysis is performed on the mainshock-damaged structure using the second ground motion in the record-pairs, to obtain the post-mainshock capacity corresponding to the maximum SDR values from the previous step. The mainshock ground motions are scaled incrementally to each of the ten SDR levels and stripe analysis [61] is used to obtain the aftershock damage state fragility curves for each of the mainshock states. Fig. 4-3 shows the aftershock building damage fragility curves obtained when the 4-story building sustains different levels of damage under the mainshock ground motions. Expectedly, the reduction in the building capacity when it is subjected to the mainshock ground motions is reflected in the increased likelihood of damage state transition under the aftershocks.

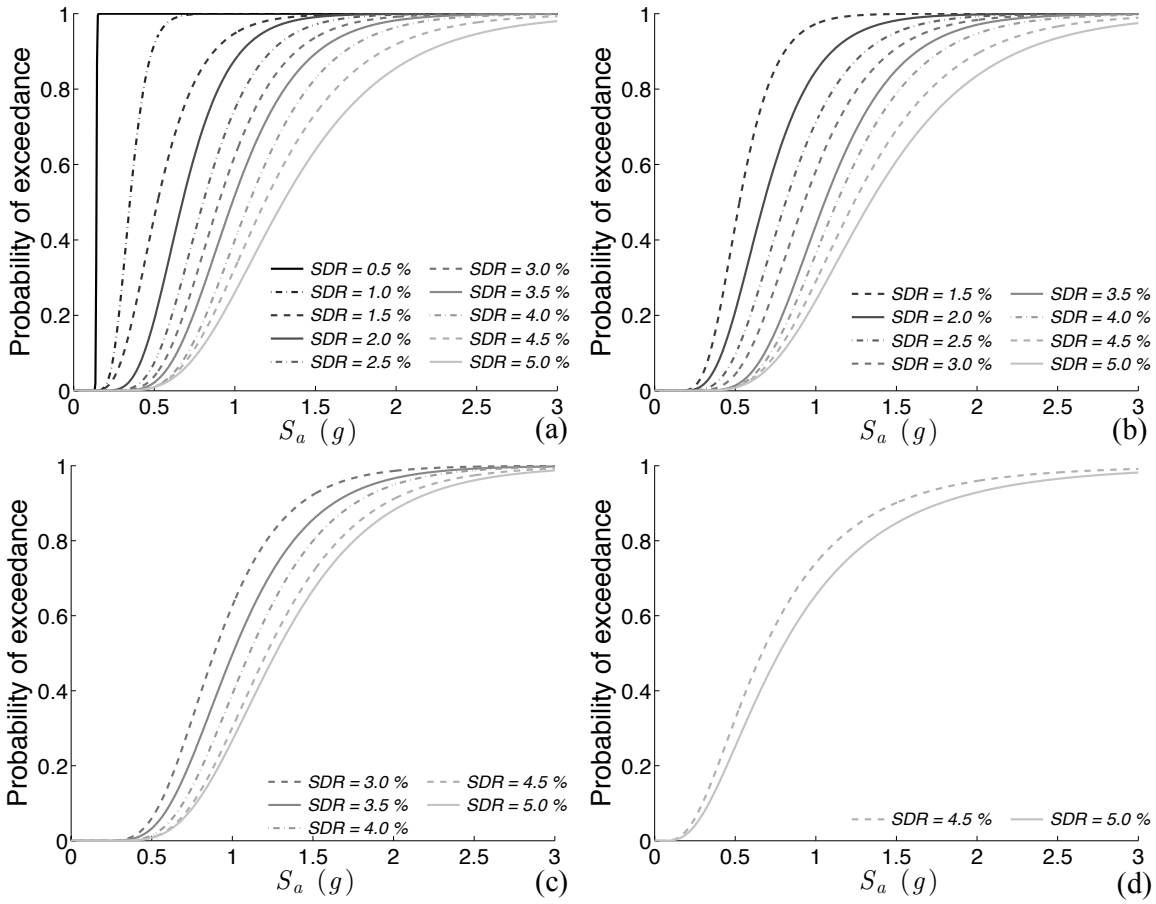

Fig. 4-3. Aftershock building damage fragility curves for a) pre-damaged, b) $\boldsymbol{SDR = 1\%}$, c) $\boldsymbol{SDR = 2.5\%}$ and d) $\boldsymbol{SDR = 4\%}$ states under the mainshock ground motions

The expected repair cost and time needed to restore the building to the pre-damaged state after experiencing each of the 10 mainshock-induced damage states is shown in Fig. 4-4a, i.e. damage caused by first ground motion in a sequence. Under successive ground motions, the expected differential losses associated with transition from damage state i to a more severe damage state j is taken as the difference in the losses associated with the two damage states, i.e., $E_{ij} = E_j - E_i$. Again, assuming exponentially distributed repair times and that repair activities can only restore the building to the pre-damaged state (there are no intermediate damage states due to incomplete repair), the elements of the Markov transition matrix in Equation 4.17 can be obtained from the inverse of the expected repair times shown in Fig. 4-4a [59]. Fig. 4-4b shows a disaggregation of the total expected losses based on the component groups listed in Table 4-1 conditioned on the each of the ten building-level damage states. The contribution of the collapse state is also included in the values shown in Fig. 4-4a. Collapse is assumed to have happened if the maximum SDR obtained from the response history analyses exceeds 10%.

The losses due to building disruption are also included in the lifecycle cost analysis. Such losses are divided into two parts [103]; the losses due to shifting and transferring which is taken as 0.95 \$/ft^2 [103] and the losses due to loss of rental income taken as 1.36 \$/ft^2 per month [103]. The rental income loss is only applied to the damage states beyond $SDR = 2\%$ as temporary relocation of tenants is unlikely to occur at the lower damage states. All losses are adjusted for inflation as the values suggested by Hazus [103] are estimates for year 1994.

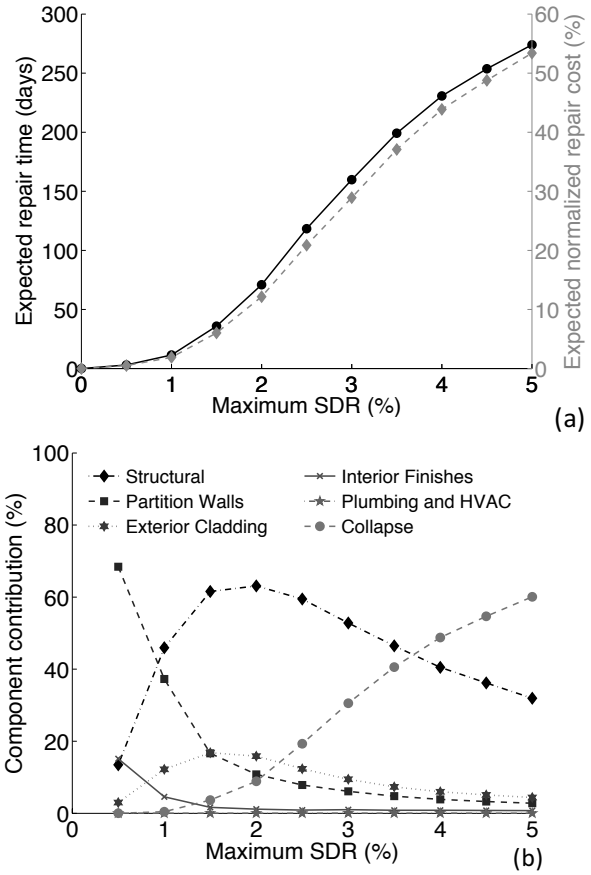

Fig. 4-4. a) Expected repair cost and repair time for different damage states under mainshock ground motions and b) Contribution of structural and non-structural components as well as the collapse state to the total mainshock-only losses for different damage states

4.3.3 Time-dependent seismic-induced loss analysis

4.3.3.1 Loss analysis in the post-mainshock environment

First, lifecycle loss analysis in the post-mainshock environment is performed where a mainshock event has occurred and the building is exposed to subsequent aftershocks. The values presented in this section are the additional losses that are likely to occur due to aftershocks and do not include the losses under the mainshock event that precedes the aftershocks. The discussion on the aftershock-only losses that are the main focus of this section could serve to inform stakeholders on the additional losses that they are likely to incur

due to aftershocks and help to better plan for the funding that will needed to support the recovery process.

Again, since it is highly unlikely for simultaneous ruptures to happen on multiple sources that contribute to the seismic hazard at the location of the building, only the Puente Hills fault, which has the highest contribution to the mainshock hazard, is used for the post-mainshock loss assessments. Aftershocks hazard is considered for a period of 30 days after the mainshock as the exponential rate of decay means that aftershock seismic hazard would be negligible after this time window. A time increment of 0.01 day is used since the occurrence of more than one aftershock on the contributing fault is unlikely during such a small time window. Table 4-2 lists the limit state transition probabilities at the end of the 30-day period considered in the aftershock loss assessment. The transition probabilities are presented for various cases where the building has experienced a certain level of mainshock-damage and progresses towards higher states of damage under the aftershocks. The possibility of the restoring the building to its pre-damaged state is not included in the probabilities summarized in Table 4-2.

Table 4-2. Limit state transition probabilities under aftershocks at the end of the 30-day period

Limit state		Intact	Probability of transition $SDR =$									
			0.5%	1.0%	1.5%	2.0%	2.5%	3.0%	3.5%	4.0%	4.5%	5.0%
Intact		0.335	0.265	0.136	0.089	0.050	0.029	0.018	0.014	0.009	0.007	0.048
$SDR =$	0.5%	0	0	0	0	0	0	0	0	0	0	0
			0.602	0.136	0.081	0.052	0.033	0.019	0.010	0.012	0.007	0.048
	1.0%	1		0	0	0	0	0	0	0	0	0
				0.746	0.078	0.050	0.032	0.025	0.010	0.009	0.006	0.045
	1.5%	1			0	0	0	0	0	0	0	0
					0.834	0.046	0.036	0.017	0.010	0.010	0.005	0.041
	2.0%	2				0	0	0	0	0	0	0
						0.873	0.037	0.020	0.012	0.010	0.005	0.043
	2.5%	2					0	0	0	0	0	0
							0.895	0.023	0.017	0.012	0.004	0.049

3.0%		0.893	0.024	0.021	0.008	0.054
3.5%			0.809	0.032	0.015	0.145
4.0%				0.781	0.034	0.185
4.5%					0.706	0.294
5.0%						1.000

Fig. 4-5 shows the normalized expected aftershock-only losses as a function of the time elapsed since the occurrence of mainshock, which include losses due to structural- and non-structural damage as well as disruption losses. The contribution of disruption losses ranges from 9% to 55% of the total losses and increases with the mainshock-SDR level and the time elapsed since the occurrence of the mainshock (Fig. 4-6). The increase in the contribution of disruption losses with the mainshock-SDR level is mainly due to the reduction in the building component damage incremental losses as the mainshock-SDRs increase. The increase in the contribution of disruption losses with the time elapsed since the occurrence of the mainshock can be explained by the fact that the contribution from building component damage becomes less significant as the increments in limit state transition probabilities get smaller with time. Note that the contribution of disruption losses can increase without bounds if the possibility of repair is not included in the Markov transition matrices, which can lead to unrealistic results if the assumed duration of aftershock sequences is too long [11]. The losses shown in Fig. 4-5**a** are calculated assuming no repairs during the 30-day period considered for aftershock sequences. In contrast, Fig. 4-5b shows the aftershock-only losses when the initiation of repairs during the 30-day time window is considered assuming exponentially distributed repair times. All losses in Fig. 4-5 are conditioned on the immediate post-mainshock damage state. For common small discount factors, the impact of discounting the aftershock-only losses for the 30-day period is insignificant. Nevertheless, a discount rate of 3% is used to calculate the expected losses at the beginning of the aftershock sequences. The time-dependent loss curves in Fig. 4-5a are marked with a sharp increase within the first few days when the rate of occurrence of aftershocks is highest. For the lowest immediate post-mainshock SDR levels, more than 2/3 of the expected losses occurs in the first three days

following the mainshock. At the end of the 30-day period, the aftershock-only losses could be as high as 7% of the building's replacement cost if the building remains pre-damaged under the mainshock. The aftershock-only losses associated with the higher immediate post-mainshock SDR levels continue to grow at a higher rate (albeit slower compared to the initial days after the mainshock), mostly because of the higher contribution of disruption losses.

The aftershock-only losses are functions of both immediate post-mainshock damage state and the probable transition to more severe damaged states under a sequence of aftershocks. These losses are generally found to decrease as the severity of the post-mainshock damage state increases. The highest aftershock-only losses occur when the building is pre-damaged following the mainshock. This is not surprising given that there are more damage states that the building can occupy under aftershocks when transition starts from a lower mainshock-SDR level. For example, a building that is undamaged immediately following the mainshock can transition through ten states of damage ($SDR = 0.5\% - 5\%$) under aftershocks. For other mainshock-SDR cases, while the differential losses (difference in losses between two damage states) due to transition to more severe states under aftershocks are smaller compared to the mainshock-pre-damaged case, the building is more likely to experience the more severe damage states when subjected to aftershocks. For example, the transition probabilities listed in Table 4-2 suggest that a mainshock-SDR of 3.5% increases the likelihood of the $SDR = 5.0\%$ state at the end of 30 days of aftershocks by a factor of 3 compared to when the mainshock-SDR is 2.5%. The higher probabilities of transition to the more severe damage states under aftershock once the building experiences higher mainshock-SDRs offsets the lower differential losses. As such, it is not surprising that the aftershock-only losses associated with the immediate post-mainshock damage state of $SDR = 3.5\%$ in Fig. 4-5 are higher than the case where the building is in the $SDR = 2.5\%$ or $SDR = 3.0\%$ states following the mainshock.

The trends in Fig. 4-5b suggest that the initiation of repair activities would have little impact on the aftershock-only losses within the first few days where successive aftershocks are more likely to happen. As expected, incorporating the possibility of the building being restored to the pre-damaged state most significantly influences the losses due to the lower damage states whose repair measures require the lowest time for completion. As an example, the losses associated with the pre-damaged state will be approximately 25% lower if repair is included in the loss evaluation whereas the reduction in the losses associated with the $SDR = 4.5\%$ state is approximately 5% under a similar scenario.

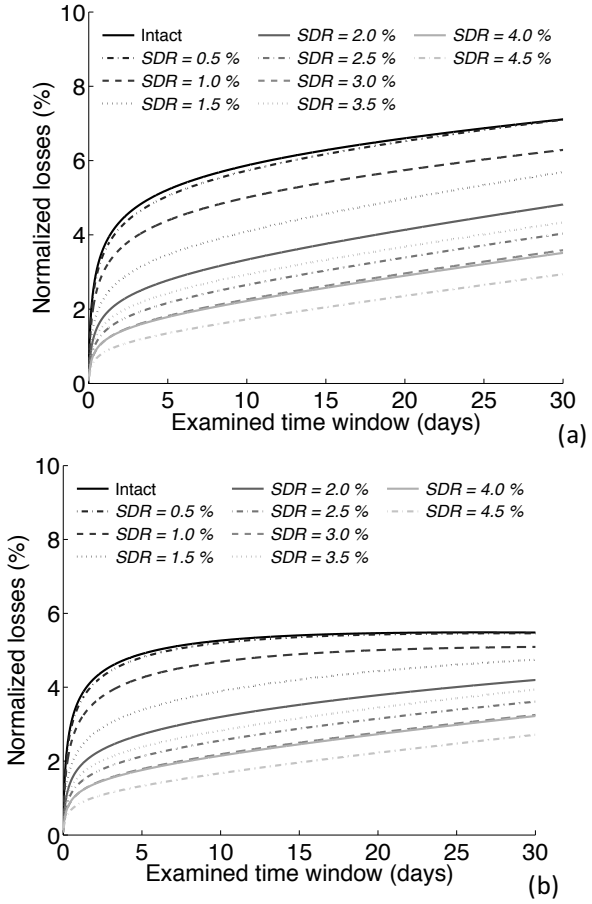

Fig. 4-5. Normalized expected aftershock-only losses as a function of time elapsed since mainshock for a) without repair and b) exponential repairs scenarios

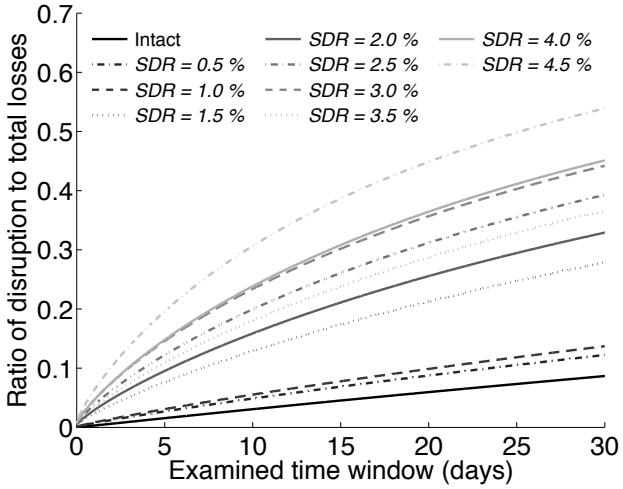

Fig. 4-6. Time-dependent contribution of disruption losses to the total aftershock-only losses

Fig. 4-7 shows the contribution of each aftershock damage state to the only-aftershock losses, which is conditioned on the immediate post-mainshock SDR level. Transition to the $SDR = 5\%$ state constitutes most of the aftershock-only losses for all immediate-post-mainshock damage states. Whereas the transition probabilities to the lower damage states

under aftershocks are higher (Table 4-2), the lower differential losses results in a lower contributions to the aftershock-only losses compared to the $SDR = 5\%$ state. The contribution of the $SDR = 5\%$ state in the total only-aftershock losses increases as the immediate post-mainshock SDR increases. This is expected given the increase in the probability of transition to $SDR = 5\%$ under aftershocks (Table 4-2) and the decrease in the number of the intermediate damage states that the building can occupy as the immediate post-mainshock SDR increases.

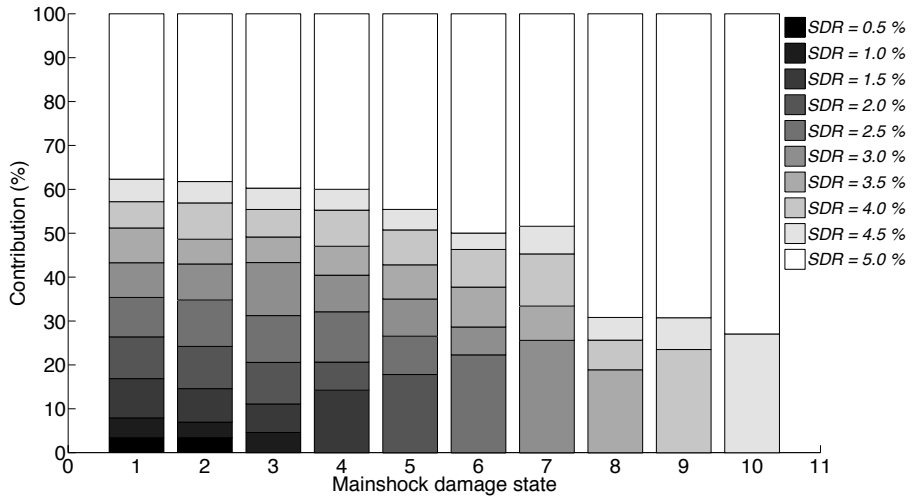

Fig. 4-7. Contribution of each aftershock damage state to the aftershock-only losses conditioned on the immediate post-mainshock limit state

A breakdown of the contribution of each component groups listed in Table 4-1 as well as the collapse state to the aftershock-only losses (disruption losses excluded), which are conditioned on the immediate post-mainshock damage state (ranging from pre-damaged to $SDR = 4.5\%$), is shown in Fig. 4-8. Comparing the trends in Fig. 4-8 to the observations from Fig. 4-4b, the collapse state has a more significant presence in the aftershock-only losses. As shown in Fig. 4-4b, up to an immediate post-mainshock SDR of 3.5%, non-collapse mainshock-only losses exceed that of collapse. In contrast, Fig. 4-8 shows that aftershock-only losses due to collapse exceed that of non-collapse starting at a much lower SDR of 1.5%. Given the significant share of the $SDR = 5\%$ state in the only-aftershock losses observed in Fig. 4-7 and the greater contribution of the collapse state to the total losses (Fig. 4-4b), it is not surprising that collapse plays a major role in the aftershock-only losses.

Among the building components, structural damage constitutes the largest non-collapse losses. Non-structural components make a relatively small contribution to the only-aftershock losses as they are more likely to get damaged under the mainshock even if the immediate post-mainshock SDR is low.

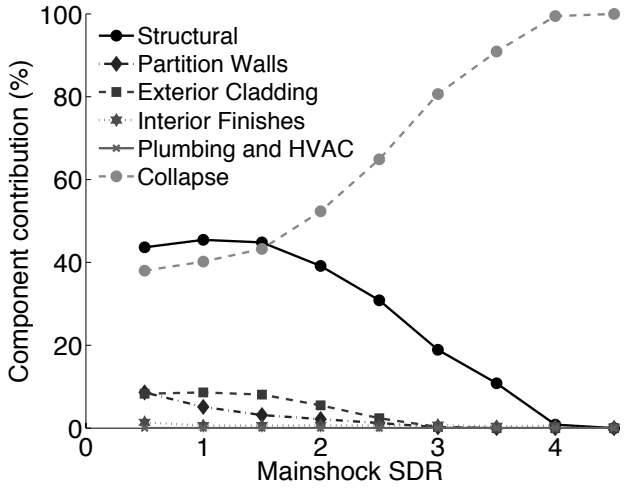

Fig. 4-8. Contributions of structural and nonstructural components as well as the collapse state to the aftershock-only losses associated conditioned on the immediate post-mainshock limit state

4.3.4 Loss assessment in the pre-mainshock environment

The main objective of this section is to evaluate the seismic-induced losses during an assumed building service life of 50 years accounting for all the possible sequences of mainshock and aftershock ground motions that can occur during this period (mainshock-aftershock losses). All faults that can generate at least one sequence of mainshock and aftershock ground motions during the 50-year time window are considered. Again, the contribution of aftershocks is considered for a period of 30 days after the mainshock and the present value of losses over the life span of the building is calculated using a discount factor of 3%. Table 4-3 shows that the mean annual frequency of exceeding each damage state is 100% to 300% higher for mainshocks and aftershocks compared to when only the former is considered.

Table 4-3. Mean annual frequency of exceedance of limit states for the mainshock-only and mainshock-aftershock scenarios

Scenario	Transition probability ($\times 10^{-3}$)									
	$SDR =$									
	0.5%	1.0%	1.5%	2.0%	2.5%	3.0%	3.5%	4.0%	4.5%	5.0%
Mainshock-only	25.97	3.56	0.70	0.44	0.23	0.05	0.03	0.02	0.03	0.15
Mainshock-aftershock	53.59	7.53	2.78	1.10	0.53	0.19	0.11	0.08	0.06	0.35

The expected normalized present value of mainshock-aftershock and mainshock-only losses for the service life of the building are presented in Fig. 4-9. The lifecycle mainshock-only losses are calculated by setting the losses associated with aftershocks to zero in Equation 4.24 and accounting for the disruption losses for a period of 30 days after each mainshock. For both scenarios, the values shown in Fig. 4-9 are the sum of the losses over the ten SDR limit states. Under the mainshock-aftershock scenario, the probable losses associated with all 10 SDR levels are considered for both the mainshock and aftershock. The losses due to all the likely mainshock-aftershock sequences is approximately 70% of the replacement cost of the building at the end of the building's service life. Under the mainshock-only scenario, the losses during the same period will be about 55% of the replacement cost, suggesting that the consideration of aftershock hazard could increase the lifecycle losses by approximately 30%.

Table 4-4 shows the contribution of different structural and non-structural components as well as the collapse state to the mainshock-aftershock and mainshock-only service life losses. Under the mainshock-only scenario, partition walls and structural elements rank first and second, respectively, in terms of their contributions to the total losses whereas under the mainshock-aftershock scenario the order is reversed. More specifically, under the mainshock-aftershock scenario the contribution of the partition walls declines by 35% relative to the mainshock-only scenario while the share of the structural elements in the total losses increases by 25%. Moreover, when aftershocks are incorporated in the loss analysis, the contribution of the collapse state to the total service life losses increases by about 70% relative to the mainshock-only scenario. The reduction in the contribution from components mostly influenced by lower demand levels (the most extreme damage state in the partition walls happens at a median SDR of 2% whereas the most severe damage state in the slabs will not occur up to a median SDR of 4% [100]) could be due to a combination of two factors. First, Table 4-3 shows that under the mainshock-aftershock scenario the likelihoods of the more severe damage states increase by a significant margin, i.e., extensive damage in the structural elements or collapse becomes more likely when aftershocks are considered. The second reason behind the more notable contribution of structural elements is the significantly higher cost associated with the repair activities required to restore the capacity of structural members or re-construct the building after it collapses. For example, after experiencing their most severe damage state, the cost of removing and replacing the structural members could be as high as 50% of the building's replacement cost whereas this number for the partition walls is less than 4% [100].

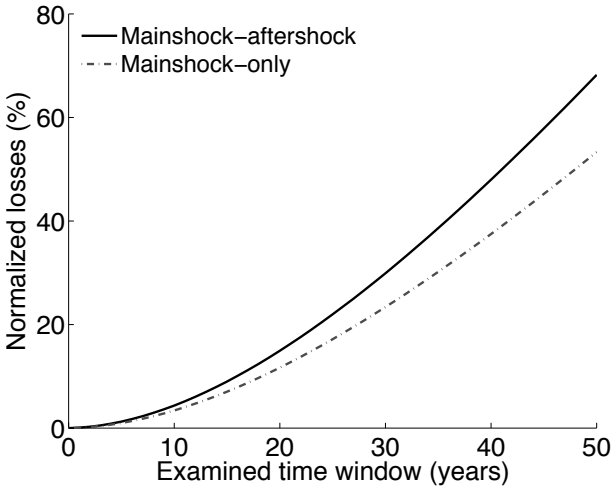

Fig. 4-9. Normalized expected present value of total mainshock-aftershock and mainshock-only losses throughout the building's service life

Table 4-4. Contribution of component groups to the total mainshock-aftershock and mainshock-only losses

Scenario	Component group					
	Structural	Partition walls	Exterior cladding	Interior finishes	Plumbing and HVAC	Collapse
Mainshock-aftershock	42	23	9	4	0	22
Mainshock-only	34	38	8	8	0	13

4.4 SUMMARY AND CONCLUSION

In recent years, research on seismic risk evaluation under sequences of ground motions in lieu of single isolated events has become increasingly popular. The gradual reduction in the structural capacity in the absence of repair measures within the first few weeks after a major mainshock event coupled with the high rate of occurrence of aftershocks during this period make structures particularly vulnerable to aftershocks. This chapter proposes a framework for lifecycle seismic loss assessment that is capable of accounting for the contribution of both the

likely mainshocks and aftershocks to the lifecycle earthquake-induced losses. The deterioration in the structural capacity as well as the time-dependency of seismic hazard in the post-mainshock environment are incorporated in the proposed methodology.

The loss assessment methodology was applied to a 4-story special reinforced concrete frame building located in a high-seismicity site. The outputs of the loss analysis in the post-mainshock environment suggested that, depending on the extent of the damage that the structure has sustained under mainshock, the aftershock-induced losses could add up to more than 7% of the replacement cost of the building. The initiation of repair measures was shown to be virtually ineffective within the first few days after mainshock due to the high rate of occurrence of aftershocks.

A lifecycle loss evaluation was also performed where seismic risk due to both mainshocks and aftershocks was included in the analysis. The contribution of aftershocks to the total earthquake-induced losses was found to be significant with the losses under mainshock-aftershock seismic sequences being up to 30% larger than the losses under the mainshock-only scenario.

It is important to emphasize that while the proposed methodology is general and can be applied to any type of structure, the findings and conclusions are limited to the 4-story moment frame structure that was used. More studies are needed to generalize the findings related to the impact of mainshock-aftershock sequences on the earthquake-induced losses in different types of buildings with distinct dynamic characteristics and damageable component distributions.

4.5 APPENDIX A

To obtain the probability density function (PDF) of the conditional arrival times used in Equation 4.11, suppose that it is known that exactly one aftershock has occurred in $[0, T]$. The conditional cumulative probability function (CDF) that the aftershock has occurred in $[0, t]$ $t < T$ can be obtained as follows [97].

$$P[T_{AS} < t | N_{AS} = 1] = \frac{P[T_{AS} < t, N_{AS} = 1]}{P[N_{AS} = 1]} = \frac{P[1 \text{ event in } (0,t) \text{ and zero events in } (t,T)]}{P[N_{AS} = 1]}$$

$$= \frac{P[1 \text{ event in } (0,t)]P[\text{zero events in } (t,T)]}{P[N_{AS} = 1]} = \frac{\lambda(0,t)e^{-\lambda(0,t)}e^{-\lambda(t,T)}}{\lambda(0,T)e^{-\lambda(0,T)}}$$

$$P[T_{AS} < t | N_{AS} = 1] = \frac{\lambda(0,t)e^{-\lambda(0,t)}e^{-\lambda(t,T)}}{\lambda(0,T)e^{-\lambda(0,T)}} \tag{4.25}$$

The probabilities are obtained using Equation 4.9 and the rates of the Poisson distributions can be found using Equation 4.10. Expanding and simplifying Equation 4.25 leads to the following relationship.

$$P[T_{AS} < t | N_{AS} = 1] = \frac{\lambda(0,t)}{\lambda(0,T)} \tag{4.26}$$

Replacing $\lambda(0,t)$ and $\lambda(0,T)$ with their functional form from Equation 4.10 yields Equation 4.27.

$$P[T_{AS} < t | N_{AS} = 1] = \frac{(t+c)^{1-\rho} - (c)^{1-\rho}}{(T+c)^{1-\rho} - (c)^{1-\rho}} \tag{4.27}$$

The PDF of the conditional arrival times can be obtained by taking the derivative of the conditional CDF in Equation 4.27 with respect to t.

$$f_{t|N_{AS}}[t | N_{AS} = 1] = \frac{1-\rho}{(T+c)^{1-\rho} - (c)^{1-\rho}}(t+c)^{-\rho} \tag{4.28}$$

4.6 APPENDIX B

As discussed in Section 4.2.1, the complexity of the calculations that involves $f_{t|N_{AS}}$ in Equation 4.25 can be avoided with a change of variable t in Equation 4.25 such that the new PDF of the arrival times will have a standard uniform distribution in the new space. In the new variable space $\tau(t)$, the probability obtained using the transformed PDF $f_{\tau(t)|N_{AS}}(\tau(t)|N_{AS})$ over an infinitesimal time step $d\tau(t)$ should be identical to the probability calculated using the initial PDF $f_{t|N_{AS}}$ in the initial variable space t.

$$f_{\tau(t)}\big(\tau(t)\big)d\tau(t) = f_t(t)dt \Rightarrow d\tau(t) = \frac{f_t(t)}{f_{\tau(t)}\big(\tau(t)\big)}dt$$

$$d\tau(t) = \frac{1-\rho}{(T+c)^{1-\rho} - (c)^{1-\rho}}(t+c)^{-\rho}dt \Rightarrow \tau(t) = \int_0^t \frac{1-\rho}{(T+c)^{1-\rho} - (c)^{1-\rho}}(u+c)^{-\rho}du$$

$$\Rightarrow \tau(t) = \frac{(t+c)^{1-\rho} - c^{1-\rho}}{(T+c)^{1-\rho} - (c)^{1-\rho}} \tag{4.29}$$

CHAPTER 5: Regional Short-Term and Long-Term Seismic Risk and Loss Assessment under Sequential Seismic Events

---

This chapter is adopted from the following study:

Shokrabadi, M. and Burton, H. V. (2018). "Regional Short-Term and Long-Term Risk and Loss Assessment under Sequential Seismic Events," *Engineering Structures* (under review)

5.1 Introduction and background

Recent seismic events in New Zealand [6], Japan [3], Nepal [104] and Italy [5] have highlighted the importance of planning for major earthquakes. A regional loss assessment that yields an estimate of the extent of earthquake-induced human and financial losses can reduce the adverse impacts by informing plans for resource-allocation to mitigate vulnerable structures, post-event search and rescue missions and repair and reconstruction. The main ingredients for performing regional seismic loss assessment are hazard maps, which provide the probability distribution of different characteristic events, exposure models, which give an estimate of the number and type of structures that can be impacted by these events and vulnerability models, which are used to estimate the probable extent of damage to the exposed infrastructure.

The past two decades have witnessed significant advancements in regional loss assessment methods and tools that have further popularized large-scale loss assessments in both literature and practice. The introduction of performance-based earthquake engineering (PBEE) [105] has provided engineers with probabilistic tools for combining the three elements of regional loss assessment. FEMA's HAZUS software and its comprehensive database [106] has facilitated loss assessment for regions in North America and the underlying methodology has been adapted into other platforms such as OpenQuake [107], which is used worldwide.. Tantala et al. [108] used HAZUS to conduct seismic loss assessment for the New York City Metropolitan Area under different probabilistic and deterministic scenarios. Their findings showed that an event with a return period of 2500 years (a maximum considered earthquake) can result in 84.8 billion dollars in losses due to the direct damage to buildings as well as the loss of income caused by disruption of the normal functionality of the buildings. Even a moderate magnitude 5 hypothetical earthquake caused an estimated 4.8 billion dollars in direct and indirect economic losses. A study by

Jaiswal et al. [109] estimated the nationwide annual financial losses due to earthquakes across the United States to be 4.5 billion dollars, with California identified as the state that most contributes to the losses. Other studies by Chen et al. [110] and Chen et al. [111] have mostly focused on estimating regional earthquake-induced losses for California, one of the most earthquake-prone states in the US.

An underlying assumption in the studies described above is the time-independence of seismic hazard. Despite being embedded in seismic design codes [112], the assumption of time-independence has been shown to be particularly violated after a major mainshock event when a swarm of aftershocks occur within a short time window [28]. Jordan et al. [113] summarized the methods and challenges for operational earthquake forecasting (OEF), which is introduced with the goal of using time-dependent seismic hazard analysis to inform authorities and public about seismic risk on time scales (hours to decades) that are normally shorter than the ones used in time-independent seismic hazard analysis. Iervolino et al. [114] demonstrated the potential use of OEF in seismic risk assessment by introducing a tool for short-term seismic risk assessment in Italy. Field et al. [115] used the seismic rates obtained from the Third Uniform California Earthquake Rupture Forecast – Epidemic Type Aftershock Sequence (UCERF3-ETAS) [116] model to calculate seismic-induced losses in the state of California from a handful of scenario mainshocks. Significant increases in the likelihoods of specific loss thresholds were observed after each of the mainshock scenarios compared to the unconditional losses, where it is assumed that no information is available about the occurrence of the scenario mainshock.

The study by Field et al. [115] has highlighted the value of a seismic hazard analysis framework that is capable of incorporating the history of seismic events in a region when calculating seismic hazard. However, what missing from the Field et al. study is the incorporation of the uncertainties that exist in the state of the buildings that are affected by a major mainshock event in the loss assessment process. When subjected to a mainshock event, the buildings are likely to lose part of their lateral load-resisting capacity. This in turn will lead to an uncertainty in their state when subjected to the aftershocks that follow the mainshock given that the duration of the high rates of aftershock occurrence is usually much shorter than the time required to restore the buildings to the their pre-mainshock states. The focus of the current study is placed on performing a regional loss assessment for the RC frames located in the County of Los Angeles. While only RC frames are considered for seismic performance assessment in this study, the main objective of the current study is to outline a framework for regional loss assessment under sequential seismic events and show

its viability rather than performing a comprehensive regional loss assessment. More specifically, we are seeking to address the two following questions.

1. The degree to which seismic risk and loss would shift when aftershocks are incorporated into the risk and loss analysis steps.
2. The extent to which seismic-induced risk and losses are affected by the uncertainties in the state of buildings when they are subjected to consecutive aftershocks within a short period.

The first step in characterizing seismic performance is to generate stochastic mainshock and aftershock ground motion maps for all the census tracts in the Los Angeles County using Monte Carlo simulations and the Intensity Measure Event Set Calculator application in OpenSHA [53] (Section 5.2). The second issue is addressed by using a Markov approach to quantify the probability of transition between different damage states that the buildings can experience when subjected to a cluster of mainshock-aftershock events [76]. The distribution of the buildings' height and code-conformity within each census tract is obtained using the HAZUS database [106].

5.2 Mainshock and Aftershock Stochastic Ground Motion Maps

Los Angeles County is divided into 2346 census tracts using the data available from the United States Census Bureau [117]. Two sets of stochastic ground motion maps are developed for each of the studied buildings (see Section 5.3 for a description of the buildings). The first set of ground motion maps characterizes all the mainshocks that are likely to happen in Los Angeles County along with their magnitudes, source-to-site distance, annual rate of occurrence and the median intensity measure recorded at each of the 2346 census tracts. The mainshock ground motion maps are generated using OpenSHA's IM Event Set Calculator application [53]. The Mean UCERF3 magnitude and source model [54] is used to generate the mainshock events and the Boore and Atkinson [56] ground motion prediction equation is used to estimate the median IM and the inter-event and total IM residuals for each magnitude and distance pair. The intensity measure is taken as the spectral acceleration at the initial first mode periods of the representative buildings $\left(S_a(T_1)\right)$. The OpenSHA outputs include more than 200,000 events. The computational effort associated with performing seismic risk and loss assessment for such a large set of events would become a major prohibitive factor in the later stages. To address this concern, the very rare events with annual occurrence frequencies smaller than 10^{-5} are first removed from the analysis. This leaves a subset of approximately 2300 events out of the initial 200,000 events. Second, a K-means

clustering approach is used to classify the 2300 events into 100 groups for each site. The events in each group are the most similar based on their median IMs [118]. The similarity between the IMs within each group are measured in terms of the squared Euclidean distance between the IMs of the individual events and the mean IMs of the events within each group. A mainshock randomly picked from the events in each of the 100 groups in taken as the representative of that group.

While OpenSHA's outputs include the median of the IM at each census tract, the more extreme IMs that deviate from the median value are usually more important for seismic loss assessment because, although rarer than the median IM, they induce higher levels of damage. To introduce IMs other than the median values into the seismic loss assessment, a set of 100 ground motion intensity maps are generated for each event. For each ground motion map, the deviations from the median due to the inter-event and intra-event variations are added separately assuming that both follow a normal distribution with zero means [119]. The standard deviations of the normal distribution of the inter-event residuals are direct outputs of OpenSHA and would remain unchanged across the 2346 sites for each mainshock event. The intra-event residuals for each mainshock follow a multivariate normal distribution where the elements of the covariance matrix are calculated using the intra-event standard deviations calculated using OpenSHA's outputs, the Boore and Atkinson [56] ground motion prediction equation and the site correlation factors obtained using the relationships suggested by Jayaram and Baker [119].

Our analyses in the later stages account for the contribution of both mainshocks and aftershocks to the seismic risk and loss. As such, for each mainshock event, a second set of ground motion maps are generated to characterize the aftershock intensity measures. Generating the aftershock ground motion maps involves two key steps.

The first step is to generate a set of aftershock events with specific magnitudes and source-to-site distances. It is assumed that the magnitude of the largest aftershocks cannot exceed that of the causative mainshock. The minimum magnitude of the aftershocks is set at 5 as events with smaller magnitudes are not expected to induce notable damage in the studied buildings. Large magnitude aftershocks are more likely to cause substantial damage. However, they are less likely to be included in the simulated event-set because of their lower frequencies of occurrence compared to the smaller events. To ensure that large-magnitude aftershocks are included without having to generate a large event-set for each mainshock scenario, the importance sampling technique described in Jayaram and Baker [118] is

employed. In this approach, the range of the minimum and maximum aftershock magnitudes for each mainshock scenario is divided into N intervals and a magnitude is sampled from each interval. All intervals have equal probabilities $(1/N)$ of being included in the sampling. By using this method, the actual cumulative probability density function (CDF) of the aftershock magnitudes (Equation 5.1) is replaced by a uniform PDF, an adjustment in the form of the importance sampling weight shown in Equation 5.2 [118]. Using this sampling scheme, 25 aftershock scenarios are generated for each mainshock event. For each aftershock scenario, the source-to-site distance is randomly sampled from the set of distances that belong to the fault associated with the causative mainshock.

$$F_{M,T}(m,t) = 1 - e^{-\lambda} \tag{5.1}$$

Equation 5.1 represents an exponential distribution with a time-varying rate λ that is calculated as shown in Equation 5.2. λ characterizes the decline in the temporal distribution of aftershock magnitudes (Equation 5.4) taking into account the decline in aftershock rate with the time elapsed since the occurrence of the causative mainshock (Equation 5.3) [55].

$$\lambda = \lambda_t \lambda'_m \tag{5.2}$$

$$\lambda_t = \frac{(t+c)^{1-\rho} - (t_0+c)^{1-\rho}}{1-\rho} \tag{5.3}$$

$$\lambda'_m = -\ln\left(1 - \frac{e^{-\lambda_{m_0}} - e^{-\lambda_m}}{e^{-\lambda_{m_0}} - e^{-\lambda_{m_m}}}\right) \tag{5.4}$$

a and b in Equation 5.3 are constants that characterize the magnitude distribution and c and ρ are constants that define the temporal decay in the number of aftershocks adopted from the aftershock model suggested by Reasenberg and Jones [55]. In Equation 5.4, m_0 and m_m are the minimum and maximum magnitudes of aftershocks and $\lambda_m = 10^{a-bm}, \lambda_{m_0} = 10^{a-bm_0}$ and $\lambda_{m_m} = 10^{a-bm_m}$.

The second step in developing aftershock ground motion maps involves calculating the expected $S_a(T_1)$ values and the inter- and intra-event standard deviations for each aftershock scenario. This is done using the magnitude and distance calculated for each aftershock scenario in Step 1 and the Boore and Atkinson [56] ground motion prediction equation. Once the mean $S_a(T_1)$ values and the inter- and intra-event standard deviations are obtained for each aftershock scenario, 10 ground motion intensity maps are generated for each aftershock

scenario following the same procedure as the mainshocks'. The Wooddell and Abrahamson's aftershock distance criterion is used to determine the distance domain within which aftershocks can happen. This approcah is common in identifying the aftershocks of a mainshock seismic event and is utilized by PEER in classifying mainshock and aftershock records in NGA-West2 database. However, Epidemic Type Aftershock Sequence (ETAS) model, where each aftershock could trigger its own sequence of aftershocks, can potentially be a better replacement for the model employed in this study for identifying aftershocks. Fig. 5-1 shows the census-track division for Los Angeles County.

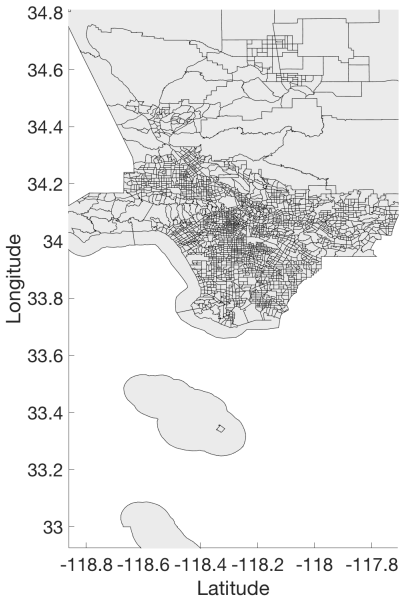

Fig. 5-1 Los Angeles County census tracts

To demonstrate the potential increase in seismic hazard after a major mainshock, Fig. 5-2 compares the daily probabilities of $S_a(T = 1s)$ values associated with the serviceability (50% probability of exceedance in 30 years [120]) hazard level. Fig. 5-2a and Fig. 5-2b show the increase in the daily probabilities of the service level S_a values one day and one week after a magnitude 7.0 mainshock event on the Puente Hills fault, respectively. The Puente Hills fault is selected here as it has been shown to be capable of generating the most damaging earthquake scenario in Southern California [110]. For the mainshock PSHA, all the faults that contribute significantly to the total seismic hazard in Los Angeles County are included in the seismic hazard analysis while the APSHA is only performed for Puente Hills fault system. In other words, we assume that a mainshock on a specific fault can only trigger aftershocks on that fault while the other faults in the region would remain intact. The probability ratios in Fig. 5-2a indicate that within the first day after the mainshock the daily probability of the service-level spectral accelerations on average increases by a factor of 13; a

significant gain whose implication for risk and loss analyses will be discussed later in Sections 5.4 and 5.5. The average increase in the daily probability of the service-level spectral acceleration drops to approximately 4 within one week after the mainshock.

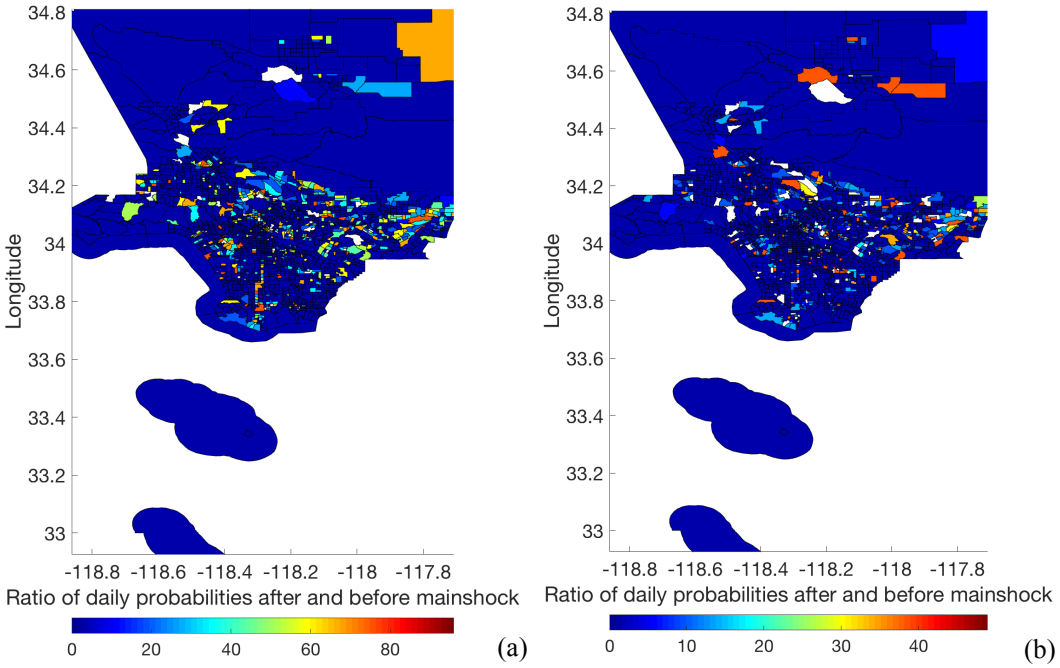

Fig. 5-2 Increase in the daily probability of the service-level mainshock $\boldsymbol{S_a(T = 1s)}$ a) one day and b) one week after a magnitude 7.0 mainshock on the Puente Hills fault

5.3 Seismic Risk and Loss Assessment Methodology

5.3.1 Seismic risk assessment under sequential ground motions

As discussed in detail in Chapter 3, aftershocks typically happen within a relatively short time window after the mainshock. Therefore, it is highly unlikely that mainshock-damaged structures are repaired before the occurrence of subsequent aftershocks. The approach to quantify seismic risk under such circumstances are discussed in Chapter 3. Here, we give a brief overview of the steps that are needed to be taken to accurately characterize seismic risk under sequential seismic events.

Seismic risk assessment under successive seismic events requires a framework that can account for the accumulation of damage while buildings are subjected to a sequence of ground motions without repair. This can be done using two approaches. The first involves performing multiple response history analyses on the structure by subjecting it to all the ground motions in the sequence. This method allows for directly quantifying the impact of each ground motion in the sequence with its unique characteristics on the state of the

structure. However, response history analyses are usually done on complex nonlinear numerical models to better represent the accumulation and distribution of damage in the structural members. As such, running multiple dynamic analyses using a number of ground motions could be computationally expensive; especially when multiple numerical models are involved in the analyses to better represent the diverse building inventory of a region.

An alternative approach to multiple-sequence response history analyses is a probabilistic framework that computes the probability of each limit state at the end of any of the ground motions in the seismic sequence and before it is subjected to the next record. The viability of a Markovian framework for this purpose has been shown before in a number of studies [76, 78]. The uncertainty in the state of the structure in the Markov process is incorporated in the risk analysis through the Markov transition matrix whose elements are the probabilities of transitioning between r predefined limit states as shown in Equation 5.5.

$$\mathbf{\Pi} = \begin{bmatrix} P_{11} & P_{12} & \cdots & P_{1r} \\ 0 & P_{22} & \cdots & P_{2r} \\ \vdots & \vdots & \ddots & \vdots \\ 0 & 0 & \cdots & 1 \end{bmatrix} \tag{5.5}$$

The P_{ij} terms in Equation 5.5 represent the probability that the structure transitions to damage state j when subjected to an event in a cluster given that it has already experienced damage state i under the previous event. The lower diagonal elements can also be populated with non-zero values if repair measures are deemed plausible during the period that the building is subjected to a seismic sequence. At time step m after the occurrence of the mainshock, the probability that the structure is in damage state j given that it has already undergone damage state i under the mainshock is equal to the element on row i and column j of the $\boldsymbol{P^m}$ matrix in Equation 5.6.

$$\boldsymbol{P^m} = \prod_{i=1}^{m} \mathbf{\Pi}(\mathbf{t_{i-1}}, \mathbf{t_i}) \tag{5.6}$$

If the risk analysis is performed in the pre-mainshock environment, then the uncertainties in the occurrence of mainshock seismic events as well as the state of the structure once it is subjected to a mainshock must be incorporated in the risk assessment. This can be done through Equation 5.7 where $\left(P_{1,n}^{MS}, \ldots P_{r,n}^{MS}\right)$ is the vector of limit state probabilities under a potential mainshock event and N_s is the total number of sources that contribute to the seismic hazard at the location of the structure.

$$\boldsymbol{P}_{\boldsymbol{PreMS}}^{\boldsymbol{m}} = \sum_{n=1}^{N_s} \left(\left(P_{1,n}^{MS}, \dots P_{r,n}^{MS}\right) \prod_{i=1}^{m} \boldsymbol{\Pi}_{\boldsymbol{n}}(\boldsymbol{t_{i-1}}, \boldsymbol{t_i}) \right) \tag{5.7}$$

More details on the application of the Markov process in seismic risk assessment can be found in Chapter 3 and Shokrabadi and Burton [121].

5.3.2 Seismic loss assessment under sequential ground motions

The Markov process approach can also be used for the seismic loss assessment as discussed in Chapter 4. Here, we give a brief overview of the mainshock-aftershock seismic risk assessment framework discussed in Chapter 4.

Yeo and Cornell [76] demonstrated the steps and relationships that are necessary for quantifying losses under mainshock-aftershock seismic sequences using a Markovian framework. An alternative framework is discussed in Shokrabadi and Burton [122] which is also adopted in this study for its robust probabilistic basis and simplicity. A brief overview of the approach is given here. Interested readers are referred to Shokrabadi and Burton [122] for a detailed description of the approach.

In the post-mainshock environment, the expected value of losses at time step t_m after the mainshock can be calculated using Equation 5.8 where $\boldsymbol{P^m}$ is the limit state transition matrix of Equation 5.6. $\boldsymbol{E^{t_m}[C_{AS}]}$ is the matrix with the total expected cumulative aftershock-induced losses. $\boldsymbol{E_C}$ is the matrix of the expected losses due to building structural and non-structural damage, $\boldsymbol{E_D}$ is the matrix that contains the expected losses due to the disruption in the normal functionality of the building and $\boldsymbol{E_D^{t_{m-1}}}$ is the disruption losses in the previous time step (t_{m-1}). The $\circ$ symbol is for the element-by-element multiplication of the $\boldsymbol{P^m}$ and $\boldsymbol{E_C + E_D}$ matrices. The elements of the $\boldsymbol{E_C + E_D}$ matrix at each step can be calculated as $E_{ij} = e^{-\alpha T_m} E\left[C_{ij} + C_{d_j}\right]$ where C_{ij} is the direct losses due to the additional damage in the structural and non-structural components when the building moves from damage state i to damage state j and C_{d_j} is the disruption losses when the building resides in damage state j.

$$\boldsymbol{E^{t_m}[C_{AS}] = P^m \circ (E_C + E_D) + E_D^{t_{m-1}}} \tag{5.8}$$

In the pre-mainshock environment, any loss assessment procedure should account for the fact that both mainshocks and aftershocks cause earthquake-induced losses. Equation 5.9 can be used to combine the total losses due to probable mainshocks and aftershocks during the service life of the building. $E_i[T_L]$ in Equation 5.9 is the expected value of total losses

associated with damage state i, λ_n is the rate of mainshocks on seismic source n, α is the discount factor and T_L is the time window during which seismic loss assessment is performed. $P[DS_{1i}^n]$ represents the probability that the building would experience damage state DS_i under a mainshock given that it was previously in the intact state (DS_1). $E[C_{1i}]$ is the total losses that occur when the building transitions from the intact state to the damage state i and $E[C_{AS}|DS_i]$ is the expected aftershock losses conditioned on each probable mainshock (Equation 5.8).

$$E_i[T_L] = \sum_{n=1}^{N_S} \frac{\lambda_n(1 - e^{-\alpha T_L})}{\alpha} P[DS_{1i}^n](E[C_{1i}] + E[C_{AS}|DS_i]) \tag{5.9}$$

When losses under a Mainshock-Only scenario (aftershocks are excluded from loss assessment) are calculated, Equation 5.9 simplifies to Equation 5.10.

$$E_i[T_L] = P[DS_{1i}^n]E[C_{1i}] \tag{5.10}$$

5.4 Building inventory and numerical models

The main focus of the current study is to estimate the financial losses caused by earthquake-damage to RC frame buildings in the County of Los Angeles. HAZUS [123] identifies the height ranges of 1-3, 4-7 and 8+ stories for low-, mid- and high-rise RC frame buildings, respectively. In this study, a group of three 2-, 4- and 8-story RC frame buildings are used to represent the inventory of RC frame buildings in the Los Angeles County.

The buildings are divided into three groups. The first group represents the typical design of ductile RC moment frames that meets the special seismic requirements of modern design codes. The second group represents RC moment frame buildings whose design dates back to the era where adopting special seismic requirements for structures in high-seismicity zones was not a common practice. Nonductile concrete buildings have been shown to be a source of major seismic risk to the communities where their presence is significant [124]. A recent database compiled by Anagnos et al. [124] has put the replacement value of approximately 1500 nonductile concrete buildings at 17 billion dollars. The issue of seismic risk in nonductile concrete buildings becomes more important when the significantly higher vulnerability of such buildings to seismic events compared to ductile buildings is considered. Liel et al. [125] showed that the mean annual frequency of collapse in an RC moment frame designed based on the 1967 Uniform Building Code provisions could be up to 40 times higher than a similar building that meets the requirements of recent seismic design codes. The

third group of RC frames are concrete frames with unreinforced masonry walls, which are likely to be the most significant source of seismic risk among the three groups of studied RC frame buildings [126].

The numerical models of three 2-, 4- and 8-story nonductile RC frames, which were designed following the requirements of 1967 Uniform Building Code by Raghunandan et al. [127], are used to simulate the seismic response of the non-ductile RC moment frames. The designs of the ductile RC moment frames are assumed to be equivalent to the High-Code and Moderate-Code seismic design levels of HAZUS whereas the nonductile frames are assumed to be representatives of buildings that are in the Low-Code and Pre-Code seismic design categories based on HAZUS' classification of seismic design and detailing. The numerical modeling of the RC frames with masonry infill walls follows that of the nonductile RC moment frames. However, diagonal and off-diagonal struts are added to the three bays of the nonductile moment frames to account for the impact of masonry infills on the seismic behavior of the nonductile RC moment frames following the modeling approach suggested by Burton and Deierlein [126].

The numerical models of the ductile frames are adopted from the set of models developed by Haselton [46]. The designs follow the requirements of ACI 318-02 and ASCE 7-05 [ASCE 47, ACI 48], including the seismic provisions of Chapter 21 of ACI 318-02. All buildings have a three-bay moment frame as the lateral force resisting system. The numerical model of the moment frame for each building is constructed in OpenSees [49]. Beams and columns are modeled with flexural plastic hinges at the member-ends connected through an elastic element. The hinges are modeled using the trilinear backbone curve developed by Ibarra et al. [50], which incorporates strength and stiffness deterioration. The properties of the plastic hinges are obtained using the empirical relationships developed by Haselton [46]. The nonductile frames are prone to shear and axial failure in columns, which can drastically affect their structural capacity. These modes of failure are incorporated in the numerical models using shear and axial springs at the top ends of the columns of the nonductile frames. More details on the nonductile concrete frame modeling can be found in Raghunandan et al. [127].

The distribution of the buildings at each census tract is obtained from the HAZUS database[106], which puts the estimate of the total number of nonductile and ductile RC frame buildings as well as RC frames with masonry infills at 733, 5315 and 1781 for the entire Los Angeles County. Wherever possible, the HAZUS database was augmented with a database of approximately 1500 concrete buildings collected specifically for the City of Los

Angeles [124]. The estimated replacement cost of the entire set of buildings across Los Angeles County is 17 billion dollars and the value of the contents of the buildings is 45 billion dollars after adjusting for inflation assuming an average rate of 3%.

A set of 24 mainshock-aftershock records from actual seismic sequences is used to analyze the buildings. The seismic sequences are from the Class 1 (mainshock) and Class 2 (aftershock) records of the Northridge, Livermore, Coalinga, Landers, Mammoth Lakes 01, Whittier Narrows, Darfield and Chi-Chi earthquakes, which are adopted from the PEER-NGA West2 database [67]. The magnitudes of the mainshocks range from 5.8 and 7.6 and the aftershocks are from events with magnitudes ranging between 5.2 and 6.5. Each building is assumed to be in one of four pre-defined distinct damage states after a seismic event; namely Slight, Moderate, Extensive and Complete. The definitions of the damage states are adopted from the fragility curves defined in HAZUS [123] for Low-Code and High-Code seismic design levels. The damage states are quantified based on the maximum SDR. The limit state transition probabilities needed to populate the elements of the Markov transition matrix in Equation 5.5 are calculated by fitting a lognormal distribution to the ground motion spectral accelerations associated with each of the damage states [59]. To calculate the residual capacity of the buildings when they have sustained some level of mainshock-damage, first, mainshock ground motions are scaled incrementally to each of the four SDR levels and then incremental dynamic analysis is used to obtain the aftershock damage fragility curves conditioned on each mainshock state. Fig. 5-3 compares the structural capacity of the 2-story ductile and nonductile RC moment frame buildings as well as the RC frame building with masonry infills in terms of their associated fragility curves for the Complete damage state. Fig. 5-3 shows that, when the buildings remain intact when subjected to the mainshock ground motions, the median S_a value that leads to the Complete damage state in the ductile 2-story RC moment frame under the aftershock ground motions is approximately 15% and 50% higher compared to the other two 2-story RC frame buildings.

The losses at each damage state are the aggregated structural, nonstructural drift-sensitive and nonstructural acceleration-sensitive repair costs. The losses due to the disruption in the normal functionality of the buildings are also incorporated. Such losses are divided into two parts [123]; the losses due to shifting and transferring and the loss of rental income [123]. The rental income loss is only applied to the damage states beyond the Moderate limit state as the temporary relocation of tenants is unlikely to occur at the lower damage states. All losses are adjusted for inflation as the values suggested by HAZUS [123] are estimates for the year 2002. All losses reported in later sections are normalized with

respect to the replacement cost of the buildings to offset the impact of errors in the cost estimation on the loss evaluation.

Under successive ground motions, the expected differential losses associated with transition from damage state i to a more severe damage state j is taken as the difference in the losses associated with the two damage states, i.e., $E_{ij} = E_j - E_i$. The possibility of repair, although absent from this study, can be incorporated in the loss assessment by assuming exponentially distributed repair times and that repair activities can only restore the building to the intact state.

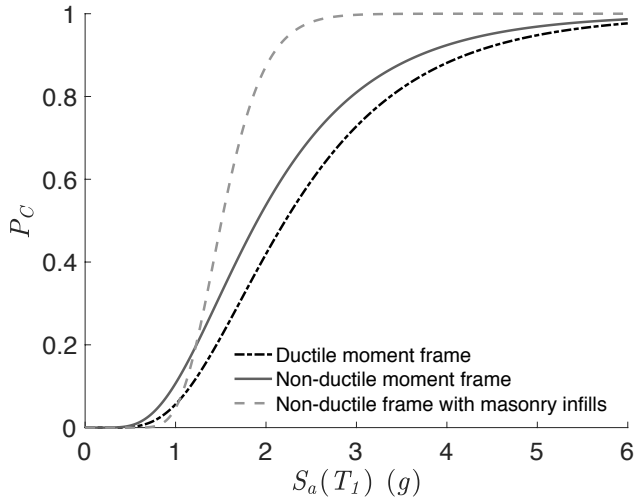

Fig. 5-3 Aftershock damage fragility curves for the RC frame 2-story buildings conditioned on the intact state under the mainshock ground motions

5.5 Seismic risk

Earthquake-induced losses are a direct function of seismic risk. As such, the first step in assessing the seismic losses in a building is to evaluate its seismic risk. Seismic risk is the convolution of the structural capacity (vulnerability) as well as the seismic hazard in the vicinity of its site location. In this study, seismic risk is measured as the probability of exceedance of each damage state and the mean annual number of buildings in each damage state. Three different scenarios are considered when reporting seismic risk. The first scenario measures seismic risk in an environment where only mainshock events are considered. This is the scenario that has mostly been addressed in previous studies. We call this type of seismic risk assessment the Mainshock-Only scenario. In the second scenario, denoted as Mainshock-Aftershock, both mainshocks and aftershocks are considered in the seismic risk assessment using the framework discussed in Section 5.3.1. In both the Mainshock-Only and Mainshock-Aftershock scenarios, no mainshock is assumed to have happened and therefore the

uncertainty in the occurrence of mainshocks is incorporated in the seismic risk assessment procedure. These two scenarios provide the type of seismic risk assessment that constitutes the basis of risk-targeted seismic design codes and can provide a picture of the most risk-prone regions in a county and inform retrofit policy and planning. The third scenario, referred to as Puente Hills Aftershocks, includes the case where a mainshock of magnitude 7 has occurred on the Puente Hills fault and the buildings are now subjected to the probable subsequent aftershocks for a period of seven days when the rate of aftershocks is at its highest. This scenario would provide insights into the seismic risk during a period immediately following a major mainshock event on one of the most important faults that affect the seismic hazard in Los Angeles.

Fig. 5-4a shows the ratios of the mean frequency of exceedance of the Complete damage state (λ_c) over a year obtained under the Mainshock-Aftershock scenario to the λ_c of the Mainshock-Only scenario, for the 4-story ductile building. For most census tracts, the increase in the annual rate of Complete Damage is between 2% to 40%, which is increased by an average of 10% across all census tracts. Fig. 5-4b shows how the ratio of probability of the Complete damage state (P_c) calculated under the Puente Hills Aftershocks scenario compares with the P_c calculated under the Mainshock-Only scenario for a period of one day immediately after the magnitude 7 mainshock. The P_c values associated with the Puente Hills Aftershocks scenario are calculated assuming that the buildings remain intact when subjected to the magnitude 7 mainshock that precedes the aftershocks. As such, the ratios displayed in Fig. 5-4b are the most optimistic scenario where the potential impact of the mainshock on the structural capacity of the buildings represented by the 4-story structure is neglected. While P_c in the post-mainshock environment remains relatively small at 1.5×10^{-3}, the P_c ratios in Fig. 5-4b suggest a substantial increase in the probability of the Complete damage state within a week after the occurrence of the mainshock. This increase, which on average is about 280 times, highlights the impact of the temporarily-elevated seismic activity after a major mainshock on the seismic risk of the buildings located in the zone of impact of the mainshock. Field et al. [115] also reported substantial gains of 250 to 1678 times in the probabilities of exceedance of specific loss thresholds calculated for the entire state of California one day after a magnitude 7.0 mainshock on the Mojave section of the Southern San Andreas fault. However, despite the significant initial increase in the seismic risk under the Puente Hills Aftershocks scenario, the exponential decrease in the rate of aftershocks means that this seismic risk would rapidly decline to the pre-mainshock level. As an example, the P_c values under the Puente Hills Aftershocks scenario during the second week after the

mainshock is on average 70 times larger than the P_c under the Mainshock-Only scenario, which indicates a reduction of four times in the probability of occurrence of the Complete damage state within a week after the mainshock's occurrence.

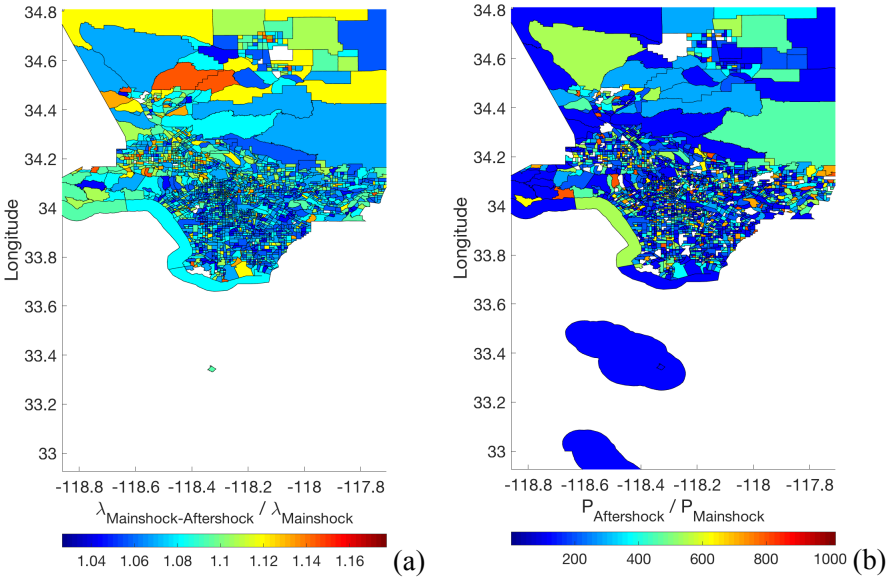

Fig. 5-4a) Ratio of annual $\boldsymbol{\lambda_c}$ values under the Mainshock-Aftershock scenario to those of the Mainshock-Only and b) ratio of daily $\boldsymbol{P_c}$ values under the Puente Hills Aftershocks scenario to those of the Mainshock-Only for the 4-story ductile building

Similar comparisons between λ_c and P_c obtained for each of the three described scenarios for the 4-story nonductile buildings are presented in Fig. 5-5. Expectedly, the nonductile buildings are more vulnerable when subjected to sequential ground motions. This is reflected in the increase in the annual λ_c under the Mainshock-Aftershock compared to the Mainshock-Only scenario, which is between 5% and 50% with an average increase of 15%. The ratio of weekly P_c associated with the Puente Hills Aftershocks scenario and within the first day after the mainshock is on average 350 times larger than the P_c under the Mainshock-Only scenario within the same period.

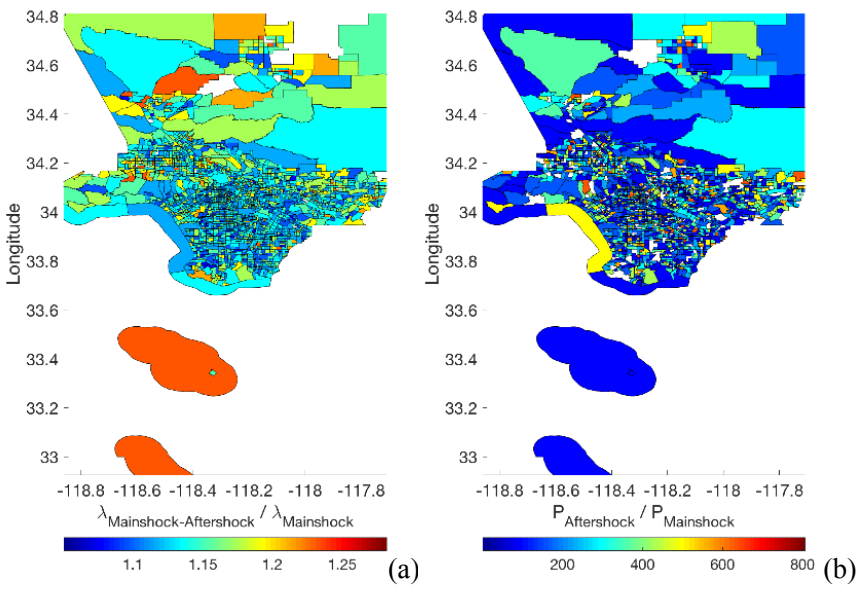

Fig. 5-5a) Ratio of annual $\boldsymbol{\lambda_c}$ values under the Mainshock-Aftershock scenario to those of the Mainshock-Only and b) ratio of daily $\boldsymbol{P_c}$ values under the Puente Hills Aftershocks scenario to those of the Mainshock-Only for the 4-story nonductile building

The ratios of the expected annual number of buildings in each damage state under the Mainshock-Aftershock scenario to that under the Mainshock-Only scenario, is shown in Fig. 5-6 for each census tract. The expected number of buildings in each of the four damage states increases by 2% to 35% when aftershocks are incorporated in the loss assessment. For the Mainshock-Aftershock scenario, the total expected annual number of buildings in the Slight, Moderate, Extensive and Complete damage states is approximately 135, 77, 22 and 19 in the entire Los Angeles County. Whereas, when aftershocks are omitted from risk assessment, these numbers reduce to 109, 66, 20 and 17. The shares of the three building groups (ductile RC moment frames, non-ductile RC moment frames and RC frames with infills) in the expected annual number of buildings that experience each of the four damage states are shown in Fig. 5-7 for the Mainshock-Aftershock scenario. Given that the ductile moment frames have the highest number of the buildings in the database, it is not surprising that they make the greatest contribution to the annual expected number of buildings in all four damage states. Ductile moment frames are closely followed by the nonductile frames with masonry infills despite the fact that the number of the buildings classified as infills frames is less than 1/3 of those grouped in the ductile moment frame category.

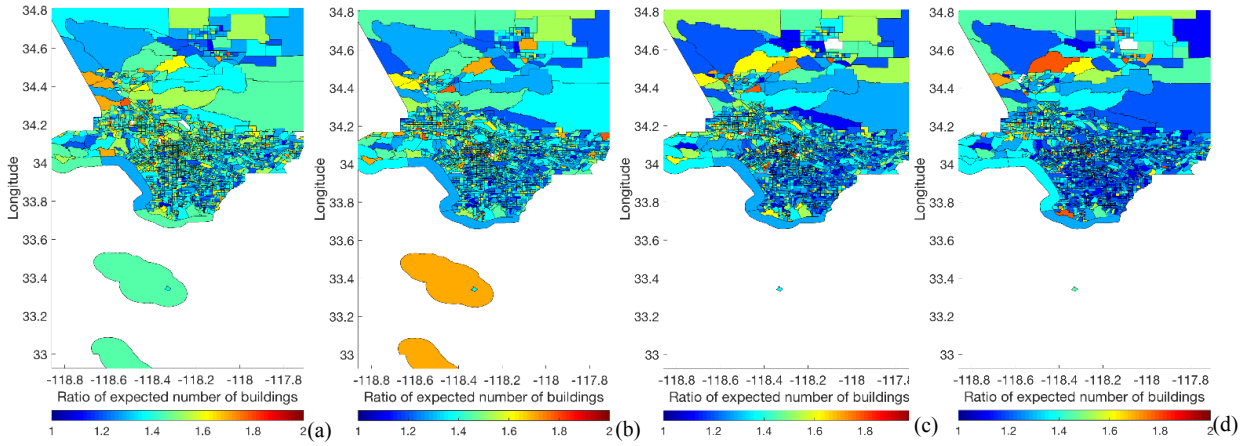

Fig. 5-6 Ratio of the expected annual number of buildings in a) Slight, b) Moderate, c) Extensive and d) Complete damage states under the Mainshock-Aftershock and Mainshock-Only scenarios

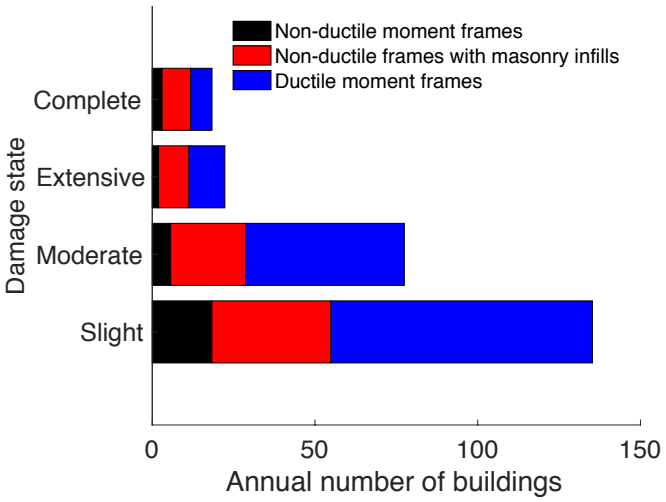

Fig. 5-7 Contributions of each building groups to the annual expected total number of the buildings in the four damage states

To demonstrate the importance of incorporating uncertainties in the building-state under a sequence of ground motions, we re-ran the risk analyses under the Mainshock-Aftershock scenarios ignoring the uncertainty in the state of the buildings in each census tract during the seven-day aftershock hazard period. This is an unrealistic scenario where buildings are essentially assumed to be in the intact state after the mainshock. The buildings are also assumed to be restored to the intact state if damaged by an aftershock and before being subjected to the next aftershock. The outputs of this type of risk analysis shows that in the absence of a proper framework for probabilistically considering the state of the buildings in the aftershock environment, the estimate for the number of buildings in the four damage states drops by 5% to 13%.

5.6 Seismic loss

Similar to risk assessment, seismic losses are calculated for the three scenarios described earlier. Losses for the Mainshock-Only and Mainshock-Aftershock scenarios are reported as mean annual expected losses whereas losses under the Puente Hills Aftershocks scenario are calculated for a period of one week starting from the occurrence of the magnitude 7 mainshock given the mainshock-induced building damage level. The expected annual losses for each census tract under the Mainshock-Only and Mainshock-Aftershock scenarios are shown in Fig. 5-8a-b. Fig. 5-8c shows the ratios of the expected annual losses calculated under the Mainshock-Aftershock scenario to the expected annual losses calculated under the Mainshock-Only scenario for each census tract. The maximum expected annual loss across all census tracts in Los Angeles County is approximately 55 thousand dollars under the Mainshock-Only scenario with a median of 12 thousand dollars. When aftershocks are considered, the maximum and the median expected annual losses increase to 65 and 16 thousand dollars. The total mean annual losses for the entire County of Los Angeles is 54 million dollars under the Mainshock-Only and 67 million dollars under the Mainshock-Aftershock scenarios; suggesting that aftershocks would increase the total losses by approximately 25%. If uncertainties in the building-state in the aftershock environment are omitted from the loss analysis, the total mean annual losses would reduce to 55 million dollars, which indicates an estimation error of 17% in the annual expected loss estimate. The individual contributions of each of the three building groups to the annual expected losses under the Mainshock-Aftershock scenario are illustrated in Fig. 5-9. The ductile moment frames contribute the most in the annual expected losses. This is not a surprising outcome given that the total replacement cost of the ductile frames is estimated at 10.3 billion dollars whereas the replacement costs of the non-ductile moment frames and the frames with masonry infills are 1.7 and 5.0 billion dollars. Nonductile frames with masonry infills, despite having a total replacement cost of less than half the ductile moment frames, make the second biggest contribution to the annual expected losses with a share that is just slightly below that of the ductile moment frames. It is important to note, the nonductile buildings, despite having a lower contribution to the total annual losses, pose a significantly higher seismic risk to their residents due to their higher collapse likelihood. This is reflected in median annual collapse risk of the nonductile moment frames which is on average four times higher than the annual collapse risk of the ductile moment frames.

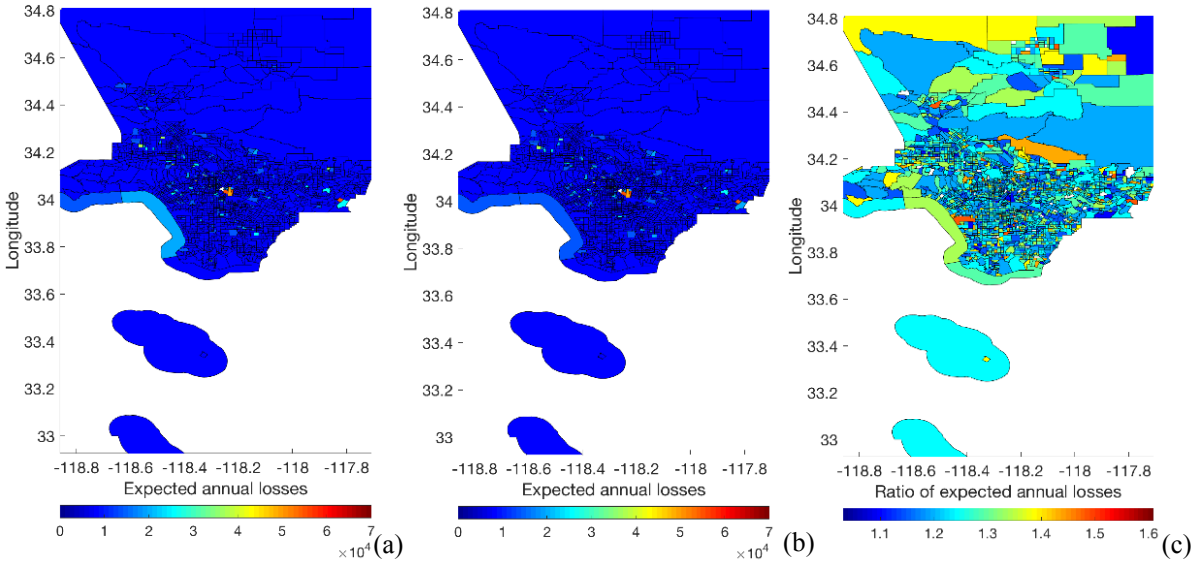

Fig. 5-8 a) Census tract expected annual losses for Mainshock-Only, b) Census tract expected annual losses for Mainshock-Aftershock scenarios and c) Census tract ratios of Mainshock-Aftershock to Mainshock-Only expected annual losses

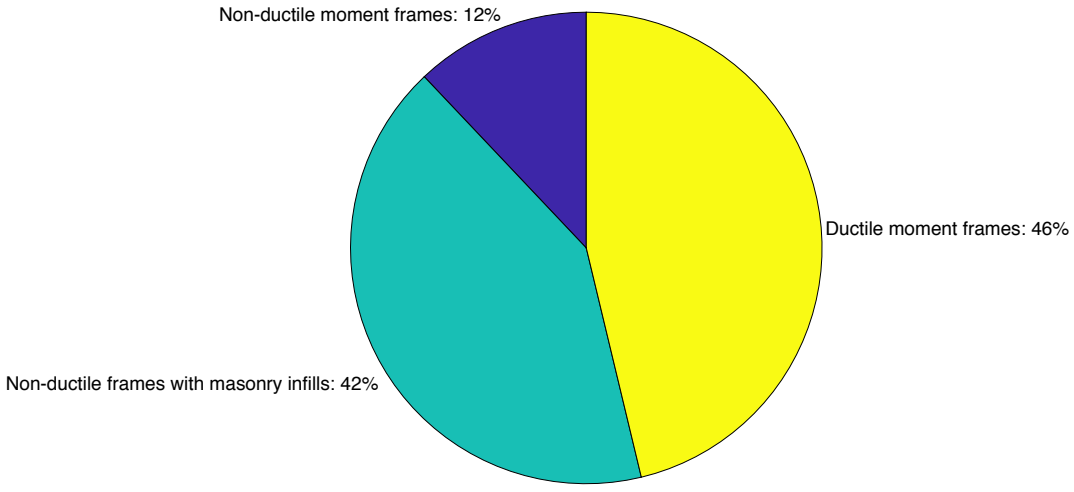

Fig. 5-9 Individual contributions of the three building groups to the total annual expected losses under the Mainshock-Aftershock scenario

The incremental total expected losses for the entire Los Angeles County due to the aftershocks that follow the magnitude 7 mainshock on the Puente Hills are expected to be up to 650 million dollars. The total building replacement losses from the magnitude 7 scenario mainshock itself is estimated at about 2.8 billion dollars; suggesting that the losses due to the aftershock could be as high as 1/4 of the total losses due to the mainshock event. The expected losses for each census tract under each of the two described scenarios are shown in Fig. 5-10.

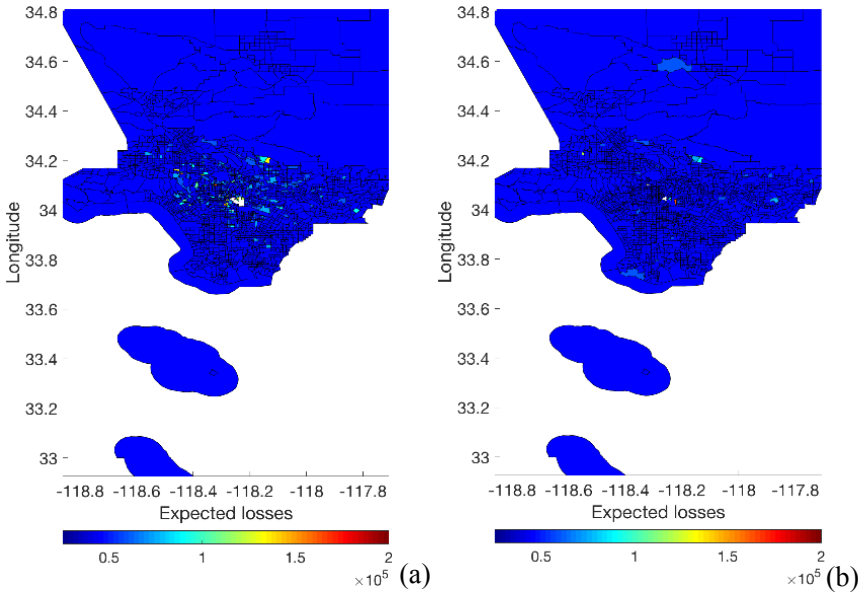

Fig. 5-10 Census tract expected annual losses for a) the Puente Hills 7 mainshock and b) the aftershocks of the 7 Puente Hills mainshock

5.7 Conclusion

Recent studies have highlighted the role of aftershocks in exacerbating seismic risk. A framework for regional seismic performance assessment, which incorporates aftershocks in the evaluation process was presented in this study. The impact of aftershocks on earthquake-induced risk and losses was computed while incorporating the reduction in the structural capacity of buildings under successive ground motions and the time dependent hazard in the post-mainshock environment.

When the seismic risk assessment framework was applied to the inventory of RC frame buildings located in Los Angeles County, the inclusion of aftershocks increased the annual rate of experiencing the Complete (HAZUS) damage state by up to 50% compared to when only mainshocks are considered. A short-term risk assessment was performed for a duration of one week starting immediately after a magnitude 7.0 on the Puente Hills fault. The significant temporary increase in the seismic activity as well as the reduction in the structural capacity of mainshock-damaged buildings increased the risk of Complete damage, on average, by a factor of 280.

Seismic loss assessment was also performed for Los Angeles County under the same scenarios used for seismic risk evaluation. It was observed that including aftershocks could increase the expected annual seismic losses by 25%. During a one-week period immediately

following the magnitude 7.0 scenario mainshock on the Puente Hills fault, aftershock losses were found to be as much as 25% of the mainshock-only losses.

It is important to emphasize that the main purpose of this study was to demonstrate the viability of the discussed approach for large scale seismic risk and loss assessment. The aftershock seismic hazard calculations performed in this study use source models that are simpler than, for instance, the UCERF3-ETAS model. Moreover, the correlation between the building responses at adjacent sites is ignored in the seismic risk and loss assessment. However, the proposed methodology can be integrated with any model used for seismic hazard and risk assessment.

CHAPTER 6: Conclusion, Limitations and Future Work

6.1 Overview

The primary objective of the current building seismic design provisions is to protect the lives of the residents during a major seismic event. Recently, there has been a shift in the design objectives of seismic design codes from targeting specific seismic hazard levels in the design steps to targeting specific seismic risk level. For example, ASCE 7 now has a collapse risk of 1% embedded in its seismic design requirements. This is achieved by setting requirements that would prevent catastrophic structural failure and collapse in the conforming building if the buildings are subjected to a strong ground motion.

However, one limitation of the current seismic design provisions is that they are based on seismic design maps that only include mainshocks and neglect the potential contributions of aftershocks to the seismic risk that a building can experience during its lifetime. Aftershocks, due to the substantial increase in seismic activity after a major mainshock event and the reduction in the structural capacity of buildings as they are being subjected to subsequent ground motions within a short period of time, can pose a significant risk to buildings.

The focus of this study was mainly placed on formulating frameworks for seismic risk and loss evaluation that are capable of incorporating the impact of both mainshocks and aftershocks on buildings seismic performance. The methodologies proposed in this study can be viewed as an extension to the current PBEE's framework for building seismic performance evaluation that would enable it to quantify the effect of aftershocks on seismic risk and loss in addition to the role of mainshocks. More specifically, the issues that addressed in this study can be summarized as follows.

- Investigating the differences in the frequency contents of mainshock and aftershock ground motions and their potential impact on different ground motion pairing strategies (Chapter 2).
- Formulating a framework for seismic risk evaluation under mainshock-aftershock seismic events that would eliminate the need for costly sequential response history analysis under multiple ground motion sequences while preserving a great degree of accuracy (Chapter 3).
- Proposing an approach for seismic loss assessment under sequential seismic event based on the seismic risk evaluation framework of Chapter 3 (Chapter 4).

- Applying the two frameworks to short-term and long-term seismic risk and loss evaluation for the inventory of RC frame buildings in Los Angeles County with the goal of quantifying the impact of aftershocks on the seismic performance metrics in a high-seismicity zone.

6.2 Findings

6.2.1 Chapter 2: Impact of Sequential Ground Motion Pairing on Mainshock-Aftershock Structural Response and Collapse Performance Assessment

This chapter was mainly focused on evaluating the implications of different record-pair selection approaches for the outcomes of sequential nonlinear response history analysis. In the absence of a comprehensive database for aftershock ground motions recorded from past seismic events, it has become common in practice to use mainshock-mainshock ground motions to form sequential ground motion pairs in lieu of mainshock-aftershock records. We evaluated the structural performance of five ductile reinforced concrete frames with varying heights using sequential nonlinear response history analyses. Systematic differences in the frequency content of mainshock and aftershock records were observed, which in turn led to notable differences in structural responses of the studied buildings. The outcome was measurable differences in the structural response, with mainshock-mainshock sequences potentially over- or under-estimating seismic demand and risk relative to the use of more appropriate mainshock-aftershock record pairs. This finding held true even when mainshock-mainshock sequences are formed by preserving the magnitude and distance relationships between as-recorded mainshocks and aftershocks. The correlation between event terms of mainshock and aftershock ground motions recorded from the same sequence was found to have a significant impact on maximum story drift ratio. We provide recommendations for aftershock record selection that drew upon these results.

6.2.2 Chapter 3: risk-based assessment of aftershock and mainshock-aftershock seismic performance of reinforced concrete frames

A framework for seismic risk assessment under sequential seismic events was presented in this chapter. The proposed framework is capable of quantifying the impact of both the elevated post-mainshock seismic hazard as well as the mainshock-induced structural damage on the seismic risk that a building is likely to experience after a mainshock event. The seismic hazard due to sequential earthquakes was examined in both pre- and post-mainshock environments. A Markov framework was utilized to incorporate the time-dependent nature of

seismic hazard in the post-mainshock environment into the risk assessment steps. The viability of the framework was demonstrated by applying to a set of ductile RC moment frame buildings. In the post-mainshock environment, the seismic risk was examined as a function of the time elapsed since the mainshock's occurrence while in the pre-mainshock environment, the risk was investigated during an assumed lifespan of 50 years for the studied structures. For the buildings and the high-seismicity site used in this study, both the increased post-mainshock seismic hazard as well as the reduction in the structural capacity are found to have a great influence on the seismic risk.

We showed that the extent of the damage that a building experiences under mainshock plays a major role in the seismic risk that it is exposed to as it is being subjected to the subsequent aftershocks. For example, depending on the building's height and configuration, the aftershock collapse probability within a 30-day period after a scenario mainshock would increase by a factor of 1.5-9 when it experiences a maximum story drift ratio of 3% under the mainshock compared to when it remains intact when subjected to the mainshock. In the pre-mainshock environment, when aftershocks were incorporated in the risk evaluation steps, they were shown to increase the lifetime collapse risk by a factor of 1.5-3.5 compared to when only mainshocks are included in estimating seismic risk. The substantial contribution of aftershocks to the collapse risk in the pre-mainshock environment highlights the need for a design procedure that accounts for the additional seismic risk from aftershocks.

6.2.3 Chapter 4: building service life economic loss assessment under sequential seismic events

Based on the seismic risk assessment framework proposed in Chapter 3, the main objective of Chapter 4 was to formulate a comprehensive framework for quantifying financial losses under sequential seismic events. Similar to the risk assessment approach, the framework proposed in this chapter is capable of accounting for the uncertainties in the state of structure due to accumulation of earthquake-induced damage, the time-dependent nature of seismic hazard in the post-mainshock environment and the uncertainties in the occurrence of mainshock and aftershock events. The framework can be utilized in estimating aftershock-only losses in the post-mainshock environment or mainshock-aftershock losses in the pre-mainshock environment and due to the all the seismic events that a building is likely to experience during its lifetime.

To demonstrate the potential application of the proposed framework, it was utilized in estimating seismic risk for a 4-story RC special moment frame building. The outputs of the

loss analysis in the post-mainshock environment suggested that, depending on the extent of the damage that the structure has experienced under mainshock, the aftershock-induced losses could be as high as 7% of the building's replacement cost. Imitation of repair measures that restore the structural capacity of the building was shown to be ineffective within the first few days after mainshock due to the high rate of aftershocks. It was shown that the contribution of losses due to the disruption in the normal functionality of the building could range from 9% to 55% of the total losses and increases with the extent of damage under the mainshock and the time elapsed since the occurrence of the mainshock. The greater seismic risk that the building experiences under aftershock ground motions led to the more significant presence of the collapse state in the aftershock-only losses compared to when losses are evaluated only under mainshock seismic events. A long-term evaluation of seismic losses for a lifespan of 50 years showed that consideration of aftershocks could increase lifecycle earthquake-induced losses by up to 30% compared to mainshock-only assessments.

6.2.4 Chapter 5: regional Short-Term and Long-Term Risk and Loss Assessment under Sequential Seismic Events

In this chapter, the risk and loss evaluation frameworks discussed in Chapters 4 and 5 were applied to the inventory of RC frame buildings in the Los Angeles County. The objective was to quantify the additional seismic risk and loss that aftershocks can impose on a high-seismicity region and the importance of accounting for aftershocks in pre-planning for major seismic events. The buildings in the database of the RC structures in Los Angeles County were divided into three design groups; ductile RC moment frame buildings that comply to the modern seismic design provisions that prevent non-desirable modes of failure such shear and axial failure in columns, nonductile RC moment frame building whose design dates back to the 1967 UBC and lack adequate reinforcement detailing to prevent brittle modes of failure, and RC frame buildings with unreinforced masonry infills that not only are prone to the undesirable behavior of the nonductile RC moment frames when subjected to earthquake ground motions but also suffer from the excessive demand imposed on their columns due to the presence of masonry infills.

The database of the buildings in Los Angeles County as well as the distinct damage states that each building can be when subjected to a seismic event were adopted from HAZUS. For the inventory of reinforced concrete frames located in Los Angeles County, the annual rate of "complete" (HAZUS) damage and expected annual losses are, on average, 10% and 25% higher, respectively, when aftershocks are incorporated in the risk assessment procedure. A

short-term risk assessment was performed for a duration of one week starting immediately after a scenario magnitude 7.0 on the Puente Hills fault. The significant temporary increase in the seismic activity as well as the reduction in the structural capacity of mainshock-damaged buildings increased the risk of Complete damage, on average, by a factor of 280. The aftershock-induced losses during the same period were estimated at approximately 30% of the losses due to the mainshock. Moreover, it was shown that incorporating aftershocks could increase the expected annual seismic losses by 25%.

6.3 Limitations and future work

The main focus of the current study is to formulate a comprehensive framework for seismic performance assessment under sequential ground motions and show its viability through application to a set of candidate RC frame buildings. It is important to note that the findings of the present study in terms of the potential seismic risk and loss that a building can experience when subjected to sequences of seismic events are limited to the set of buildings, ground motions and the hypothetical site described in the body of the manuscript. More studies with a variety of buildings, ground motions and sites with different characteristics are needed to more broadly quantify the impact of aftershocks on seismic performance.

We also should emphasize that the main purpose of this study was to demonstrate the viability of the discussed approach for small and large-scale seismic risk and loss assessments. The importance of the incorporation of aftershocks in the seismic performance evaluation steps has just recently become evident. As such, the data available on the performance of actual buildings under mainshock-aftershock ground motions is scarce compared to data available on the seismic response under single ground motions. While the findings of this study are based on robust probabilistic tools, they are necessary to be validated against data gathered on the seismic performance of actual buildings when subjected to sequences of mainshock-aftershock events.

The intensity measure primarily used in this study to link the building seismic response and site seismic hazard in the spectral acceleration at the first mode periods of the studied buildings. However, due to changes in strength and stiffness as well as the contribution of higher modes to the dynamic response, a structure that undergoes significant mainshock damage is expected to have a fundamental period that is different than that corresponding to its intact first mode. Alternative intensity measures, such as nonlinear spectral displacement, average spectral acceleration and vector-valued intensity measures have been shown to be more effective in representing the seismic response of nonlinear and complex structures

under mainshock ground motions. Similar findings are also expected to apply to seismic performance evaluation under sequential ground motions. As such, intensity measures other than the first-mode spectral acceleration may prove to be a more effective (efficient and sufficient) for assessing the seismic performance of mainshock-damaged buildings and should be investigated in future studies.

The aftershock seismic hazard calculations performed in this study use source models that are simpler than, for instance, the UCERF3-ETAS model. While the proposed frameworks are independent of the seismic hazard calculations approach, the accuracy of their outputs could be greatly improved by utilizing more robust source models.

Finally, as discussed before in Chapters 3 and 4, the risk and loss assessment frameworks proposed in this study assume that buildings are always restored to their initial state after they undergo a major mainshock and its subsequent aftershocks and before the next mainshock happens. However, buildings might experience minor levels of damage that, while affecting their structural capacity, would go unnoticed or deemed too insignificant for any repair measure to take place. These uncertainties in the state of buildings, while usually difficult to quantify, can be considered by modifying the building fragility curves. While in this study it is assumed that the impact of such uncertainties on building seismic performance is negligible, it is possible to consider such uncertainties by taking the same approach as the one discussed here for incorporating uncertainties in building limit state under sequential aftershocks.

References

[1] Parker M, Steenkamp D. The economic impact of the Canterbury earthquakes. Reserve Bank of New Zealand Bulletin. 2012;75.

[2] Dong W. Chi-Chi, Taiwan Earthquake Event Report. Risk Management Solutions, Inc, https://www rms com/Publications/Taiwan_Event pdf, retrieved Mar. 2010.

[3] Kazama M, Noda T. Damage statistics (Summary of the 2011 off the Pacific Coast of Tohoku Earthquake damage). Soils and Foundations. 2012;52:780-92.

[4] Burton HV, Deierlein G, Lallemant D, Lin T. Framework for incorporating probabilistic building performance in the assessment of community seismic resilience. Journal of Structural Engineering. 2015:C4015007.

[5] GEER Association. Engineering reconnaissance following the October 2016 central Italy earthquakes: Ver 2. Geotechnical Extreme Events Reconnaissance Association; 2017.

[6] Atzori S, Tolomei C, Antonioli A, Merryman Boncori J, Bannister S, Trasatti E, et al. The 2010–2011 Canterbury, New Zealand, seismic sequence: multiple source analysis from InSAR data and modeling. Journal of Geophysical Research: Solid Earth. 2012;117.

[7] Federal Emergency Management Agency (FEMA). FEMA P-58: Seismic performance assessment of buildings. Redwood City, CA2012.

[8] Wooddell KE, Abrahamson NA. Classification of main shocks and aftershocks in the NGA-West2 database. Earthquake Spectra. 2014;30:1257-67.

[9] Iervolino I, Giorgio M, Polidoro B. Sequence-based probabilistic seismic hazard analysis. Bulletin of the Seismological Society of America. 2014;104:1006-12.

[10] Boyd OS. Including foreshocks and aftershocks in time-independent probabilistic seismic-hazard analyses. Bulletin of the Seismological Society of America. 2012;102:909-17.

[11] Yeo GL, Cornell CA. A probabilistic framework for quantification of aftershock ground-motion hazard in California: Methodology and parametric study. Earthquake Engineering & Structural Dynamics. 2009;38:45-60.

[12] Hatzigeorgiou GD, Beskos DE. Inelastic displacement ratios for SDOF structures subjected to repeated earthquakes. Engineering Structures. 2009;31:2744-55.

[13] Nazari N, van de Lindt J, Li Y. Effect of mainshock-aftershock sequences on woodframe building damage fragilities. Journal of Performance of Constructed Facilities. 2013;29:04014036.

[14] Raghunandan M, Liel AB, Luco N. Aftershock collapse vulnerability assessment of reinforced concrete frame structures. Earthquake Engineering & Structural Dynamics. 2015;44:419-39.

[15] Ryu H, Luco N, Uma S, Liel A. Developing fragilities for mainshock-damaged structures through incremental dynamic analysis. Ninth Pacific Conference on Earthquake Engineering, Auckland, New Zealand2011.

[16] Jeon JS, DesRoches R, Lowes LN, Brilakis I. Framework of aftershock fragility assessment–case studies: older California reinforced concrete building frames. Earthquake Engineering & Structural Dynamics. 2015;44:2617-36.

[17] Burton HV, Sharma M. Quantifying the Reduction in Collapse Safety of Mainshock-Damaged Reinforced Concrete Frames with Infills. Earthquake Spectra. 2016.

[18] Amadio C, Fragiacomo M, Rajgelj S. The effects of repeated earthquake ground motions on the non-linear response of SDOF systems. Earthquake engineering & structural dynamics. 2003;32:291-308.

[19] Zhai C-H, Wen W-P, Chen Z, Li S, Xie L-L. Damage spectra for the mainshock–aftershock sequence-type ground motions. Soil Dynamics and Earthquake Engineering. 2013;45:1-12.

[20] Zhai C-H, Wen W-P, Li S, Xie L-L. The ductility-based strength reduction factor for the mainshock–aftershock sequence-type ground motions. Bulletin of Earthquake Engineering. 2015;13:2893-914.

[21] Goda K. Nonlinear response potential of mainshock–aftershock sequences from Japanese earthquakes. Bulletin of the Seismological Society of America. 2012;102:2139-56.

[22] Ruiz-García J. Mainshock-aftershock ground motion features and their influence in building's seismic response. Journal of Earthquake Engineering. 2012;16:719-37.

[23] Ruiz-García J, Negrete-Manriquez JC. Evaluation of drift demands in existing steel frames under as-recorded far-field and near-fault mainshock–aftershock seismic sequences. Engineering Structures. 2011;33:621-34.

[24] Zhai C-H, Wen W-P, Li S, Chen Z, Chang Z, Xie L-L. The damage investigation of inelastic SDOF structure under the mainshock–aftershock sequence-type ground motions. Soil Dynamics and Earthquake Engineering. 2014;59:30-41.

[25] Wen W, Zhai C, Ji D, Li S, Xie L. Framework for the vulnerability assessment of structure under mainshock-aftershock sequences. Soil Dynamics and Earthquake Engineering. 2017;101:41-52.

[26] Shcherbakov R, Turcotte DL. A modified form of Båth's law. B Seismol Soc Am. 2004;94:1968-75.

[27] Boore DM, Stewart JP, Seyhan E, Atkinson GM. NGA-West2 equations for predicting PGA, PGV, and 5% damped PSA for shallow crustal earthquakes. Earthq Spectra. 2014;30:1057-85.

[28] Utsu T, Ogata Y. The centenary of the Omori formula for a decay law of aftershock activity. Journal of Physics of the Earth. 1995;43:1-33.

[29] Goda K. Record selection for aftershock incremental dynamic analysis. Earthquake Engineering & Structural Dynamics. 2015;44:1157-62.

[30] Baker JW, Cornell CA. Vector-valued ground motion intensity measures for probabilistic seismic demand analysis: Pacific Earthquake Engineering Research Center, College of Engineering, University of California, Berkeley; 2006.

[31] Bradley BA, Dhakal RP, MacRae GA, Cubrinovski M. Prediction of spatially distributed seismic demands in specific structures: Ground motion and structural response. Earthquake Engineering & Structural Dynamics. 2010;39:501-20.

[32] Luco N, Cornell CA. Structure-specific scalar intensity measures for near-source and ordinary earthquake ground motions. Earthquake Spectra. 2007;23:357-92.

[33] Boore DM, Atkinson GM. Spectral scaling of the 1985 to 1988 Nahanni, Northwest Territories, earthquakes. Bulletin of the Seismological Society of America. 1989;79:1736-61.

[34] Ancheta TD, Darragh RB, Stewart JP, Seyhan E, Silva WJ, Chiou BS-J, et al. NGA-West2 database. Earthquake Spectra. 2014;30:989-1005.

[35] Power M, Chiou B, Abrahamson N, Bozorgnia Y, Shantz T, Roblee C. An overview of the NGA project. Earthquake spectra. 2008;24:3-21.

[36] Abrahamson N, Silva W, Kamai R. Update of the AS08 Ground-Motion Prediction equations based on the NGA-west2 data set. Pacific Earthquake Engineering Research Center, College of Engineering, University of California, Berkeley; 2013.

[37] Chiou B-J, Youngs RR. An NGA model for the average horizontal component of peak ground motion and response spectra. Earthquake Spectra. 2008;24:173-215.

[38] Kagan YY. Aftershock zone scaling. Bulletin of the Seismological Society of America. 2002;92:641-55.

[39] Massey Jr FJ. The Kolmogorov-Smirnov test for goodness of fit. Journal of the American statistical Association. 1951;46:68-78.

[40] Ruiz-García J, Miranda E. Inelastic displacement ratios for evaluation of existing structures. Earthquake Engineering & Structural Dynamics. 2003;32:1237-58.

[41] Miranda E. Inelastic displacement ratios for structures on firm sites. Journal of Structural Engineering. 2000;126:1150-9.

[42] Veletsos A, Newmark N, Chelapati C. Deformation spectra for elastic and elastoplastic systems subjected to ground shock and earthquake motions. Proceedings of the 3rd world conference on earthquake engineering1965. p. 663-82.

[43] Chopra AK, Chintanapakdee C. Inelastic deformation ratios for design and evaluation of structures: single-degree-of-freedom bilinear systems. Journal of structural engineering. 2004;130:1309-19.

[44] Tothong P, Cornell CA. An empirical ground-motion attenuation relation for inelastic spectral displacement. Bulletin of the Seismological Society of America. 2006;96:2146-64.

[45] Chopra AK. Dynamics of structures: Prentice Hall New Jersey; 1995.

[46] Haselton CB. Assessing Seismic Collapse Safety of Modern Reinforced Concrete Moment Frame Buildings. PhD Dissertation: Department of Civil and Environmental Engineering, Stanford University; 2007.

[47] American Society of Civil Engineers (ASCE). ASCE/SEI 7-05: Minimum design loads for buildings and other structures. Reston, VA2005.

[48] American Concrete Institue (ACI). ACI 318M-02: Building code requirements for structural concrete and commentary. Farmington Hills, MI2002.

[49] Mazzoni S, McKenna F, Scott MH, Fenves GL. OpenSees command language manual. Pacific Earthquake Engineering Research Center, University of California, Berkeley; 2006.

[50] Ibarra LF, Medina RA, Krawinkler H. Hysteretic models that incorporate strength and stiffness deterioration. Earthquake engineering & structural dynamics. 2005;34:1489-511.

[51] Haselton CB, Liel AB, Deierlein GG, Dean BS, Chou JH. Seismic collapse safety of reinforced concrete buildings. I: Assessment of ductile moment frames. Journal of Structural Engineering. 2010;137:481-91.

[52] United States Geological Survey (USGS). Unified Hazard Tool. 2017.

[53] Field EH, Jordan TH, Cornell CA. OpenSHA: A developing community-modeling environment for seismic hazard analysis. Seismological Research Letters. 2003;74:406-19.

[54] Field EH, Arrowsmith RJ, Biasi GP, Bird P, Dawson TE, Felzer KR, et al. Uniform California earthquake rupture forecast, version 3 (UCERF3)—The time-independent model. Bulletin of the Seismological Society of America. 2014;104:1122-80.

[55] Reasenberg PA, Jones LM. Earthquake hazard after a mainshock in California. Science. 1989;243:1173-6.

[56] Boore DM, Atkinson GM. Ground-motion prediction equations for the average horizontal component of PGA, PGV, and 5%-damped PSA at spectral periods between 0.01 s and 10.0 s. Earthquake Spectra. 2008;24:99-138.

[57] Joyner WB, Boore DM. Methods for regression analysis of strong-motion data. B Seismol Soc Am. 1993;83:469-87.

[58] Joyner WB, Boore DM. Methods for regression analysis of strong-motion data. Bulletin of the Seismological Society of America. 1994;84:955-6.

[59] Yeo GL, Cornell CA. Stochastic characterization and decision bases under time-dependent aftershock risk in performance-based earthquake engineering: Pacific Earthquake Engineering Research Center; 2005.

[60] Howard RA. Dynamic probabilistic systems. Vol. 2. Semi-Markov and decision processes. 1971.

[61] Baker JW. Efficient analytical fragility function fitting using dynamic structural analysis. Earthquake Spectra. 2015;31:579-99.

[62] Haselton C, Mitrani-Reiser J, Goulet C, Deierlein G, Beck J, Porter K, et al. An Assessment to Benchmark the Seismic Performance of a Code-Conforming Reinforced concrete Moment-Frame Building, PEER 2007/12. Berkeley, CA: Pacific Earthquake Engineering Research Center, University of California, Berkeley; 2007.

[63] Yeo GL, Cornell CA. Stochastic characterization and decision bases under time-dependent aftershock risk in performance-based earthquake engineering. Pacific Earthquake Engineering Research Center, College of Engineering, University of California, Berkeley; 2005.

[64] Holzer TL. Implications for earthquake risk reduction in the United States from the Kocaeli, Turkey, earthquake of August 17, 1999: US Geological Survey, Information Services; 2000.

[65] Comerio M, Elwood K, Berkowitz R. The M 6.3 Christchurch, New Zealand, Earthquake of February 22, 2011. EERI special earthquake report. Earthquake Engineering Research Institute (EERI), Oakland. 2011.

[66] Parker M, Steenkamp D. The economic impact of the Canterbury earthquakes. Reserve Bank of New Zealand Bulletin. 2012;75:13-25.

[67] Abrahamson N, Atkinson G, Boore D, Bozorgnia Y, Campbell K, Chiou B, et al. Comparisons of the NGA ground-motion relations. Earthquake Spectra. 2008;24:45-66.

[68] Li Q, Ellingwood BR. Performance evaluation and damage assessment of steel frame buildings under main shock–aftershock earthquake sequences. Earthquake engineering & structural dynamics. 2007;36:405-27.

[69] Ruiz-García J, Aguilar JD. Aftershock seismic assessment taking into account postmainshock residual drifts. Earthquake Engineering & Structural Dynamics. 2015;44:1391-407.

[70] Hatzigeorgiou GD, Liolios AA. Nonlinear behaviour of RC frames under repeated strong ground motions. Soil Dynamics and Earthquake Engineering. 2010;30:1010-25.

[71] Luco N, Bazzurro P, Cornell CA. Dynamic versus static computation of the residual capacity of a mainshock-damaged building to withstand an aftershock. Proceedings of the 13th world conference on earthquake engineering: Vancouver, Canada; 2004.

[72] Bazzurro P, Cornell C, Menun C, Motahari M. Guidelines for seismic assessment of damaged buildings. Proceedings of the 13th World Conference on Earthquake Engineering, Vancouver, Canada2004.

[73] Maffei J, Telleen K, Nakayama Y. Probability-based seismic assessment of buildings, considering post-earthquake safety. Earthquake Spectra. 2008;24:667-99.

[74] Han R, Li Y, van de Lindt J. Assessment of seismic performance of buildings with incorporation of aftershocks. Journal of Performance of Constructed Facilities. 2014;29:04014088.

[75] Tesfamariam S, Goda K, Mondal G. Seismic Vulnerability of Reinforced Concrete Frame with Unreinforced Masonry Infill Due to Main Shock-Aftershock Earthquake Sequences. Earthquake Spectra. 2015;31:1427-49.

[76] Yeo GL, Cornell CA. Building life-cycle cost analysis due to mainshock and aftershock occurrences. Structural Safety. 2009;31:396-408.

[77] Ebrahimian H, Jalayer F, Asprone D, Lombardi AM, Marzocchi W, Prota A, et al. A performance-based framework for adaptive seismic aftershock risk assessment. Earthquake Engineering & Structural Dynamics. 2014;43:2179-97.

[78] Iervolino I, Giorgio M, Chioccarelli E. Markovian modeling of seismic damage accumulation. Earthquake Engineering & Structural Dynamics. 2015.

[79] Nazari N, van de Lindt J, Li Y. Quantifying Changes in Structural Design Needed to Account for Aftershock Hazard. Journal of Structural Engineering. 2015;141:04015035.

[80] Tothong P, Luco N. Probabilistic seismic demand analysis using advanced ground motion intensity measures. Earthquake Engineering & Structural Dynamics. 2007;36:1837-60.

[81] Eads L, Miranda E, Lignos DG. Average spectral acceleration as an intensity measure for collapse risk assessment. Earthquake Engineering & Structural Dynamics. 2015.

[82] Kramer SL. Geotechnical earthquake engineering: Pearson Education India; 1996.

[83] Shcherbakov R, Turcotte DL, Rundle JB. Aftershock statistics. Pure and Applied Geophysics. 2005;162:1051-76.

[84] Knopoff L, Gardner J. Higher seismic activity during local night on the raw worldwide earthquake catalogue. Geophysical Journal of the Royal Astronomical Society. 1972;28:311-3.

[85] Haselton C, Liel A, Deierlein G, Dean B, Chou J. Seismic Collapse Safety of Reinforced Concrete Buildings. I: Assessment of Ductile Moment Frames. Journal of Structural Engineering. 2011;137:481-91.

[86] Wen Y-K, Kang Y. Minimum building life-cycle cost design criteria. I: Methodology. J Struct Eng. 2001;127:330-7.

[87] Goulet CA, Haselton CB, Mitrani-Reiser J, Beck JL, Deierlein GG, Porter KA, et al. Evaluation of the seismic performance of a code-conforming reinforced-concrete frame building—from seismic hazard to collapse safety and economic losses. Earthquake Engineering & Structural Dynamics. 2007;36:1973-97.

[88] Ramirez C, Liel A, Mitrani-Reiser J, Haselton C, Spear A, Steiner J, et al. Expected earthquake damage and repair costs in reinforced concrete frame buildings. Earthq Eng Struct D. 2012;41:1455-75.

[89] Takahashi Y, Kiureghian AD, Ang AHS. Life-cycle cost analysis based on a renewal model of earthquake occurrences. Earthq Eng Struct D. 2004;33:859-80.

[90] Tao Z, Corotis RB, Ellis JH. Reliability-based structural design with Markov decision processes. Journal of Structural Engineering. 1995;121:971-80.

[91] Moehle J, Deierlein GG. A framework methodology for performance-based earthquake engineering. 13th world conference on earthquake engineering2004. p. 3812-4.

[92] Porter KA. Safe enough? A building code to protect our cities as well as our lives. Earthquake Spectra. 2015.

[93] Jalayer F, Asprone D, Prota A, Manfredi G. Multi-hazard upgrade decision making for critical infrastructure based on life-cycle cost criteria. Earthq Eng Struct D. 2011;40:1163-79.

[94] Alessandri S, Giannini R, Paolacci F. Aftershock risk assessment and the decision to open traffic on bridges. Earthq Eng Struct D. 2013;42:2255-75.

[95] Fereshtehnejad E, Shafieezadeh A. Multiple hazard incidents lifecycle cost assessment of structural systems considering state-dependent repair times and fragility curves. Earthq Eng Struct D. 2016;45:2327-47.

[96] Shokrabadi M, Burton HV, Stewart JP. Impact of Sequential Ground Motion Pairing on Mainshock-Aftershock Structural Response and Collapse Performance Assessment. Journal of Structural Engineering (accepted for publication). 2017.

[97] Ross SM. Introduction to probability models: Academic press; 2014.

[98] ACI (American Concrete Institue). ACI 318M-02: Building code requirements for structural concrete and commentary. Farmington Hills, MI2002.

[99] ASCE (American Society of Civil Engineers). ASCE/SEI 7-05: Minimum design loads for buildings and other structures. Reston, VA2005.

[100] Haselton Baker Risk Group. Seismic Performance Prediction Program, (SP3). 2017.

[101] FEMA (Federal Emergency Management Agency). FEMA P-58: Seismic performance assessment of buildings. Redwood City, CA2012.

[102] Chiou B, Darragh R, Gregor N, Silva W. NGA project strong-motion database. Earthquake Spectra. 2008;24:23-44.

[103] Federal Emergency Management Agency (FEMA). Hazus - MH 2.1 Technical Manual. Washington, D.C.

[104] Goda K, Kiyota T, Pokhrel RM, Chiaro G, Katagiri T, Sharma K, et al. The 2015 Gorkha Nepal earthquake: insights from earthquake damage survey. Frontiers in Built Environment. 2015;1:8.

[105] Krawinkler H, Miranda E. Performance-based earthquake engineering. CRC Press: Boca Raton, FL; 2004. p. 1-9.

[106] Federal Emergency Management Agency (FEMA) Hazus 4.0. Washington, D.C2017.

[107] Pagani M, Monelli D, Weatherill G, Danciu L, Crowley H, Silva V, et al. OpenQuake engine: an open hazard (and risk) software for the global earthquake model. Seismological Research Letters. 2014;85:692-702.

[108] Tantala MW, Nordenson GJ, Deodatis G, Jacob K. Earthquake loss estimation for the New York City metropolitan region. Soil Dynamics and Earthquake Engineering. 2008;28:812-35.

[109] Jaiswal KS, Bausch D, Chen R, Bouabid J, Seligson H. Estimating annualized earthquake losses for the conterminous United States. Earthquake Spectra. 2015;31:S221-S43.

[110] Chen R, Branum DM, Wills CJ. Annualized and scenario earthquake loss estimations for California. Earthquake Spectra. 2013;29:1183-207.

[111] Chen R, Jaiswal K, Bausch D, Seligson H, Wills C. Annualized earthquake loss estimates for California and their sensitivity to site amplification. Seismological Research Letters. 2016;87:1363-72.

[112] Field EH, Jordan TH, Jones LM, Michael AJ, Blanpied ML, Participants W. The potential uses of operational earthquake forecasting. Seismological Research Letters. 2016;87:313-22.

[113] Jordan T, Chen Y-T, Gasparini P, Madariaga R, Main I, Marzocchi W, et al. Operational Earthquake Forecasting: State of Knowledge and Guidelines for Implementation. Annals of Geophysics. 2011.

[114] Iervolino I, Chioccarelli E, Giorgio M, Marzocchi W, Zuccaro G, Dolce M, et al. Operational (short-term) earthquake loss forecasting in Italy. Bulletin of the Seismological Society of America. 2015.

[115] Field E, Porter K, Milner K. A Prototype Operational Earthquake Loss Model for California Based on UCERF3-ETAS–A First Look at Valuation. Earthquake Spectra. 2017;33:1279-99.

[116] Field EH, Milner KR, Hardebeck JL, Page MT, van der Elst N, Jordan TH, et al. A Spatiotemporal Clustering Model for the Third Uniform California Earthquake Rupture Forecast (UCERF3-ETAS): Toward an Operational Earthquake Forecast. Bulletin of the Seismological Society of America. 2017;107:1049-81.

[117] United States Census Bureau.

[118] Jayaram N, Baker JW. Efficient sampling and data reduction techniques for probabilistic seismic lifeline risk assessment. Earthquake Engineering & Structural Dynamics. 2010;39:1109-31.

[119] Jayaram N, Baker JW. Correlation model for spatially distributed ground-motion intensities. Earthquake Engineering & Structural Dynamics. 2009;38:1687-708.

[120] Council LATBSD. An alternative procedure for seismic analysis and design of tall buildings located in the Los Angeles region. 2013.

[121] Shokrabadi M, Burton HV. Risk-based assessment of aftershock and mainshock-aftershock seismic performance of reinforced concrete frames. Structural Safety. 2018;73:64-74.

[122] Shokrabadi M, Burton HV. Building service life economic loss assessment under sequential seismic events. Earthquake Engineering & Structural Dynamics.

[123] Kircher CA, Whitman RV, Holmes WT. HAZUS earthquake loss estimation methods. Natural Hazards Review. 2006;7:45-59.

[124] Anagnos T, Comerio MC, Stewart JP. Earthquake loss estimates and policy implications for nonductile concrete buildings in Los Angeles. Earthquake Spectra. 2016;32:1951-73.

[125] Liel AB, Haselton CB, Deierlein GG. Seismic collapse safety of reinforced concrete buildings. II: Comparative assessment of nonductile and ductile moment frames. Journal of Structural Engineering. 2010;137:492-502.

[126] Burton H, Deierlein G. Simulation of seismic collapse in nonductile reinforced concrete frame buildings with masonry infills. Journal of Structural Engineering. 2013;140:A4014016.

[127] Raghunandan M, Liel AB, Luco N. Collapse risk of buildings in the Pacific northwest region due to subduction earthquakes. Earthquake Spectra. 2015;31:2087-115.